DYNAMIC SIMULATION AND CONTROL OF A HYBRID GASIFIER/REFORMER SYSTEM

DYNAMIC SIMULATION AND CONTROL OF A HYBRID COAL GASIFIER /
STEAM METHANE REFORMER SYSTEM

By DOMINIK SEEPERSAD, B.E.Sc.

A Thesis Submitted to the School of Graduate Studies
in Partial Fulfillment of the Requirements
for the Degree
Master of Applied Science

McMaster University

MASTER OF APPLIED SCIENCE (2014)   McMaster University

(Chemical Engineering)   Hamilton, Ontario, Canada

TITLE: Dynamic Simulation and Control of a Hybrid Coal Gasifier
                    / Steam Methane Reformer System

AUTHOR: Dominik Seepersad, B.E.Sc. (Chemical Engineering)
                    (The University of Western Ontario, Canada)

SUPERVISOR: Dr. Thomas A. Adams II

NUMBER OF PAGES: xvii, 145

ABSTRACT

Polygeneration plants are proposed as an attractive solution to today's challenging economic and political climate, whereby fossil fuels (e.g.: coal, natural gas) can be co-processed to obtain multiple products, such as electricity, gasoline and diesel. To this end, this thesis investigates the feasibility of the operation and control of a novel cooling system which incorporates steam methane reformer (SMR) tubes into a gasifier radiant syngas cooler (RSC). This approach capitalizes on available exergy by producing valuable H_2-rich synthesis gas (syngas) for liquid fuel production. As the device is still in the conceptual phase, a detailed multi-scale, two-dimensional, heterogeneous model has been developed in prior work to accurately predict the unit's operation.

A base case design was developed for both counter-current and co-current flow configurations, wherein a PI control structure designed to achieve performance objectives. Key trade-offs were found between the configurations: the counter-current design was more robust and effective in rejecting moderate and severe disturbances, while providing greater cooling duty and natural gas throughput, but at the expense of dangerously high tube wall temperatures, which can greatly reduce tube lifetime. The co-current design operates in a safer temperature range and satisfactorily rejects moderate disturbances, but requires feedforward control to handle extreme gasifier upsets.

An offset-free linear model predictive controller (MPC) was developed for the co-current system to address process interactions. The MPC model was identified from 'data' derived from the rigorous plant model, with a Luenberger observer used to estimate and eliminate the plant-model mismatch. MPC offered superior set point tracking relative to discrete-PI control, especially in cases where discrete-PI destabilized the system. Using the co-current design, the flexibility of the device to adjust natural gas throughput based on variations in downstream syngas demand was demonstrated.

ACKNOWLEDGEMENTS

I wish to thank the many people that have been instrumental in my completion of this thesis. Firstly, I wish to express my sincerest gratitude to my supervisor, Dr. Thomas Adams II, for this opportunity, and for his continual and insightful advice, patience and support throughout my research here at McMaster. I am truly honoured to have had him as my supervisor, and thank him for giving me the push to achieve so much more than I thought possible. I also wish to thank Dr. Christopher Swartz and Dr. Prashant Mhaskar for their guidance on my thesis committee.

The suggestions and input from Matt have greatly aided me in the last stages of my research, which I genuinely appreciate. Special thanks goes to Jake and Chinedu for their assistance in improving the quality and presentation of this manuscript, I could not have gotten this far without their generous and unwavering help. My time at the MACC was truly a rewarding, stimulating and entertaining experience, many thanks to the penthouse craw whom I've had the greatest pleasure in getting to know: Jake, Alicia, Jaffer, Chris, Chinedu, Vida, Yasser, Kyle, Kushlani and Mudassir.

In being so far away from my homeland, I have been truly blessed and fortunate to have been a part of MACSA, my family away from home. I have made some of the very best friends of my life here: Sean, Arielle, Phoebe, Louidgie and many others; thank you for your amazing friendship throughout this entire experience, and for reminding me of the truly important things in life.

To my family in Trinidad: my parents Joe and Jill, my sister Denisa and my cousin Elizabeth (mining village); your never-ending love and support have sustained me throughout this endeavour, and I thank you. And to my beloved, Kelby, you have always encouraged the very best in me, and this journey has been infinitely more fun, exhilarating and rewarding with you by my side. Last but not least, I thank God for His steadfast grace and mercy, without which I would not be here today.

This work is dedicated to Joe, Jill, Denisa and Kelby.

Table of Contents

LIST OF FIGURES

LIST OF TABLES

LIST OF ABBREVIATIONS AND SYMBOLS

Abbreviations

ACM	Aspen Custom Modeler
ARX	Auto-Regressive with Exogenous Input
ASU	Air Separation Unit
ATR	Autothermal Reformer
C-C	Cohen-Coon
CCS	Carbon Capture and Sequestration
CFD	Computational Fluid Dynamics
COT	Coil Outlet Temperature
CSTR	Continuously-Stirred Tank Reactor
CTL	Coal-to-Liquids
CV	Controlled Variable
DMC	Dynamic Matrix Control
DV	Disturbance Variable
EPRI	Electric Power Research Institute
FT	Fischer-Tropsch
GE	General Electric
GTL	Gas-to-Liquids
HER	Heat Exchange Reformer
HHV	Higher Heating Value
HTFT	High Temperature Fischer Tropsch
IAE	Integral Absolute Error
ID	Inner Diameter
IGCC	Integrated Gasification Combined Cycle
IMC	Internal Model Control
ISE	Integral Squared Error
ITAE	Integral Time Absolute Error
LTFT	Low Temperature Fischer Tropsch
MIMO	Multiple-Input-Multiple-Output
MPC	Model Predictive Control
MV	Manipulated Variable
NETL	National Energy Technology Laboratory
NG	Natural Gas
ODE	Ordinary Differential Equation
PC	Pulverized Coal
PDE	Partial Differential Equation
PFR	Plug Flow Reactor
PI	Proportional-Integral
PID	Proportional-Integral-Derivative

POX	Partial Oxidation Section
RGA	Relative Gain Array
RSC	Radiant Syngas Cooler
S/C	Steam-to-Carbon ratio
SISO	Single-Input-Single-Output
SMR	Steam Methane Reformer
syngas	Synthesis Gas
TWT	Tube Wall Temperature
WGS	Water-Gas Shift
Z-N	Ziegler-Nichols
ZOH	Zero-Order-Hold

Subscripts

C	Catalyst
i	Discrete sample index or Gas species index
L	Linear
NL	Non-linear
R	Refractory wall
S	Shell gas
T	Tube gas
W	Tube wall

Superscripts

| in | Inlet |
| out | Outlet |

Symbols

A_{CS}	Cross-sectional area
C	Concentration
C_p	Heat capacity
D_{RSC}	RSC inner diameter
dir	Flow direction
E	Error
E_a	Activation energy
F	Molar flow rate
F_{SMR}	Total molar feed flow to SMR tube
G	Transfer function
h	Heat transfer coefficient
H	Enthalpy
k	Sampling instant

k	Pre-exponential factor
K_C	Controller gain
K_{eq}	Equilibrium constant
k_i	Mass transfer coefficient
L	RSC length
$\mathbf{L}$	Luenberger gain matrix
M_S	Shell gas mass flow rate
N	Control horizon
N_t	Number of tubes
P	Prediction horizon
P	Pressure
Q	Heat transfer
r	Radial position
R	Radius
r_i	Reaction rate of species i
$R_{S/C}$	Steam-to-Carbon ratio
S	Discrete error summation
SP	Set point
T	Temperature
T_{gas}	SMR exit gas temperature
v	Gas velocity
y	mole fraction
y_{CH_4}	CH_4 Slip
z	Axial position

Greek Letters

α	Switching parameter
ΔP	Pressure drop
Δt	Sample time
ε	Bed porosity
ϵ	Gas emissivity
θ_d	Dead time
Θ	Fictitious disturbance state
λ	Thermal conductivity or Switching parameter
μ	Pareto optimal weighting parameter
ρ	Density
σ	Stefan-Boltzmann constant
τ_p	Process time constant
τ_i	Integral time constant

Chapter 1

Introduction

1.1 Motivation and Goals

In the developed world, technology, improved quality of life and an energy-based economy have placed an enormous demand on natural resources, particularly on fossil fuels which constitute the majority of the modern world's energy supply. In particular global electricity is expected to grow by 2.6% per year over the next twenty years (BP p.l.c., 2014) of which coal and natural gas provide 43% and 21% of the energy share respectively (Figure 1.1). Within North America, which possesses 28.5% of the world's coal reserves (BP p.l.c., 2013), almost all of the coal-based power plants in existence are based on aged Pulverized Coal technology, which suffer from low efficiencies and high CO_2 emission rates. Meanwhile the world's most populous countries, China and India, are expected to depend on coal for power production as their economies become more industrialized, contributing 87% of the growth of global coal consumption over the next twenty years (BP p.l.c., 2014). With this increased energy demand fueled by GDP growth, improvements in energy efficiency are necessary to decelerate the corresponding increase in resource depletion and pollutant emissions.
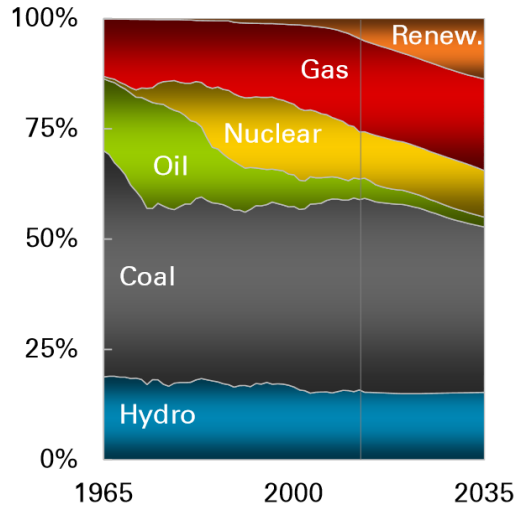
Figure 1.1: Fuel input mix for global power production (reprinted from (BP p.l.c., 2014)).

An interesting multifaceted technology which has emerged as a promising concept to replace existing power production facilities while addressing key environmental and social issues is the flexible polygeneration plant. Polygeneration utilizes various advanced technologies to produce multiple products such as electricity, gasoline and diesel from multiple (at times unconventional) feedstocks such as coal, natural gas and biomass. The polygeneration plant considered in this work is based on Adams and Barton (2011) which uses coal gasification to produce synthesis gas (syngas), which is correspondingly used to co-produce electricity and liquid fuels. While the composition of this coal-derived syngas is sufficient for power production, the hydrogen content must be increased for liquid fuel production. Adams and Barton (2011) explore multiple strategies to accomplish this, with the strategy of most interest involving methane reforming performed within the radiant syngas cooler (RSC) tubes of the gasifier. In current state-of-the-art gasifiers, high pressure steam (HPS) production is used to cool the very hot coal-syngas; by replacing this cooling mechanism with the endothermic methane reforming reactions, effective cooling duty is supplied whilst producing H_2-rich syngas, which is more valuable than steam and can upgrade the coal-derived syngas for downstream processes.

Polygeneration touts several advantages: increased efficiency, the ability to achieve zero process CO_2 emissions, and reduced sensitivity to volatility in feedstock availability and product pricing. While the integrated gasification/reforming approach was predicted to be most efficient and profitable over a range of expected market scenarios, previous studies have only looked at overly simple, zero-order models of the proposed integrated gasifier/reformer device in order to make performance estimates of the system as a whole. However, certain important and specific details of the device itself have not been explored, and prior to this work, it had not yet been shown that the proposed device was even feasible to operate. In particular, a feasible design that simultaneously considers the requirements and limitations of gasifier and methane reforming processes must be established. As there is considerable difficulty involved in gasifier operation, it would be ideal if the integrated gasifier/reformer does not pose any additional burden to the operators, and should require minimal tuning effort and maintenance, while simultaneously rejecting plausible disturbances satisfactorily. Additionally, the operation of the device within a flexible polygeneration framework has to be addressed, which places importance on effective control for transient operation from one operating mode to another.

To address these objectives, a rigorous dynamic, two-dimensional heterogeneous model has been developed (Ghouse et al., 2014), which accurately describes key temperature, pressure and concentration profiles within the different elements of the device. This model forms the foundation for the work carried out in this thesis, whose major objective is to investigate the operability and control of the proposed gasifier/reformer device.

1.2   Main Contributions

Model Improvements:

Certain modifications were made to the model of the device described in (Ghouse et al., 2014), to allow control studies to be explored. In particular, the coal-derived syngas phase model was enhanced to allow for simulation of disturbances, by implementing mass and

momentum balances, and accounting for the water-gas shift reaction. Tube and refractory wall models were improved to capture heat transfer effects more accurately, a critical component of such a highly thermally integrated system. Key adjustments to model structure and discretization were implemented to improve simulation speed and accuracy, in order to effectively perform control studies.

Investigation of co-current and counter-current implementation:

Relative to the coal-derived syngas flow, the device can be implemented within the radiant cooler in either a co-current or counter-current configuration. For both configurations, the design of the device that allows for feasible operation was still unknown, thus an initial goal was to determine which configuration would best suit the overall plant objectives. This work addressed this by developing a base case design that considers spatial restrictions within the existing syngas cooler, meets safety criteria, rejects gasifier disturbances, and transitions between operating modes smoothly. Each flow configuration involves unique challenges with respect to the various constraints and objectives which are identified in this work.

Development of control structures:

An appropriate control structure was identified for the device based on historical methane reformer control methods and knowledge of gasifier operation. Trade-offs in the degrees of freedom were identified with the hybrid system that do not exist with the independent technologies. A series of increasingly complex control strategies were developed for the device, from classical PI control, to feedforward/feedback, to offset-free model predictive control (MPC); each of these were tested using a sequence of set point changes and disturbance scenarios to determine its operability within an actual gasifier system, while satisfying key safety and performance objectives.

1.3   Thesis Overview

Chapter 2:

This chapter provides background and literature review of relevant topics to the development of the work. In particular, the technologies of gasifiers and steam methane reformers are discussed in the context of synthesis gas production. These two technologies are brought together within a polygeneration framework which is also discussed.

Chapter 3:

This chapter gives an overview of the mathematical model developed for this work. In particular, most of the details are provided in (Ghouse et al., 2014); this chapter is concerned with modifications to the model made by the author of this thesis to render it fit for control and operation studies.

Chapter 4:

This chapter uses the mathematical model described in chapter 3 to develop a PI control structure for the proposed device. Both co-current and counter-current configurations are developed and simulated, in order to assess the benefits and drawbacks of each. The selected control configuration is subjected to set point changes and realistic disturbances to assess the operability of the proposed system under industrial conditions.

Chapter 5:

This chapter expands on the control studies of chapter 4, by introducing the effects of implementing discrete control. The impact of sample time on the PI control performance is assessed, and an offset-free Model Predictive Control device is developed using system identification techniques and implemented. MPC is compared against PI using a series of set point change and disturbance scenarios.

Chapter 6:

Major conclusions are summarized from the results in this work, and recommendations are made with respect to future research directions.

Chapter 2

Background and Literature Review

The purpose of this chapter is to provide background information and a brief review of topics that are relevant to this research project. This work concerns the integration of two independent technologies: coal gasification and steam methane reforming, in a manner that has not been performed previously. As a result, apart from the model developed for this work (Ghouse et al., 2014), there is no existing literature on the modeling of the integrated system. In light of this, coal gasification and steam methane reforming will be reviewed as separate technologies within the next subsections. With a detailed understanding of the separate technologies, the method and implications of integration will be covered in a broader context within the polygeneration subsection.

2.1   Gasification

2.1.1   Process Overview

Synthesis gas (syngas) is produced via two mechanisms: reforming and gasification. Both mechanisms involve the conversion of carbonaceous fuels to syngas, but the primary distinction is that gasification refers to solid feedstocks and reforming refers to liquid or gaseous feedstocks (Steynberg and Dry, 2004). Gasification is the conversion of coal to syngas by partial combustion. The primary constituents of this coal-syngas in order of decreasing concentration are: carbon monoxide (CO), hydrogen (H_2), water (H_2O) and carbon dioxide (CO_2). There are three main types of commercial-scale gasifiers. The fixed bed gasifier produces syngas with an exit temperature of around 600°C; the Sasol-Lurgi design is most popular example of this strategy (Steynberg and Dry, 2004). Fluidized bed gasifiers typically have a higher syngas exit temperature of 1,000°C; the Kellogg Rust Westinghouse (KRW) design is most popular of the fluidized bed designs. Entrained bed gasifiers are the most commercially successful gasifier type in the world to date, and operate with a syngas exit temperature of over 1,200°C. The most popular design in this regard is the GE-Texaco gasifier, which is adopted in this work, and was adopted in several preceding studies (Adams and Barton, 2011; Ghouse et al., 2014). As it will be shown, the Texaco gasifier syngas product contains large amounts of sensible heat to be exploited, and is advantageous to the proposed hybrid system. Because of these high temperatures, the existing Texaco gasifiers at Cool Water (EPRI, 1990) and Polk Power Station (McDaniel and Hornick, 2002) utilize a radiant syngas cooler (RSC), to capture the high temperature heat.

The GE-Texaco design considered in this work consists of three main parts connected in series in the following order: the partial oxidation (POX) section, the RSC section and the quench section. The refractory-lined POX unit is first in the sequence, in which oxygen and a slurry of coal and water are fed through the top. The oxygen is supplied to the gasifier from an air separation unit (ASU). The gasification reactions take place in the POX at 55 bar and 1,316°C (Woods et al., 2007). The resulting syngas is comprised mainly of

CO, H_2, CO_2 and H_2O upon entering the RSC section. Heat from the coal-derived syngas is recovered by passing sub-cooled feed water through radiant tubes to produce high pressure steam (Monaghan and Ghoniem, 2012c). Coal ash flows downwards through the center of the RSC as molten slag, into the quench pool below. The cooled syngas, now at approximately 816°C, exits out of the bottom of the RSC, passes through the quench pool, and is sent to a gas cleanup train to remove sulphides and particulates. The clean syngas can then be upgraded using water-gas shift (WGS) reactors and used for electricity generation or liquid fuel production via Fischer-Tropsch (FT) synthesis.

Different types of coal and petroleum coke (petcoke) can be used as gasifier feedstock, which can lead to significant variations in gasifier temperature and syngas composition. Illinois #6 coal is the most commonly used feedstock among the conceptual design literature because researchers across the industry have unofficially agreed to use this coal type as a uniform basis on which many different systems can be compared. Thus, it will also be the type considered in this work.

2.1.2 Gasifier RSC Design and Modeling

The focus of this research is around designing a cooling system for the RSC, and as such, the following review concerns developments within this area. Overall, the gasification reactions and flow regimes are quite complex, and require rigorous modeling of the POX chamber, which is outside the scope of this work. Due to this complexity, most of the gasifier modeling efforts in the literature have been steady-state, ranging from one-dimensional models (Govind and Shah, 1984; Kasule et al., 2012; Qian et al., 2013) to three-dimensional computational fluid dynamics (CFD) models (Bockelie et al., 2003; Watanabe and Otaka, 2006). Even fewer published works are concerned with dynamic modeling (Monaghan and Ghoniem, 2012b; Robinson and Luyben, 2008), particularly regarding the RSC. The difficulty in RSC modeling is exacerbated by non-disclosure of key design parameters and operational data by industrial plant reports (EPRI, 1990;

McDaniel and Hornick, 2002; Woods et al., 2007), necessitating researchers to make numerous speculative assumptions regarding the RSC shell and radiant tube sizing.

Monaghan and Ghoniem (2012b) provided a comprehensive gasifier and RSC model for entrained flow gasifiers, and validated it against lab scale gasifier data (Monaghan and Ghoniem, 2012a). The model was then used to simulate steady-state and dynamic operation of the industrial scale GE-Texaco gasifier (Monaghan and Ghoniem, 2012c). The purpose of the model was to provide accurate results without the computational expense of CFD modeling; as such, the model, solved using Aspen Custom Modeler (ACM), was characterized by one-dimensional partial differential equations (PDEs), which capture the essential chemical and thermal phenomena. The RSC was modeled as a counter-current plug flow reactor (PFR), with the radiant tubes placed in a ring surrounding the center.

(Robinson and Luyben, 2008) developed a dynamic model of the Texaco gasifier and RSC within Aspen Dynamics. In this model, the RSC was modeled as a combination of continuously-stirred tank reactors (CSTRs) and a PFR, in an effort to reduce numerical instability. Due to this approximation, axial temperature and mole-fraction profiles for the RSC were not provided. Tubes within the RSC were assumed to be arranged in a square-pitch formation, with one-inch spacing between the tubes. A control system, comprised of proportional-integral (PI) controllers, was implemented for the gasifier model, and disturbances in coal-slurry flow rate and concentration were tested. It was found that the gasifier dynamics were on the order of several minutes, and tight temperature control throughout the RSC posed a challenging problem.

(Kasule et al., 2012) developed steady-state gasifier and RSC models to investigate the effect of varying coal feed parameters on the overall system. The difficulty of validation was emphasized due to the lack of published raw-syngas gasifier data (prior to exiting the gasifier quench). This one-dimensional model was developed in ACM and solved using first-order finite differences. Proper initial guesses were critical to successful initialization and model convergence. An iterative initialization procedure was used, whereby a reduced-length system was solved, and the solution was then used as the initial guess for a

larger system, until full system length was achieved. The RSC was modeled as a PFR, with design characteristics obtained from (Robinson and Luyben, 2008). The authors illustrate the progression of WGS in the RSC, but do not provide corresponding axial temperature profiles.

2.2   Steam Methane Reforming

2.2.1   SMR Process description

Steam methane reforming (SMR) is the conversion of methane (CH_4) to syngas. Natural gas (NG) is the most commonly used feedstock for reforming due to its high methane content. Methane is an attractive option for syngas production as the ratio of hydrogen atoms to carbon atoms is high, especially compared to coal. NG may also have small amounts of higher alkanes (e.g. ethane and propane); pre-reformers are commonly used to convert these compounds to methane prior to the reforming step. Methane content in NG may vary typically between 87.86 and 95.70% by volume, while C_2's and C_3's make up 0.33 to 5.26% by volume (Steynberg and Dry, 2004). Methane reforming, unlike coal gasification, is much more commercially prominent, and is a key process for supplying hydrogen in oil refineries.

Methane reforming reactions are reversible and overall highly endothermic, occurring at different rates depending on the temperature:

$$CH_4 + H_2O \leftrightarrow CO + 3H_2, \quad \left(\Delta H_{rxn,298K} = 206.3 \frac{kJ}{mol}\right) \tag{2.1}$$

$$CO + H_2O \leftrightarrow CO_2 + H_2, \quad \left(\Delta H_{rxn,298K} = -41.1 \frac{kJ}{mol}\right) \tag{2.2}$$

$$CH_4 + 2H_2O \leftrightarrow CO_2 + 4H_2, \quad \left(\Delta H_{rxn,298K} = 164.9 \frac{kJ}{mol}\right). \tag{2.3}$$
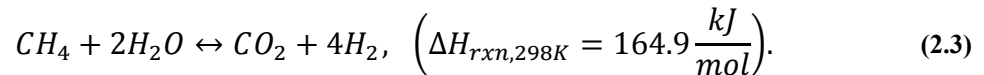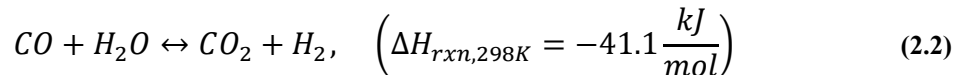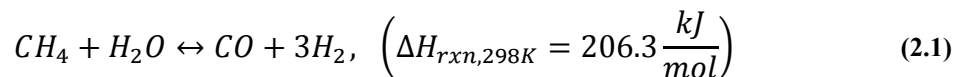
The dilemma of supplying a vast quantity of thermal energy for the reactions brings about two distinct methods of reforming: steam methane reforming and autothermal reforming (ATR). While both SMR and ATR processes require the mixing of steam with NG, ATR

processes also include an O_2 feed, which facilitates the controlled ignition of a portion of the methane in the same vessel where reforming takes place. SMR systems usually take place in radiant furnaces, though some heat exchange reformer (HER) methods have also been developed (Dybkjær, 1995; Wesenberg and Svendsen, 2007). With SMR systems, the NG-derived syngas H_2/CO ratio tends to be too high for efficient FT synthesis, and thus existing gas-to-liquids (GTL) facilities use ATR as their primary syngas producer despite the carbon losses that arise from burning part of the methane feed.

For furnace SMRs, the catalyst-filled tubes require a large thermal energy input and are located in the radiant section of the furnace. Several types of furnace designs are currently used, and there is no universally accepted optimal design (Hawkins, 2013). Side-fired SMRs tend to be more popular, due to the flexibility in adjusting heat flux along the tube length, made possible with the placement of individually-adjusted burners along the furnace walls. In top-fired designs, both the burners and process gas inlet are located at the top, employing a co-current heat exchange strategy. Bottom-fired designs have the burners located at the process gas exit, employing a counter-current heat exchange strategy. Bottom-fired SMRs are treated with caution, as tube skin temperatures tend to be much higher than in the other designs. As opposed to furnace SMRs that primarily rely on radiative heat transfer, HER designs are more compact and thus convective heat exchange dominates. In HER systems, methane reforming typically takes place within the tubes, while the heating gas flows through the exchanger shell. For thermal efficiency, the heating gas is typically obtained from some other high temperature process of the plant, such as the ATR reformed product gas (Steynberg and Dry, 2004).

2.2.2   SMR Modeling

SMRs are complex systems which necessitate the development and use of rigorous mathematical models. In particular, since the SMR process takes place at elevated temperatures and pressures, it is not possible to obtain direct measurements of conditions within the system. Thermal and chemical interactions within the bulk gas and catalyst pores need

to be accurately captured to assess performance. SMR models have been developed over the past several decades, and model rigour is continually being improved with advancements in computing power. Some of the earliest work assumed lumped, homogenous systems, while recent literature has expanded the model detail to multi-dimensional distributed, heterogeneous systems.

The earliest SMR modeling efforts focused on steady-state modeling. Singh and Saraf (1979) developed a one-dimensional homogeneous model of a side fired reformer, validating it against industrial data. A furnace radiation model was developed to calculate heat transferred to the reformer tubes using a constant furnace gas temperature. Xu and Froment (1989) described the kinetics of the SMR reactions as three reversible reactions occurring in parallel, the details of which being dependent on the gas component partial pressures within the catalyst. This kinetic expression is agreed upon by all recent works as the true kinetic model (Ghouse and Adams II, 2013; Pantoleontos et al., 2012; Pedernera et al., 2003; Rajesh et al., 2000). A one-dimensional heterogeneous model was developed, integrating along the radius of the catalyst to obtain effectiveness factors and thus estimate the actual reaction rate. The steady-state model was validated against industrial data.

Alatiqi et al. (1989) developed a one-dimensional, pseudo-homogenous steady-state model to estimate temperature, conversion and pressure profiles along the length of the reformer tube. The authors used an empirical quadratic equation to model heat transfer from furnace gas to the reformer tubes (likely just developed for their own process). The authors employed a 4th order Runge-Kutta method to solve the system. From this work, Alatiqi and Meziou (1991) developed a dynamic model of the reforming process, extended from their steady-state formulation. As such, the ordinary differential equations (ODEs) in the original system were converted to PDEs and solved using a finite differences approach. The model was compared against actual plant dynamic data in order to then use the model for control design purposes.

Pedernera et al. (2003) constructed a steady state model to investigate and improve SMR performance. This model was two-dimensional in the tube gas phase, taking into account

axial and radial variation. The model also captured radial variations within the catalyst, and utilized effectiveness factors to determine overall reaction rate. The model predicted sharp gradients in the catalyst radial profile, as the reaction only effectively takes place in the 2.5% of the catalyst volume closest to the surface. To capture these gradients, the authors utilized a custom grid, placing most nodes near the surface, and fewer nodes throughout the bulk of the catalyst. While tube gas concentration gradients were found negligible in the radial dimension of the tube, temperature gradients were significant, implying that the catalyst along the tube center was underutilized.

De Wilde and Froment (2013) developed a steady-state CFD model of a lab scale SMR. The reformer employed a dual-zone structure, where baffles exist inside the reformer in order to increase turbulence in the flow of the reformer gas and increase the uniformity of heat transfer. Due to the expense of the computation time, only a slice of the reformer cross-section was simulated along the reactor length.

All of the aforementioned models utilize the effectiveness factor as a means of predicting the actual reaction rate due to diffusional resistances. In (Ghouse and Adams II, 2013), which is the model used in this research, the authors eliminated the need to calculate effectiveness factors, by modeling the diffusional resistance within the catalyst particle using PDEs. As such, their first-principles model has a much broader application as the dependence on equipment specific parameters is removed.

2.2.3 SMR Operation and Control

The existing literature developed around control of SMR systems are primarily focused on furnace designs. Alatiqi et al. (1989) was one of the earliest works to discuss using a rigorous mathematical model to develop control for an industrial steam reformer. The critical controlled variables (CVs) included the reformer coil outlet temperature (COT) and methane conversion (expressed as % H_2 in reformer product gas). By controlling COT through the manipulation of the fuel gas flow and maintaining fixed feed gas rates, conversion could also be indirectly controlled within a certain range. For feed composition

changes, the steam-to-carbon (S/C) ratio would have to be manipulated in order to maintain tight conversion control (Alatiqi, 1990).

A single-input-single-output (SISO) control design was developed by Alatiqi and Meziou (1991), and tested using an actual industrial SMR. A process transfer function was identified by observing the effects of a step change in fuel gas on the COT. Tuning rules were tested and compared using servo (set point change) and regulatory (disturbance rejection) control, and it was observed that internal model control (IMC) tuning performed better for set point changes, while Ziegler-Nichols (Z-N) tuning performed better for load disturbances. Despite the heuristic used, all controller tunings developed with the plant operating at 100% capacity produced excessive oscillation and unacceptable controller performance at 58% plant capacity, signaling the requirement to detune the controller at the lower throughput. Conversion was not specified as a control objective in this work.

Alatiqi (1990) suggested a multi-loop control strategy for the reformer, whereby for a fixed NG feed gas rate, COT was controlled by manipulating the S/C ratio, and conversion was controlled by manipulating fuel gas flow. By performing a relative gain array (RGA) analysis, it was inferred that the loop interactions were not severe. Unfortunately, no results are available regarding the performance of this control scheme.

In (Meziou and Alatiqi, 1994), the authors build upon their previous work by considering the control of COT, conversion and steam boiler water level. In their SMR furnace, the heat from fuel gas combustion is first transmitted to the SMR tubes in the radiant section, with residual heat then transmitted to the steam boiler tubes in the convective section. The authors consider the manipulated variables (MVs) to be: S/C ratio, fuel gas rate and boiler feed water (BFW) flow rate. Step response data was used to perform system identification in the form of transfer functions, and RGA analysis was used to determine loop pairings. For system identification, autoregressive exogenous (ARX) models were used. System linearity was assessed using variable step sizes, and it was found that linearity is preserved when the relative step disturbance is less than 1%. Multiple disturbances were considered, including feed gas rate and density, feed gas temperature, fuel gas density and

BFW inlet temperature. For their system, the authors observed that by controlling the COT using the S/C ratio, overall system control performance was improved relative to the conventional method of using fuel gas as the MV. Due to the interactions between systems, the controllers required detuning, with IMC providing better results than Z-N. A recommendation was made to include feedforward control from feed gas to fuel flow.

In (Meziou et al., 1995), a dynamic matrix control (DMC) structure was developed to determine performance improvements relative to multi-loop PI control. The authors utilized the same CVs and MVs from their previous study, and also incorporated disturbance variable (DV) effects into the controller model. It was observed that input move suppression and constraints were required in the face of plant-model mismatch, thereby improving controller stability. With correctly chosen input weights, DMC provided superior performance over PI control when assessed using the integral time squared error (ITSE) measure. Following a disturbance or set point change, steady states were reached after 60-90 minutes of transient behaviour.

In contrast to previous works, Hawkins (2013) used the concept of methane (CH_4) slip as a way of expressing SMR conversion. Here, CH_4 slip refers to the percentage of CH_4 in the reformer exit gas on a dry molar basis. In this design, the fuel gas flow was used to control COT, and the S/C ratio was used to maintain CH_4 slip. Hawkins (2013) emphasized the importance of monitoring tube wall temperatures (TWT) on a daily basis, as tube failure can rapidly occur during abnormal operation. Thermocouples cannot be attached to the tube within the reformer environment due to the excessively high temperatures; consequently, pyrometers and visual inspection are used to determine the tube condition.

In line with the common control philosophy of SMR systems explored by researchers, conversion (CH_4 slip) and COT control will be implemented on the hybrid gasifier/reformer system in this work. A primary distinction between this hybrid system and conventional SMR control is the ability to adjust heat duty. For furnace SMRs, heat duty to the tubes is an MV through adjusting fuel gas firing. For the gasifier/reformer system,

heat duty, supplied by the coal-derived syngas, is a DV, and can be adopted within feed-forward control design (assuming availability of measurement). As such, for the hybrid system in this work, SMR feed flow rate must become a MV, where traditionally it is treated as a DV. Similar to previous SMR control studies, S/C ratio will be implemented as an MV to maintain conversion. While the model in this work provides tube wall temperatures within the RSC, it is assumed that online measurement cannot be implemented; the potential of indirectly controlling maximum tube wall temperatures through maintaining COT will be investigated.

2.3   Polygeneration

A polygeneration plant, broadly defined, is one that processes multiple types of fossil fuels (e.g.: coal, NG, petcoke) to generate a variety of products, such as gasoline, diesel, methanol and electricity (Adams and Barton, 2011). This type of plant offers several advantages over conventional methods of production, including but not limited to reducing worldwide dependence on in-ground oil and hedging against volatile oil prices. It can be seen as a hybridization of several existing independent technologies: integrated gasification combined cycle (IGCC), coal-to-liquids (CTL) and GTL.
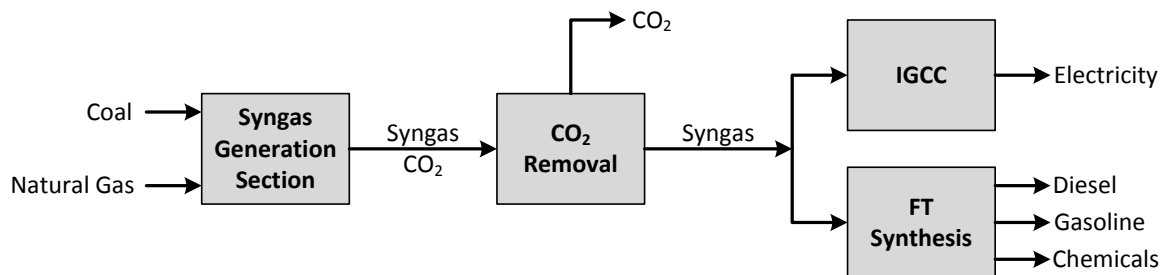
Figure 2.1: Simplified diagram of the Polygeneration Concept used in this work.

An IGCC involves the combustion of syngas derived from the gasification of coal within combustion turbines to produce electricity. The IGCC is a cleaner and more efficient power production method than the traditional Pulverized Coal (PC) combustion methods that exist today. The higher energy penalty for carbon capture and sequestration (CCS) in

a PC plant results in a net higher heating value (HHV) efficiency of 24.9%, while the IGCC plant has a net HHV efficiency of 32.5% (Woods et al., 2007). GTL facilities produce liquid fuels from NG-derived syngas generated by reforming for FT synthesis; commercial demonstrations already exist at facilities in New Zealand, Malaysia and South Africa (Aasberg-Petersen et al., 2001). Similarly, CTL plants use coal-derived syngas generated by gasification for FT synthesis. A flexible polygeneration plant, containing all of these elements, is be able to respond to product price and demand fluctuations by adjusting how the syngas is produced and to what final product it is routed. For example, in times of peak electricity demand, the plant will send more syngas to electricity production, and less to liquid fuel production. Likewise, when the demand and price of electricity fall, the syngas flows are adjusted to increase liquid fuel production.

FT reactions convert the syngas to the desired liquid products, and can either take place in high temperature (HTFT) or low temperature (LTFT) reactors. For the manufacturing of methanol, dimethyl-ether (DME) and HTFT liquids (primarily gasoline), the proportions of CO, CO_2 and H_2 in the syngas must be considered, with the desired ratio determined as (Steynberg and Dry, 2004):

$$M = \frac{(H_2 - CO_2)}{CO + CO_2},$$ (2.4)

where M should be approximately 2.0.

For the production of waxes, electric power and LTFT liquid fuels (primarily diesel), the characteristic syngas ratio of H_2/CO is desired to be 2.0. CO_2 is not considered for LTFT as it is inert for the reactor temperature range (200 to 400°C) (Dry, 2002).

In the polygeneration plant considered in this work (shown in Figure 2.1), coal gasification is used as the main syngas producer. As coal is predominantly made up of carbon, the syngas produced has a typical H_2/CO ratio ranging from 0.7 to 1.1 (Adams and Barton, 2011), which is insufficient for FT synthesis. The upgrading of coal syngas (increasing H_2

content) is hence a necessary intermediate step and can take place in several ways, with the three most economically viable options assessed by Adams and Barton (2011).

The first of these methods upgrades the coal-derived syngas itself using catalytic water-gas shift (WGS) reactors, and is the primary method used by several investigators (Botero et al., 2012; Woods et al., 2007). The WGS reaction is exothermic and occurs as follows (Adams and Barton, 2009):

$$H_2O + CO \leftrightarrow H_2 + CO_2, \ \left(\Delta H_{rxn,298K} = -41.1\frac{kJ}{mol}\right). \tag{2.5}$$
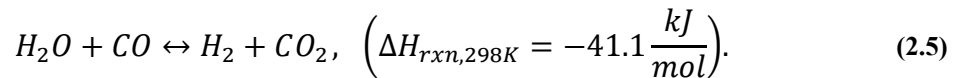
The second method, referred to as external reforming, involves including a methane reforming unit in the plant, which supplies H_2 to upgrade the coal-derived syngas (Adams and Barton, 2011). A description of the reforming process is provided in Section 2.2.1. The authors utilize an ATR as the methane reforming unit. Note that the ATR process is also used within existing GTL facilities (Steynberg and Dry, 2004). NG-derived syngas has a H_2/CO ratio of over 3.0, which can be blended with the coal-derived syngas to produce the desired FT synthesis feedstock, negating the requirement for the WGS reactor as was necessary in the first design (Adams and Barton, 2011).
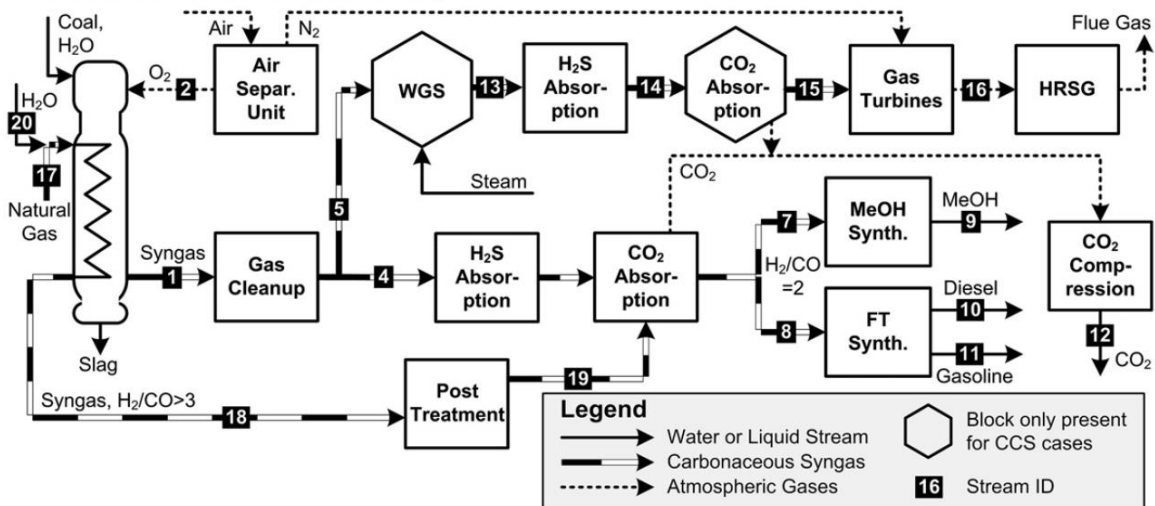
Figure 2.2: Polygeneration concept using Internal Reforming (reprinted from (Adams and Barton, 2011)).

The third method (Figure 2.2), referred to as internal reforming, performs the steam methane reforming in the RSC section of the gasifier (Adams and Barton, 2011). Current RSC designs (EPRI, 1990; McDaniel and Hornick, 2002; Woods et al., 2007) generate high-pressure steam as a by-product by sending cooling water through the radiant tubes. In this method, the RSC tubes would be filled with reforming catalyst, and a mixture of steam and NG is fed into these tubes. The high temperature coal-derived syngas, travelling through the RSC, provides the required heat duty to drive the reforming reaction and produce H_2-rich syngas ($H_2/CO > 3.0$) while simultaneously cooling the coal-derived syngas in the process. This heat exchange eliminates the need to combust NG as in the ATR case, and also negates the requirement for a WGS reactor to upgrade the H_2 content of the coal-derived syngas. A techno-economic analysis showed, for a wide range of potential electricity and gasoline prices, the internal reforming strategy was the most economically promising strategy. Adams and Barton (2011) note that, due to the extreme conditions involved, a detailed analysis of the design and operability of such a unit needs to be conducted in order to determine the feasibility of this concept. Therefore, the focus of this work is to investigate the operability of two variants of the hybrid gasifier/reformer (henceforth referred to as the RSC/SMR system), in order to determine the range of feasible or safe operations, investigate key safety criteria, and develop quality control systems to ensure that the unit can handle disturbances and changes in its operation.

Chapter 3

Model Development

This Chapter describes the details of the dynamic model developed for use in this work. Many aspects of the model have been developed in prior work (Ghouse and Adams II, 2013; Ghouse et al., 2014), and are not included in the following discussion for the sake of brevity. The aspects of the model described in this chapter are the additions made throughout this thesis project in order to render it fit for use for dynamic control studies.

3.1 Model Overview

The overall RSC/SMR model is comprised of five coupled models:

1. Shell gas phase: this model captures the flow of coal-derived syngas through the RSC, the progression of water-gas shift (WGS) reaction, and the transfer of heat from the coal-derived syngas to the tube and refractory walls.

2. Tube wall phase: this model captures the transfer of heat from the coal-derived syngas to the SMR tube-gas via conduction through the tube wall.

3. Refractory wall phase: this model captures the transfer of heat from the coal-derived syngas to the ambient via conduction through the refractory wall.

4. Tube gas phase: this model captures the flow of SMR gas through the reformer tubes, pressure drop due to the catalyst packing, heat transfer from the tube wall, and heat and mass transfer to and from the catalyst particles.

5. Catalyst phase: this model captures the diffusion of heat and mass into and out of the catalyst particle, conduction of heat throughout the particle, and the reforming reaction within the pores.

The way in which these models interact with each other can be visualized using Figure 3.1.
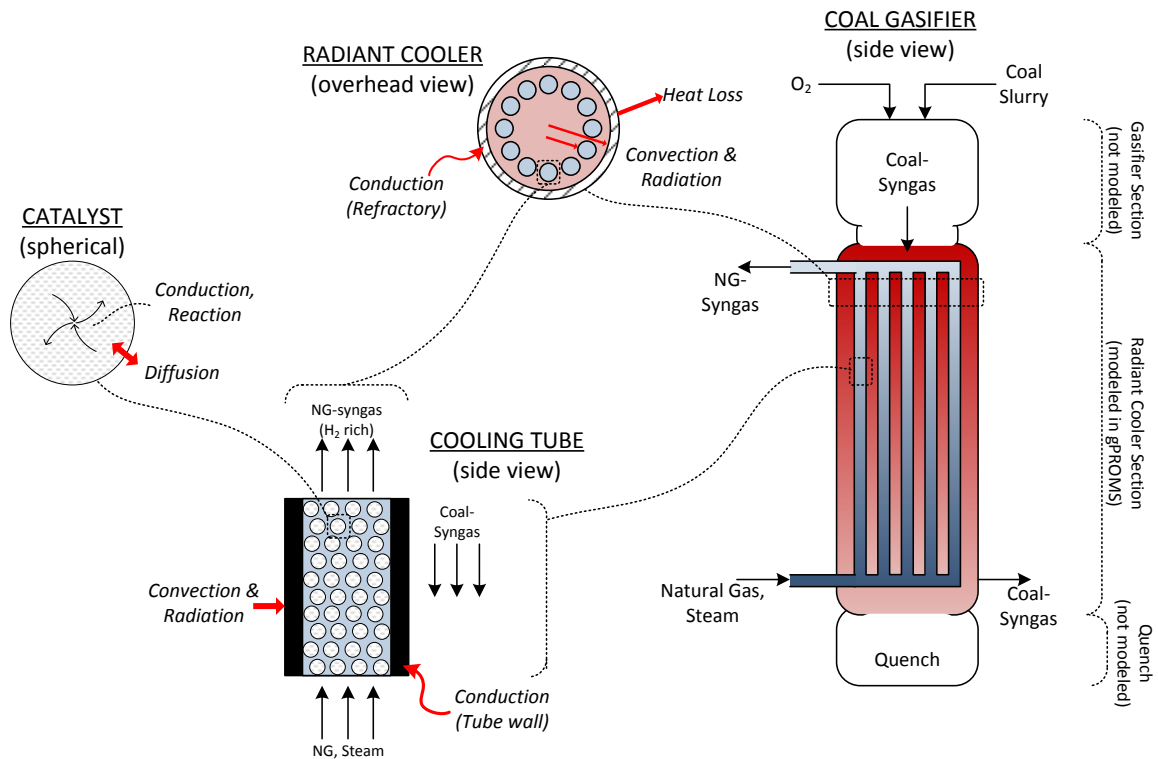
Figure 3.1: Schematic of the overall RSC/SMR model as implemented in gPROMS.

3.2   Shell Gas Phase

Several modifications were made to the shell gas model in order to accurately capture the effect of coal-derived syngas transient behaviour on the SMR tubes and refractory, as explored in chapters 4 and 5. The original RSC/SMR model as developed in (Ghouse et al., 2014) only considered the energy balance in the shell gas phase assuming fixed gasifier operation. To simulate changes in coal-derived syngas flow and composition, mass and momentum balances were developed in this work and are described in the following sections. In addition, the original RSC/SMR model made the assumption that no reactions occur throughout the shell side of the RSC. To depict coal-derived syngas composition profiles along the RSC more accurately, a study of the relevant kinetic expressions was performed, as described in section 3.2.5.

3.2.1   Shell Gas Mass Balance

The dynamic component balance for the gas within the shell side is given by:

$$\frac{\partial C_{S,i}}{\partial t} = -\frac{\partial(C_{S,i}v_S)}{\partial z} + r_{S,i},$$

(3.1)

where $C_{S,i}$ represents the concentration of species i in the shell gas, v_S is the velocity of the shell gas and $r_{S,i}$ is the rate of reaction of species i in the shell gas phase due to the WGS reactions, z is the axial location and t is time. Assuming that the shell gas can be approximated using the ideal gas law, the velocity v_S can be computed using:

$$v_S = \frac{\left(F_S^{in}RT_S\right)}{A_{CS}P_S},$$

(3.2)

where F_S^{in} is the molar flow rate of shell gas at the inlet, R is the universal gas constant, T_S is the temperature of the shell gas, A_{CS} represents the cross-sectional area of the RSC and P_S is the pressure of the shell gas. Note that A_{CS} must account for only the empty

space within the RSC where the shell gas is permitted to travel, and will vary depending on the number of tubes used and their diameters.

3.2.2   Shell Gas Energy Balance

The energy balance of the shell gas phase was developed in prior work (Ghouse et al., 2014), which is shown here for the sake of completeness:

$$\frac{\partial H_S}{\partial t} = -v_s \frac{\partial H_S}{\partial z} - \frac{N_t}{\rho_S A_{CS}} \left(Q_{conv,S \to W} + Q_{rad,S \to W} \right)$$
$$- \frac{1}{\rho_S A_{CS}} \left(Q_{conv,S \to R} + Q_{rad,S \to R} \right),$$

(3.3)

where H_S represents shell gas enthalpy, N_t represents number of SMR tubes in the RSC, ρ_S is shell gas molar density, $Q_{conv,S \to W}$ is the convective heat transfer from shell gas to the tube walls, $Q_{rad,S \to W}$ is the radiative heat transfer from shell gas to the tube walls, $Q_{conv,s \to W}$ is the convective heat transfer from shell gas to the refractory wall and $Q_{rad,S \to W}$ is the radiative heat transfer from shell gas to the refractory wall. Note that despite there being a reaction term within the mass balance of equation (3.1), such a term is not visibly present in the energy balance of equation (3.3). This is due to the heat of reaction being implicitly accounted for by the calculation of the shell gas enthalpy (H_S).

3.2.3   Shell Gas Momentum Balance

As discussed in prior work (Adams and Barton, 2009; Ghouse and Adams II, 2013), the inclusion of a rigorous momentum balance results in a very stiff system of equations that becomes difficult to solve. Robinson and Luyben (2008) and others have also shown that the pressure drop within the RSC is small in comparison to the pressure drop within the SMR tubes. As such, the pseudo-steady-state form was employed:

$$\frac{\partial P_S}{\partial z} = -\frac{\Delta P_S}{L},$$

(3.4)

where ΔP_S is the pressure drop across the length of the RSC, and L is the RSC length. Previous researchers consistently estimated a 1 bar pressure drop across the length of the RSC (Monaghan and Ghoniem, 2012b; Robinson and Luyben, 2008; Woods et al., 2007), which was also used in this study.

3.2.4   Shell Gas Boundary Conditions

The boundary conditions for the shell gas phase are provided at the inlet at $z = 0$:

$$C_{S,i}|_{z=0} = C_{S,i}^{in} \qquad (3.5)$$

$$T_S|_{z=0} = T_S^{in} \qquad (3.6)$$

$$P_S|_{z=0} = P_S^{in}. \qquad (3.7)$$

3.2.5   Shell Gas Reaction Kinetics

The original RSC/SMR model as developed in (Ghouse et al., 2014) made the assumption that no reactions occur in the shell gas throughout the length of the RSC. However, the WGS reaction is known to occur along the RSC length, due to the high temperature of the coal-derived syngas exiting the partial oxidation section (POX) of the gasifier (Kasule et al., 2012; Monaghan and Ghoniem, 2012b; Robinson and Luyben, 2008). In particular, the equilibrium of the WGS reaction shifts with the gradually decreasing temperatures, favouring the production of H_2 and CO_2; this is a desired effect within a polygeneration plant, as the H_2/CO ratio of the coal-derived syngas also increases with progression of WGS. While researchers agree on the importance of modeling the WGS reaction, the few studies available in open literature on homogeneous WGS kinetics are in considerable disagreement regarding the structure of the kinetic expression. In contrast, heterogeneous WGS kinetics are much more understood and investigated, yet only apply to catalytic WGS reactors, which operate at a far lower temperature range than the RSC.

Other reactions (such as methanation) also occur within the RSC, but were found to have negligible impact on the predicted coal-derived syngas composition (Robinson and

Luyben, 2008); in line with common practice (Kasule et al., 2012; Monaghan and Ghoniem, 2012b), these less significant reactions will not be modeled in this work. The subsequent discussion is thus focused on four different WGS kinetic expressions posed by researchers in the field, those of: Monaghan (Monaghan and Ghoniem, 2012b), Luyben (Robinson and Luyben, 2008), Bockelie (Bockelie et al., 2004) and Bustamante (Bustamante et al., 2004, 2005). Of these, only Monaghan provides axial shell mole-fraction profiles along the RSC length.

Monaghan developed a detailed dynamic model of the coal gasifier and RSC, providing the kinetics for the homogeneous WGS reaction as follows (Monaghan and Ghoniem, 2012b):

$$r_{WGS} = 7.40 \times 10^{17} \exp\left(-\frac{34674}{T}\right)\left(\left(\frac{C_{CO}}{10^6}\right)^{0.5}\left(\frac{C_{H_2O}}{10^6}\right) - \frac{1}{K_{eq}}\left(\frac{C_{CO_2}}{10^6}\right)\left(\frac{C_{H_2}}{10^6}\right)\right), \quad \textbf{(3.8)}$$

where T is in Kelvin, C is in mol m^{-3}, and r_{WGS} is provided in mol m^{-3} s^{-1}.

Monaghan mentions that the kinetic expression in (3.8) was developed by Bustamante (Bustamante et al., 2005). However, in (Monaghan and Ghoniem, 2012a), the authors state that the computed rate of reaction from equation (3.8) had to be "tuned to 0-8% of the rate calculated by Bustamante's expression" for all simulation studies, providing no justification for why this tuning had to be used. When adopting the kinetics from equation (3.8) for the model in this thesis, the progression of WGS was grossly overestimated without the use of a tuning factor. As shown in Figure 3.2A, it was found that by using a tuning factor of 3% of the calculated rate and adopting RSC inlet mole fractions determined by Monaghan, the model in this work obtains similar WGS dynamics to the profile exhibited by Monaghan and Ghoniem (2012c). The RSC exit mole fractions obtained through using Monaghan's kinetics come close to the NETL reported exit conditions, as shown in Figure 3.3.
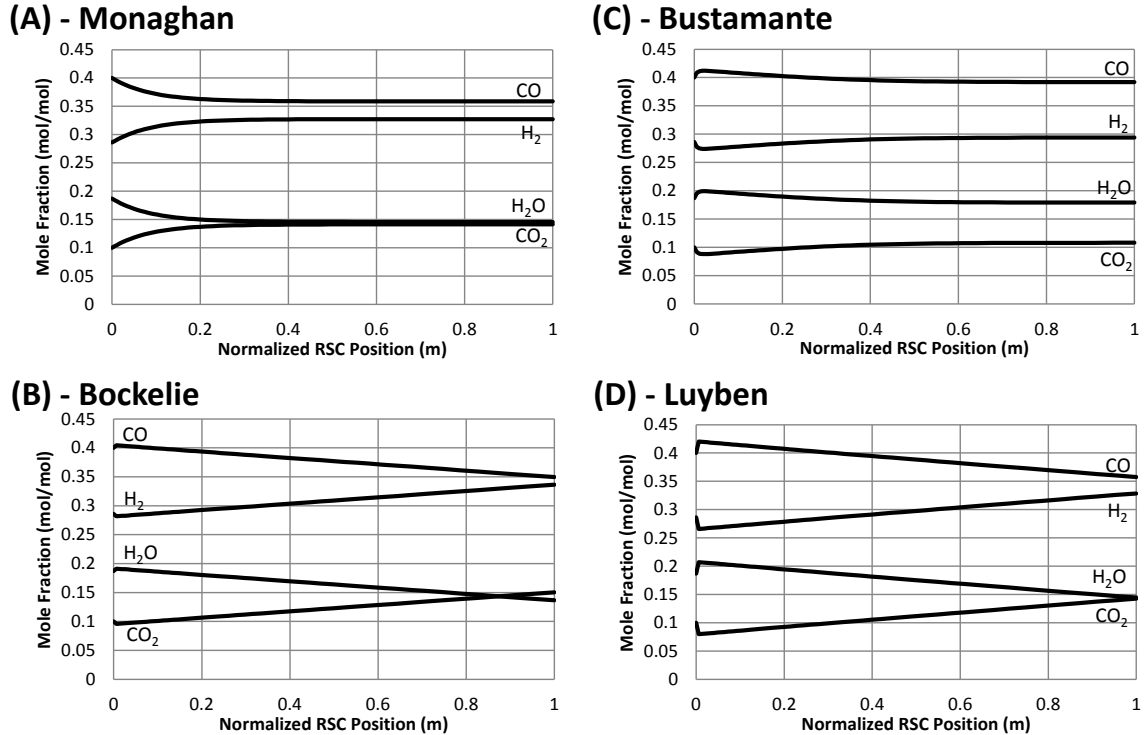
Figure 3.2: Comparison of different homogeneous WGS kinetic expressions within the Radiant Syngas Cooler.

Upon inspection of the WGS kinetics defined in (Bustamante et al., 2004, 2005), it was found that significant differences exist between Bustamante's expression and what Monaghan adopted. Bustamante's expression was developed for membrane reactors between the temperature range of $1,070 - 1,198$ K, which may not be applicable to certain conditions in the industrial gasifier RSC, which operates anywhere from $1,033 - 1,589$ K. It would appear that Bustamante's work may have been misinterpreted by Monaghan. Bustamante et al. (2005) identified that the forward WGS reaction has a non-elementary dependence on CO and H_2O, but the same applies to H_2 and CO_2 for the reverse reaction. The forward reaction was correctly interpreted from Bustamante by Monaghan:

$$r_{WGS,forward} = k_F \exp\left(-\frac{E_F}{RT}\right)\left(C_{CO}^{0.5} C_{H_2O}\right). \tag{3.9}$$

However, the reverse WGS reaction was provided by Bustamante to follow the rate law (Bustamante et al., 2004):

$$r_{WGS,reverse} = k_R \exp\left(-\frac{E_R}{RT}\right)(C_{CO_2}C_{H_2}^{0.5}),$$ (3.10)

where the power of concentration of H_2 in Bustamante's expression is different to what Monaghan adopted. Using the kinetic expressions as defined by Bustamante, the axial composition profiles can be seen in Figure 3.2C. There is significant reverse WGS reaction near the RSC inlet; this occurs because the assumed inlet mole fractions, which were previously in equilibrium with the kinetic expression of equation (3.8), are no longer in equilibrium with Bustamante's actual kinetic expression of equation (3.9) and (3.10). As a result, the resulting composition profiles in Figure 3.2C are an artifact of the model due to the specified boundary conditions, and do not represent a physical result. The reaction does revert to forward WGS soon after, but overall WGS progression is very slow. The mole fractions at the RSC exit are not very different from the inlet mole fractions, and do not match well with the NETL reported syngas compositions (Figure 3.3). The work in (Bustamante et al., 2004, 2005) was developed for membrane reactors, which remove H_2 from the system as the gas progresses along the length of the reactor, and thus may not be indicative of RSC environments.

Robinson and Luyben (2008) expressed difficulty in obtaining reliable homogeneous WGS kinetics. As such, the authors adopt heterogeneous kinetics as developed by Choi and Stenger (2003), adjusting it for use in the RSC by converting the expression to:

$$r_{WGS,forward} = k_F \exp\left(-\frac{E_F}{RT}\right)P_{CO}P_{H_2O}$$ (3.11)

$$r_{WGS,reverse} = k_R \exp\left(-\frac{E_R}{RT}\right)P_{CO_2}P_{H_2},$$ (3.12)

where $k_F = 1.612 \times 10^{-2}$ mol s^{-1} m^{-3} Pa^{-2}, $E_F = 47,400$ J mol^{-1}, $k_R = 1.224$ mol s^{-1} m^{-3} Pa^{-2}, $E_F = 85,460$ J mol^{-1}, and P is the partial pressure of the component in Pa. As the original kinetic expression was heterogeneous, a catalyst density had to be assumed to convert

the reaction rate units from mol g^{-1} h^{-1} to mol m^{-3} s^{-1}. The catalyst properties used to convert the rate parameters were not provided by the authors. Testing the kinetic expressions in (3.11) and (3.12) with the RSC model in this work yielded the axial mole fraction profile shown in Figure 3.2D. As observed previously using Bustamante's kinetics, the RSC inlet compositions are not at equilibrium with the specified inlet temperature, thus causing initially rapid reverse WGS; however, the exit coal-derived syngas compositions approach the NETL reported values (Figure 3.3). There is no axial profile provided in (Robinson and Luyben, 2008) to verify the result of Figure 3.2D.
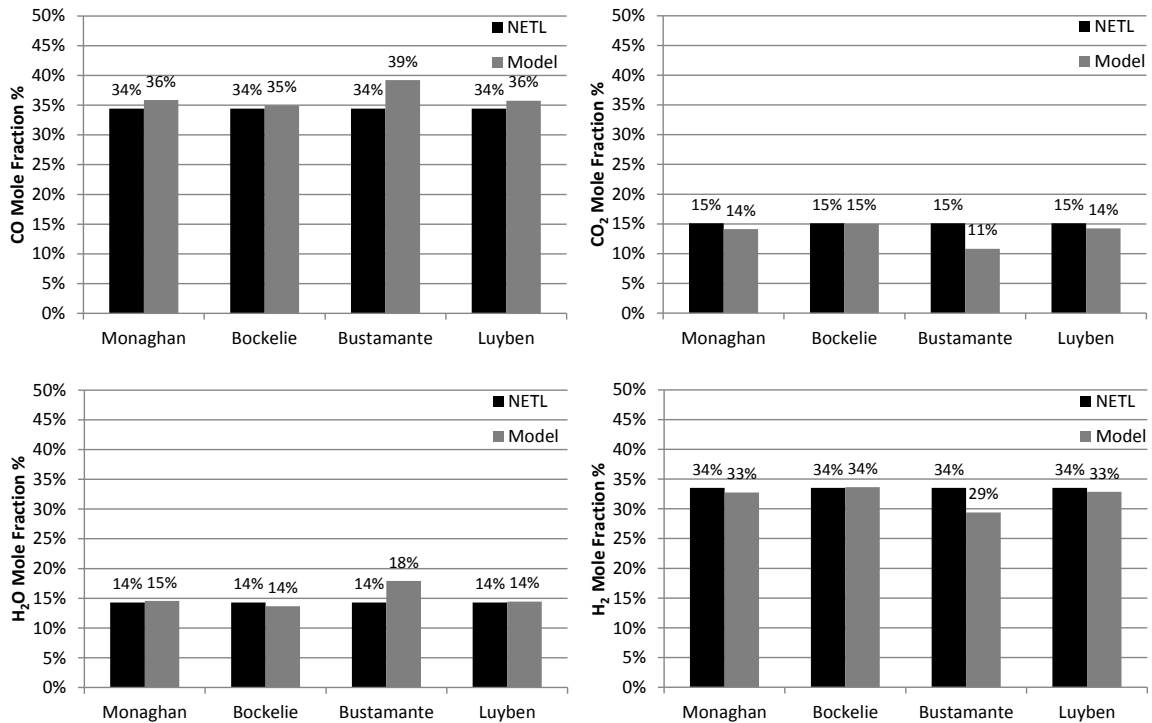

Figure 3.3: Comparison of coal syngas mole fractions at RSC exit following WGS reaction. Black represents the reported NETL figures. Grey represents the result from using the specified author's kinetic expression.

In (Bockelie et al., 2004), CFD simulations of the gasifier and RSC were developed utilizing kinetic expressions for the WGS reaction developed by Jones and Lindstedt (1988):

$$r_{WGS} = k \cdot \exp\left(-\frac{E}{RT}\right)\left(C_{CO}C_{H_2O} - \frac{1}{K_{eq}}C_{CO_2}C_{H_2}\right) \tag{3.13}$$

where $k = 2.75 \times 10^{12}$ mol s^{-1} m^{-3}, $E/R = 10{,}100$ K and the equilibrium constant is determined as:

$$K_{eq} = \exp[470.8524 - 175.8711(lnT) + 21.95011(lnT)^2$$
$$- 0.9192934(lnT)^3]\,. \tag{3.14}$$

Axial mole fraction profiles from using this reaction scheme in the RSC model of this thesis are shown in Figure 3.2B. The simulated exit mole fractions using this scheme is the closest to the NETL reported figures (Figure 3.3). Note that the kinetic expression used by Bockelie was initially used in (Monaghan and Ghoniem, 2012b), but Monaghan switched to using Bustamante's expression upon observing overly rapid progression of WGS. However, by comparing Figure 3.2A to Figure 3.2B, it can be seen that Monaghan's kinetic expression results in faster WGS progression than Bockelie's.

It is difficult to truly validate these results, as there is no available experimental data on the axial profiles of the coal-derived syngas throughout the RSC for the industrial gasifier. The inlet conditions to the RSC are also just an estimation, rather than industrial or experimental data (also unavailable in the open literature), but the results from Monaghan's gasifier model closely match Bockelie's in terms of coal-derived syngas properties exiting the POX chamber.

Thus, the rate expression used by Bockelie as shown in equations (3.13) and (3.14) was adopted in this work, as it provided results which were closest to the NETL mole fractions in the expected temperature range, without requiring tweaks or modifications of the original kinetic expression to do so.

3.3 Tube Wall and Refractory Phase

In prior work (Ghouse and Adams II, 2013), the necessity of utilizing a dynamic distributed wall model in order to assess transient behavior of different points within and along the tube wall was explained. This requirement can also be extended to the refractory phase, where typical refractory materials cannot handle a temperature change rate greater than 10 K min^{-1} (Monaghan and Ghoniem, 2012c). While the original RSC/SMR model utilized a thin slab approximation for the tube and refractory walls (Ghouse et al., 2014), this was found to be a source of error when assessing the heat transfer from the shell gas to the tube gas, as illustrated in Figure 3.4 and discussed in Section 3.3.1. Due to this finding, a two-dimensional radial model was developed in this work for the tube wall, defined as follows:

$$\rho_W C_{p,W} \left[\frac{\partial T_W}{\partial t} \right] = \lambda_W \left[\frac{1}{r_W} \frac{\partial}{\partial r_W} \left(r_W \frac{\partial T_W}{\partial r_W} \right) + \frac{\partial T_W}{\partial z^2} \right], \tag{3.15}$$

where ρ_W is the tube wall density, $C_{p,W}$ is the tube wall heat capacity, λ_W is the tube wall thermal conductivity, T_W is the tube wall temperature and r_W is the radius of the tube wall. Analogous to the tube wall model, the refractory wall model is derived as:

$$\rho_R C_{p,R} \left[\frac{\partial T_R}{\partial t} \right] = \lambda_R \left[\frac{1}{r_R} \frac{\partial}{\partial r_R} \left(r_R \frac{\partial T_R}{\partial r_R} \right) + \frac{\partial T_R}{\partial z^2} \right], \tag{3.16}$$

where ρ_R is the refractory density, $C_{p,R}$ is the refractory heat capacity, λ_R is the refractory thermal conductivity, T_R is the refractory temperature and r_R is the radius of the refractory.

The boundary conditions for the radial wall model are defined differently from the thin slab approximation as used in (Ghouse and Adams II, 2013), and are now determined by the inner radius (R_i) and outer radius (R_o) of the tube. For the tube wall model in equation (3.15), continuity in the heat flux between the inner tube wall and the tube gas boundary is defined at $r_W = R_i, t > 0$ and $\forall\, z \in [0, L]$:

$$\lambda_W \left[\frac{\partial T_W}{\partial r_W}\right]_{r_w=R_i} = h_T\big(T_W|_{r_w=R_i} - T_T\big). \tag{3.17}$$

Continuity in the heat flux between the shell gas and the outer tube wall boundary is defined at $r_W = R_o$, $t > 0$ and $\forall\, z \in [0, L]$:

$$\lambda_W \left[\frac{\partial T_W}{\partial r_W}\right]_{r_w=R_o} = \sigma \epsilon_S \epsilon_T\big(T_S^4 - T_W^4|_{r_w=R_o}\big) + h_S\big(T_S - T_W|_{r_w=R_o}\big). \tag{3.18}$$

For both ends of the tube along the axial domain, the boundary conditions are defined at $z = 0$ and $z = L$, $t > 0$ and $\forall\, r_W \in [R_i, R_o]$:

$$\left[\frac{\partial T_W}{\partial z}\right]_{z=0} = \left[\frac{\partial T_W}{\partial z}\right]_{z=L} = 0. \tag{3.19}$$

Similar adjustments were made to the refractory model boundary conditions, as elaborated upon in (Ghouse et al., 2014).

3.3.1   Radial Wall Model vs. Thin Slab Model

To evaluate the performance of the radial model versus the thin slab model for the tube wall, the heat flux was compared between the inner wall and the outer wall of the tube. Figure 3.4 illustrates this comparison.

For both tube wall model variants, the RSC/SMR model was initialized by setting concentration, temperature and pressure values throughout the system equal to the inlet boundary conditions. Once the system was initialized at this arbitrary state, the dynamic simulation was run for a sufficient length of time to obtain true steady-state profiles that correspond to the chosen inlet conditions. This method of obtaining a steady-state solution is standard procedure adopted by gPROMS model developers, as initializing a system at steady-state is too difficult for such a complex model, and frequently results in simulation failure. While the dynamic transients from the arbitrary initial state to the steady-state are meaningless, it allows for meaningful steady-state results to be consistently obtained.

At steady-state, the heat accumulation term within the tube wall becomes zero, and heat flux at the inner wall must exactly match the outer wall heat flux. As seen in Figure 3.4A, the heat flux terms for both sides of the tube wall match exactly using the radial model. However, as seen in Figure 3.4B, there is an average mismatch of 13.5% between the fluxes using the thin slab model. In this scenario, the impact of the heat transfer error using the thin slab model is significant, with CH_4 conversion (X_{CH_4}) for the RSC/SMR system being under-predicted by 5.64 percentage points. As such, the radial tube and refractory models were adopted throughout this work.
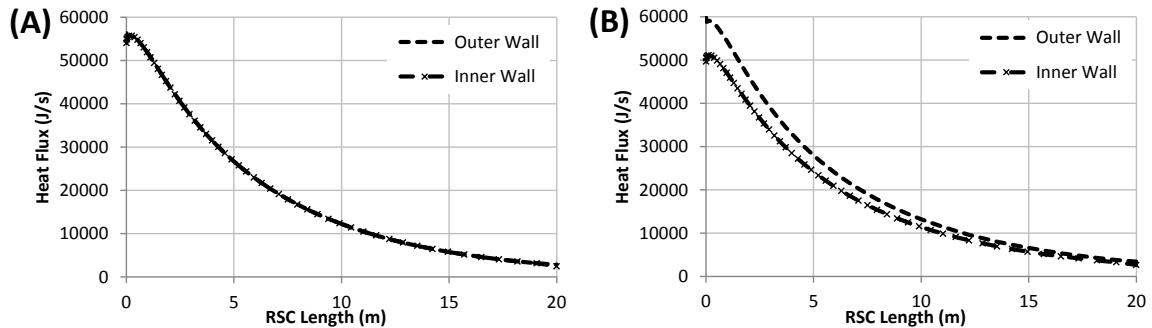
Figure 3.4: Comparison of heat fluxes observed at the inner tube wall and outer tube wall. (A) shows the heat flux comparison using radial wall model. (B) shows the comparison using the thin slab approximation.

3.4   Tube Gas Phase

3.4.1   Tube Gas Model Additions

The tube gas model used in this work is largely adopted from a prior study (Ghouse and Adams II, 2013). The key difference established in this work is the implementation of a direction term which indicates if the tube gas is flowing in co-current or counter-current mode, relative to the shell gas phase.

Some auxiliary equations were necessary to add in order to facilitate the implementation of a suitable control structure. These equations are described below:

The feed to the SMR tube inlet is described as:

$$F_{SMR} = F_{NG} + F_{STM}, \tag{3.20}$$

where F_{SMR} is the total inlet molar flow rate into the SMR tube, F_{NG} is the inlet flow rate of the NG feed to the tube, and F_{STM} is the steam inlet molar flow rate. Steam-to carbon-ratio, denoted as $R_{S/C}$, is an important definition required for SMR control, specified as follows:

$$R_{S/C} = \frac{F_{STM}}{F_{NG} y_{NG,CH_4}}, \tag{3.21}$$

where y_{NG,CH_4} represents the mole fraction of CH_4 in the NG feed. It is useful to deter-mine the dry mole fraction of the SMR gas throughout the tube, to be able to estimate the conversion of CH_4 to H_2 and CO_2 independently of steam:

$$y_{T,i,dry} = \frac{F_T y_{T,i}}{F_T (1 - y_{T,H_2O})}, \tag{3.22}$$

where F_T is the tube gas molar flow rate along the tube, and $y_{T,i}$ is the mole fraction of the ith component in the tube gas. Two indicators of CH_4 conversion for the SMR tubes are adopted in this work. The first, referred to as CH_4 slip and denoted as y_{CH_4}, is derived as:

$$y_{CH_4} = y_{T,CH_4,dry}^{out}. \tag{3.23}$$

The second measure of CH_4 conversion commonly used in the literature, namely X_{CH_4}, is defined as:

$$X_{CH_4} = \frac{F_{T,CH_4}^{in} - F_{T,CH_4}^{out}}{F_{T,CH_4}^{in}}. \tag{3.24}$$

3.4.2   Tube Gas Boundary Conditions

The tube gas model was modified to allow the flexibility of choosing co-current or coun-ter-current flow, relative to the shell gas phase, through specification of a direction varia-

ble (dir). Recall that the shell gas phase has a fixed inlet boundary at $z = 0$. For counter-current flow, the tube gas boundary conditions are given as:

$$C_{T,i}|_{z=L} = C_{T,i}^{in} \tag{3.25}$$

$$T_T|_{z=L} = T_T^{in} \tag{3.26}$$

$$P_T|_{z=L} = P_T^{in}. \tag{3.27}$$

For co-current flow, the tube gas boundary conditions are given as:

$$C_{T,i}|_{z=0} = C_{T,i}^{in} \tag{3.28}$$

$$T_T|_{z=0} = T_T^{in} \tag{3.29}$$

$$P_T|_{z=0} = P_T^{in}. \tag{3.30}$$

The direction variable (dir) is used to select the appropriate boundary conditions as follows:

$$z = \frac{1}{2}(dir + 1)(L). \tag{3.31}$$

For counter-current flow, $dir = +1$ and $z = L$. For co-current flow, $dir = -1$ and $z = 0$.

3.4.3   Use of Smoothing Function for Discontinuity

The equation describing the flow of heat between the tube gas phase and the catalyst phase due to diffusion of gases posed numerical difficulties for the solver. This diffusion phenomenon was described by an IF/ELSE statement within the original model as follows (Ghouse and Adams II, 2013):

IF $C_{T,i} > C_{c_{i,surf}}$ THEN

$$Q_i = -\frac{H_{T,i}k_i(C_{T,i} - C_{c_i,surf})a_v}{\varepsilon} \tag{3.32}$$

ELSE

$$Q_i = -\frac{H_{c,i}k_i\left(C_{T,i} - C_{c_i,surf}\right)a_v}{\varepsilon} \tag{3.33}$$

END

When the concentration of gas is greater in the bulk gas phase than in the catalyst phase at the surface $(C_{T,i} > C_{c_i,surf})$, gas diffuses into the catalyst, and the enthalpy of the bulk gas phase $(H_{T,i})$ is used to compute the ith gas component heat transfer (Q_i). When the concentration of gas in the catalyst phase is greater $(C_{T,i} < C_{c_i,surf})$, gas diffuses out of the catalyst, and the enthalpy of the catalyst gas phase $(H_{C,i})$ is used to compute Q_i.

With this `IF/ELSE` expression, every instance the direction of gas flow changes, this introduces a discontinuity in the system, forcing the solver in `gPROMS` to reinitialize the model at that instance. During a typical transient run, this was observed many hundreds of times, at different axial locations along the tube. The presence of an inert (N_2) often exacerbates this issue. Even though the difference in concentration between the catalyst and bulk gas may be effectively zero, the actual number reported during simulation fluctuates between $\pm 1 \times 10^{-15}$ mol m^{-3}, at infinitesimally small time steps, causing the simulation to stall.

The solution to this numerical problem is to use a smoothing function to replace the `IF/ELSE` statement, formulating it as follows:

$$\alpha = \frac{1}{2}\left[1 + tanh\left(C_{T,i} - C_{c_i,surf}\right)\right] \tag{3.34}$$

$$H_{move} = \alpha H_{T,i} + (1 - \alpha)H_{c,i} \tag{3.35}$$

$$Q_i = -\frac{H_{move}k_i\left(C_{T,i} - C_{c_i,surf}\right)a_v}{\varepsilon}, \tag{3.36}$$

where α is a switching parameter. When $C_i > C_{c_i,surf}$, α tends towards 1 and H_{move} takes the value of the bulk gas phase enthalpy ($H_{T,i}$). When $C_i < C_{c_i,surf}$, α tends towards 0 and H_{move} takes the value of the catalyst phase enthalpy ($H_{C,i}$). As $C_i \rightarrow C_{c_i,surf}$, $\alpha \rightarrow 0.5$ and

H_{move} becomes an average enthalpy between the catalyst and bulk gas phases. In this scenario however, the value of H_{move} becomes inconsequential as the concentration difference term in equation (3.36) will be zero, resulting in a net heat transfer term (Q_i) of zero.
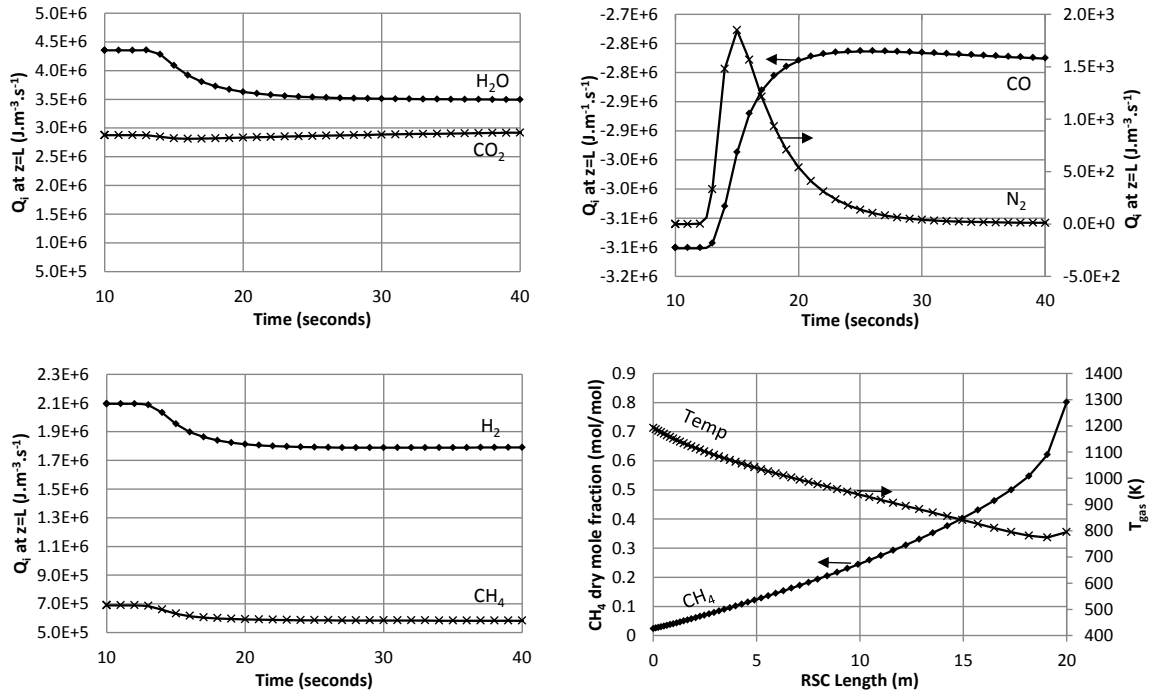

Figure 3.5: Comparison of results using smoothing function. Solid lines represent results obtained from `IF/ELSE` statement. Data points represent results obtained from $tanh$ smoothing function.

Figure 3.5 illustrates the results obtained from the two methods of calculating heat transfer of diffused gas. At ten seconds into the simulation, the composition of the SMR feed is changed, and its effects observed over thirty seconds. As a result, the concentrations throughout the tubes change, and Q_i also changes to reflect this. For all six gas components, the smoothing function approximation is able to capture the full range of movement in Q_i observed using the `IF/ELSE` method (Figure 3.5). Note that the Q_i for N_2 has a swift and significant peak at five seconds after the feed change, which the smoothing function was able to capture. The axial profiles are largely unchanged, and for the purposes of this investigation, both methods of calculating Q_i yield the same result. Simulating

this run using the `IF/ELSE` function results in a simulation time of 592 seconds. By switching to the smoothing function, simulation time was reduced by 90%, to 57 seconds. The smoothing function was hence used for the remainder of this study.

3.5   Catalyst Phase

The catalyst model has been adopted as is from a prior work. Please refer to (Ghouse and Adams II, 2013) for model details.

3.6   Mesh Choice Study (Analysis of Numerical Resolution)

The multi-scale, multi-dimensional nature of the coupled models makes finding an accurate solution especially challenging, demanding an appropriate discretization method for each model. The major issues associated with discretization of each model are discussed below.

3.6.1   Catalyst Model

Gaseous diffusion into and out of the catalyst pores is a key phenomenon of the SMR system. Significant care must be taken in selecting an appropriate discretization method for solution of the catalyst model. Within the catalyst particle, the reactions mainly take place close to the surface, within the initial 2.5% of the particle depth (Pedernera et al., 2003). These steep diffusion gradients, as captured using various grid specifications, are illustrated in Figure 3.6. A 25 node linear grid (which was originally used in prior work) is largely unable to capture the diffusion front, while using a finer linear grid of 350 nodes captures the gradient well, but at the expense of computation time.

Within `gPROMS`, a custom grid can be employed to allow for irregular node placements. After some experimentation and analysis, a custom grid was developed that provides excellent accuracy whilst minimizing simulation time. Figure 3.7 illustrates the node place-

ment of this custom grid, with 8 nodes contained within the initial 5% depth from the catalyst surface, and 10 nodes evenly spaced throughout the remaining 95%. As seen in Figure 3.6, the 18 node custom grid yields a very similar intra-particle radial profile to the 350 node linear grid, albeit with some loss of smoothness.
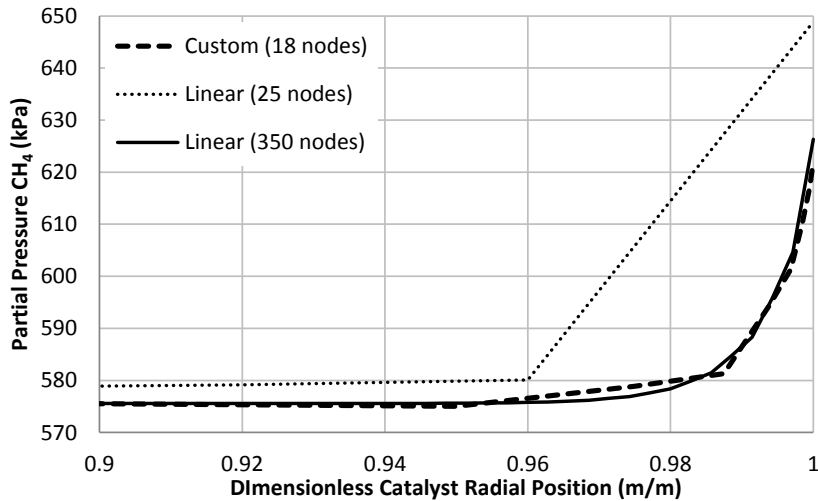
Figure 3.6: Radial profile of CH$_4$ partial pressure within the catalyst using various discretization grids. Dimensionless catalyst radial position of 0 represents the catalyst core, while 1 represents the catalyst surface.
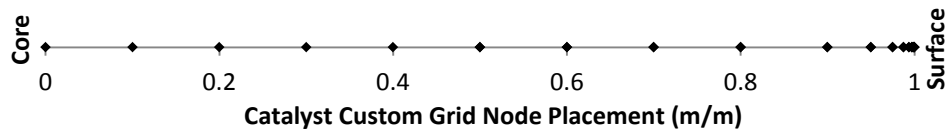
Figure 3.7: Illustration of the custom grid used to discretize the radial dimension of the catalyst particle. Dimension is normalized such that 0 represents the catalyst core, and 1 represents the catalyst surface.

Figure 3.8 illustrates the impact of increasing mesh fineness on the overall CH$_4$ conversion (X_{CH_4}) predicted. Using a linear grid, conversion varies significantly depending on the number of nodes used. If the 350 node linear grid result is taken as the 'exact' solution, the error in CH$_4$ conversion using a 25 node linear grid is as much as 7 percentage points, with a corresponding temperature error in the SMR exit gas of 33 K. However, when using a custom grid, increasing the number of nodes throughout the catalyst core

results in negligible change in predicted CH_4 conversion (Figure 3.8). It can be seen that the custom and linear grid predictions for CH_4 conversion converge towards an asymptotic value of approximately 86% as the node count increases.
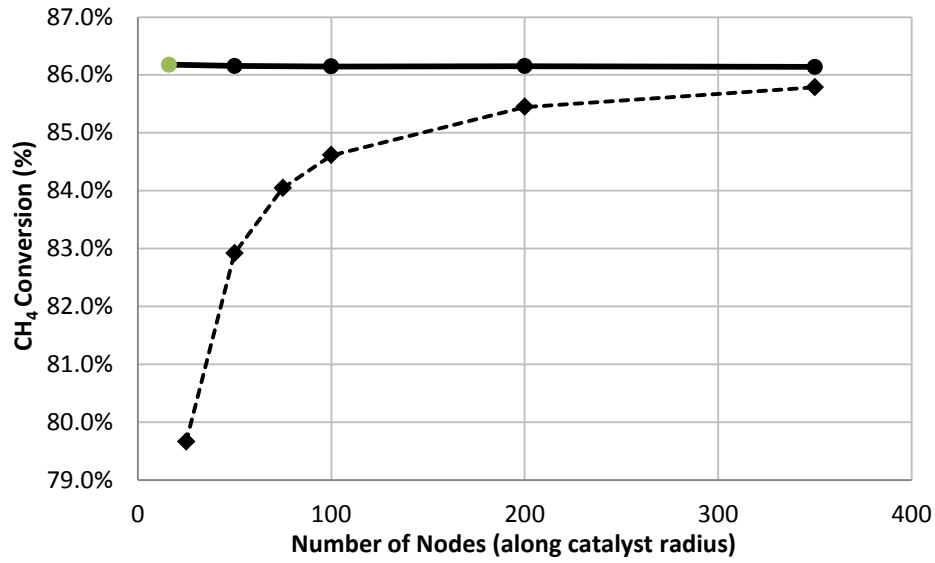
Figure 3.8: CH_4 conversion vs. number of radial nodes for the catalyst model, using a selection of linear and custom grids. The 18 node custom grid (denoted by the green circle) was used for all subsequent simulations in the thesis.

Table 3.1: Simulation results for selected catalyst grids.

Grid Type	# Nodes	T_{gas} (K)	X_{CH_4} (%)	CPU Time (s)
Linear	25	1217.8	79.7	84
Linear	350	1185.2	85.8	609
Custom	18	1182.2	86.2	77
Custom	350	1182.0	86.1	953

Table 3.1 summarizes observed simulation results and run times for selected catalyst grids. The 18 node custom grid provides similar profiles compared to the 350 node linear and custom grids, while taking the least amount of time to run. Note that minor oscillations were observed in intra-particle temperature, pressure and concentration profiles throughout the catalyst depth for all investigated grids; this is a result of the accumulation

40

of numerical error associated with the use of finite difference approximations for converting the PDEs to ODEs. Orthogonal collocation on finite elements (OCFE) was another discretization method investigated for the catalyst model, and was found to eliminate this oscillation while providing smoother radial profiles. However, OCFE was exceedingly difficult to initialize in most cases, and provided approximately the same conversion predictions as the finite difference methods with longer simulation times.

For the catalyst model, the finite differences method with an 18 node custom grid was used throughout the remainder of this investigation.

3.6.2   Refractory and Tube Wall Model

The tube wall and refractory wall model posed no challenges with respect to discretization of the PDEs; this has also been observed in models developed by other researchers (Coletti and Macchietto, 2011). As such, centered finite differences was used for both refractory and tube wall radial discretization. 10 nodes were found to be sufficient, and increasing the node count produced no appreciable difference in results.

3.6.3   Shell and Tube Gas Discretization

Since the shell gas and tube gas models are integrated along the axial domain, they both must use the exact same node placement. Using the aforementioned custom grid for the catalyst model, the number of axial nodes was varied between 25 and 200. Assuming 200 axial nodes gives an 'exact' solution of the system, using 50 axial nodes results in 0.4% error in the exit tube gas temperature, and 1.0% error in CH_4 conversion for a counter-current system. With the co-current system, using 50 nodes results in 0.2% error in the exit tube gas temperature, and 0.4% error in CH_4 conversion.

An additional measure of the accuracy of the discretization is to analyze the overall energy balance of the RSC/SMR system. The refractory model is not considered in this case

in order to simulate the RSC/SMR as an adiabatic system. The method used to assess the energy balance is:

$$Q_{error} = \frac{\left(F_S^{in} H_S^{in} - F_S^{out} H_S^{out}\right) - \left(F_T^{out} H_T^{out} - F_T^{in} H_T^{in}\right)}{F_S^{in} H_S^{in} - F_S^{out} H_S^{out}}. \tag{3.37}$$

Here, F represents the molar flow rate of the stream, and H is the stream molar enthalpy. To close the energy balance, the model should predict at steady-state that the heat removed from the shell gas phase is equivalent to the heat gained by the tube gas phase. The energy balance error (Q_{error}) using 50 nodes is -2.7% for the counter-current system, and +0.1% for the co-current system, where a negative error indicates more heat gained by the tube gas than lost by the shell gas. As the refractory model is excluded in this analysis, Q_{error} should trend toward 0% as the axial discretization becomes finer. The error magnitude is larger for the counter-current system, due to the increased numerical difficulty associated with solving the opposing flows through finite difference approximations. While increasing to 200 nodes can decrease Q_{error} below 1% for the counter-current configuration, the increased computation time greatly outweighs the minor gains in accuracy.

Chapter 4

Base Case and Control

The goal of this Chapter is to provide insight into the steady-state and dynamic operation of the RSC/SMR hybrid system, and to assess its feasibility of design and operability. As the RSC/SMR hybrid system is still in the conceptual stage, and is thus devoid of industrial, pilot-scale and lab-scale demonstration, design and performance details are yet to be investigated and developed. Some of the key considerations to address include: determining the number of tubes required for adequate cooling, quantifying the risk of catalyst and tube overheating when subjected to gasifier operating conditions, and assessing the ability of the device to reject potential shifts and upsets in gasifier operation. A suitable base case design and control structure is developed for both co-current and counter-current flow configurations, where the benefits and drawbacks of each configuration in the context of steady-state and dynamic operation will be explored and discussed.

4.1   Base Case Design

A brief study into the development of a base case design is necessary. To facilitate this, there exists abundant literature and guidelines concerning the typical design of SMR systems. However, for gasifiers (specifically the GE-Texaco version), there is a lack of accessible information regarding design specifications and operating conditions, as this is largely considered proprietary. The integration of these two technologies causes design choice conflicts to arise that do not exist with each independent system; these choices are simultaneously compared to determine a feasible design that satisfies the most critical constraints of both systems. Of paramount concern is that the design is safe, with a nominal operation established well within material and process limits. Secondly, the design should satisfy performance criteria, such as efficient use of the natural gas (NG) and steam feedstocks.

The primary safety considerations are the maximum tube wall temperatures and the pressure drop across the tube. As a result of the maturation of SMR and catalyst technology, the primary limitation to reformer performance (CH_4 conversion) is the maximum allowable tube wall temperatures (Steynberg and Dry, 2004), a constraint set by the chosen material of tube construction, rather than by the process itself. High alloy steel is the material of choice for conventional SMR furnaces, with modern variants capable of withstanding tube temperatures up to 1400 K (Schmidt & Clemens Inc., 2010). However, under pressurized conditions, operating at elevated tube temperatures can severely reduce the expected tube life (Hawkins, 2013). Lowering the inlet pressure can also drive CH_4 conversion further, but pressure drop can become quite significant across the length of the catalyst bed (Hawkins, 2013). Typical pressure drop across the tube in conventional SMR systems is between 5.1 and 5.7 bar (Pedernera et al., 2003).

The primary performance objectives for the RSC/SMR system are: conversion of CH_4 within the SMR tubes, and coal-derived syngas temperature at the RSC exit. Within the SMR literature, there exist many different cases of CH_4 conversion, from as low as 48% (Pedernera et al., 2003) to as high as 90% (Singh and Saraf, 1979). An industrial guide-

line provided by Hawkins (2013) uses the definition of CH_4 slip to characterize desired conversion. CH_4 slip, henceforth denoted as y_{CH_4}, refers to the mol % of CH_4 in the reformer exit gas on a dry basis. Hawkins (2013) uses 3.5% y_{CH_4} in their base case design, which translates to a CH_4 conversion of approximately 85%, which will be used as the target conversion in this study.

Of secondary importance is the coal-derived syngas temperature at the RSC exit. While not as strict a safety consideration as tube wall temperature, current gasifier RSCs are designed around an expected coal-derived syngas exit temperature of around 1,033 K (Woods et al., 2007). The chosen RSC/SMR design should provide this level of cooling, in order to mimic the current industrial RSC performance as closely as possible. Robinson and Luyben (2008) mention that tight control over coal-derived syngas temperatures may not be overly important, as there is a quench system immediately downstream that provides additional cooling to the RSC exit gas. Bockelie et al. (2003) estimate the cooling rate of the quench section at around 27,000 K s^{-1}, which far surpasses typical RSC cooling rates of 100 to 550 K s^{-1}. As such, variations in the RSC coal-derived syngas exit temperature can be easily handled by the quench system, and should not be detrimental to the overall system. It does, however, represent a loss in exergy, as the RSC tubes are not able to extract as much useful heat in this case.

To summarize, the RSC/SMR device base case must obtain a 3.5% y_{CH_4} (85% conversion) within the tubes, subject to the following constraints, listed in order of decreasing importance:

1) Max Tube wall temperature (< 1,350 K)

2) Pressure Drop (< 5.7 bar)

3) Coal-derived syngas temperature (~1,033 K)

Table 4.1 and Table 4.2 provide a summary of the design parameters considered in the literature for SMR systems, where the table headings correspond to the eight decision variables adopted in this work to obtain a feasible design for the radiant tubes. The base case

designs explored for the RSC/SMR hybrid system (as discussed in Sections 4.1.1 and 4.1.2) utilized the parameter ranges in Table 4.1 and Table 4.2 as general bounds for the decision variables.

Table 4.1: Typical SMR tube design parameters found in literature.

Source	Tube I.D. [m]	Tube Thickness [m]	Number of tubes	Length [m]
De Deken J et al., 1982	0.102	0.015	-	12
Xu & Froment, 1989	0.102	0.015	-	12
Pedernera et al., 2003	0.084 – 0.155	0.008 – 0.013	-	-
Hawkins, 2013	0.095	-	352	12.98
Pantoleontos et al., 2012	0.102	0.015	169	12
Steynberg & Dry, 2004	0.080 – 0.160	0.008 – 0.020	< 1000	10 - 14
Elnashaie, 1994	0.098	0.008	896	14.5

Table 4.2: Typical SMR process gas inlet conditions found in literature.

Source	P_{inlet} [bar]	T_{inlet} [K]	F_{inlet} [kmol h^{-1}]	S/C Ratio
De Deken J et al., 1982	28.1	793	24.08	3.33
Xu & Froment, 1989	29.0	793	24.33	3.36
Pedernera et al., 2003	38.7	823	44.06	3.20
Hawkins, 2013	-	773	-	-
Pantoleontos et al., 2012	25.7	793	24.29	3.36
Steynberg & Dry, 2004	15.0 – 40.0	-	-	-
Elnashaie, 1994	29.8	760	19.55	3.56

In contrast to SMR systems, Table 4.3 illustrates the relative lack of available design specifications for the RSC. Robinson and Luyben (2008) and Monaghan and Ghoniem (2012c) provide the main work developed around dynamic simulation of the GE-Texaco gasifier, that also consider the modeling of the RSC. However, both of these works make divergent assumptions regarding the radiant tube design and RSC size; thus, the parameters provided can be treated as speculative at best. However, as seen in Table 4.3, the operating conditions in both works are in close agreement to the published values provided in the NETL report (Woods et al., 2007).

Table 4.3: Comparison of reported gasifier RSC design and operating conditions found in literature.

	(Robinson and Luyben, 2008)	(Monaghan and Ghoniem, 2012c)	NETL Report (Woods et al., 2007)
Tube I.D. [m]	0.038	0.05	-
Tube Thickness [m]	0.003	0.01	-
# Tubes	2828	-	-
Length [m]	30	40	-
Pressure [bar]	55.1	56	55
RSC inlet temp [K]	1644	1589	1589
Syngas flow rate [kg h⁻¹]	237428	255325	249618
RSC I.D. [m]	4.572	2.74	-

Typical tube lengths for conventional SMRs (Table 4.1) fall well short of the tube lengths of the RSC (Table 4.3). The RSC/SMR design choice must hence be a compromise between these two. SMR tubes, due to the catalyst loading, are generally not able to support the excessive pressure drop that would arise if the typical RSC tube lengths are used. The gasifier RSC inner tube diameters (Table 4.3) are also smaller than the range of allowable SMR tube diameters (Table 4.1), and would be too narrow to uniformly fill with the SMR catalyst. The number of tubes chosen must be able to fit within the RSC internal cross-sectional area (A_{CS}), leaving free space in the center along the RSC axis, to allow slag to freely flow through from the gasifier. Luyben's tube estimate results in 34.9% of the cross-sectional area being occupied by tubes (Robinson and Luyben, 2008); the design in this work will consider this as a maximum tube occupancy.

The gasifier RSC shell size and operating conditions utilized in this work are derived from Table 4.3 and are listed in Table 4.4. The chosen RSC/SMR base case design will have to provide cooling duty within this environment.

Table 4.4: Nominal gasifier operating conditions for the RSC/SMR hybrid system.

D_{RSC} [m]	M_S^{in} [kg h⁻¹]	T_S^{in} [K]	P_S^{in} [bar]
4.572	237428	1589	55.1

4.1.1   Counter-Current Base Case Design

Using the gasifier RSC conditions of Table 4.4, a number of cases were simulated by varying the eight SMR tube decision variables within ranges specified by Table 4.1 and Table 4.2. The effects of each decision variable on the conversion (CH_4 slip) and maximum tube wall temperature are illustrated in Figure 4.1 and Figure 4.2. For all decision variables, with the exception of tube inlet pressure (P_T^{in}), cases with higher conversion are accompanied by a subsequent increase in maximum tube temperature.
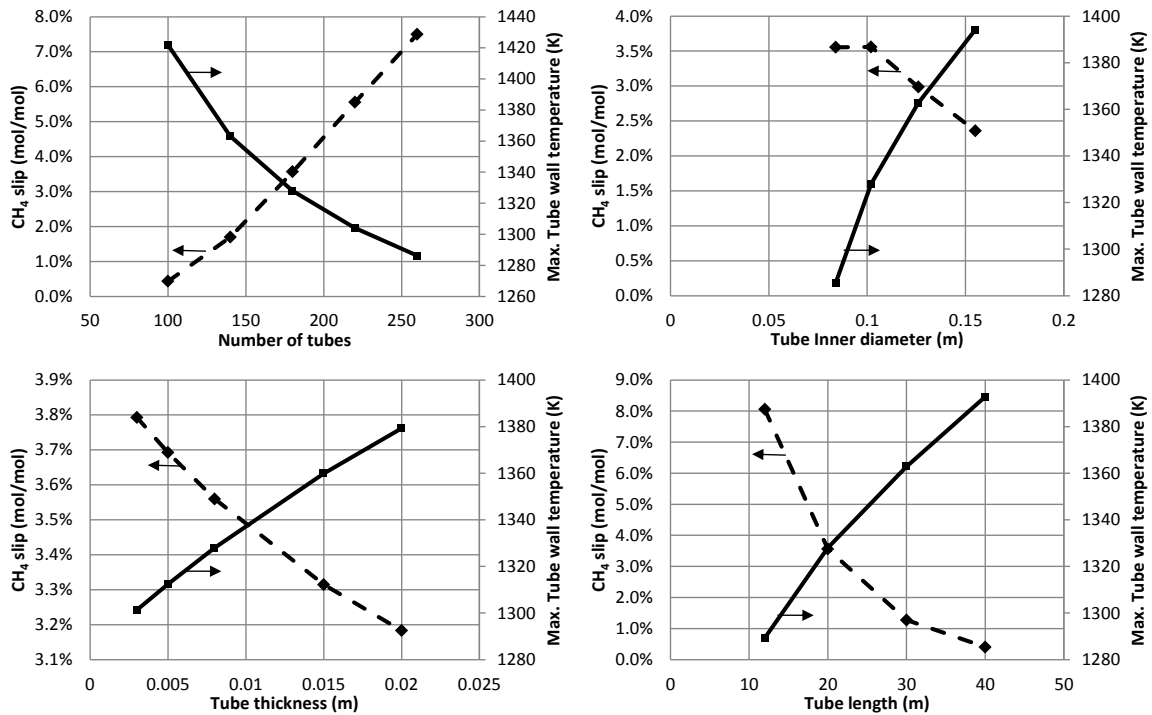
Figure 4.1: Counter-current design - Sensitivities of CH_4 conversion (CH_4 slip) and maximum tube wall temperature to the tube design decision variables: number of tubes, inner tube diameter, tube thickness and tube length.
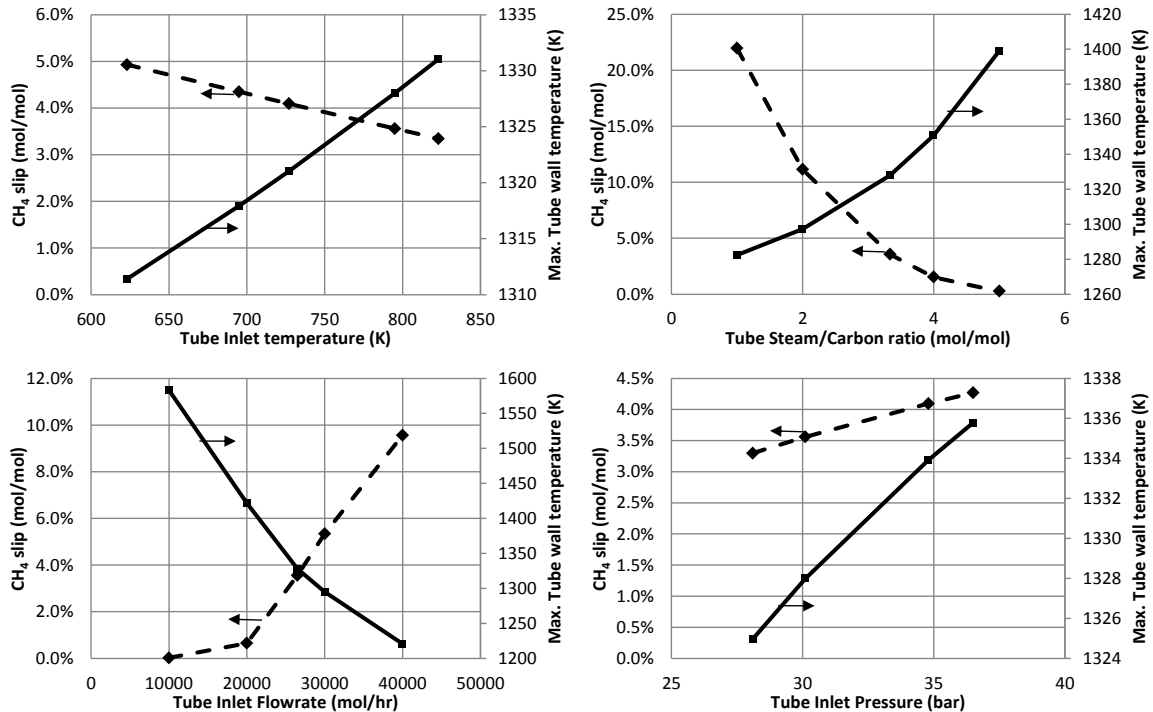
Figure 4.2: Counter-current design - Sensitivities of CH$_4$ conversion (CH$_4$ slip) and maximum tube wall temperature to the tube gas inlet condition variables: temperature, pressure, S/C ratio and flow rate.

In general, due to the nature of counter-current flow, the coal-derived syngas exiting the RSC was always sufficiently cooled, provided that the maximum tube wall temperature constraint was satisfied. Figure 4.3 illustrates the maximum tube wall temperature and CH$_4$ conversions obtained for a variety of investigated base case designs. It is desired to have nominal operation located in the upper left corner of Figure 4.3, where CH$_4$ conversion is high and the maximum tube wall temperature is relatively low. While the absolute maximum temperature is 1,400 K (Schmidt & Clemens Inc., 2010), a safety margin of 50 K was employed to allow for deviations during transient operation and disturbance rejection. It was found that all base cases with adequately low tube wall temperature (< 1350 K) and high conversion (~90% or greater) suffer from an excessively high pressure drop (> 5.7 bar), denoted with an 'X' on Figure 4.3.
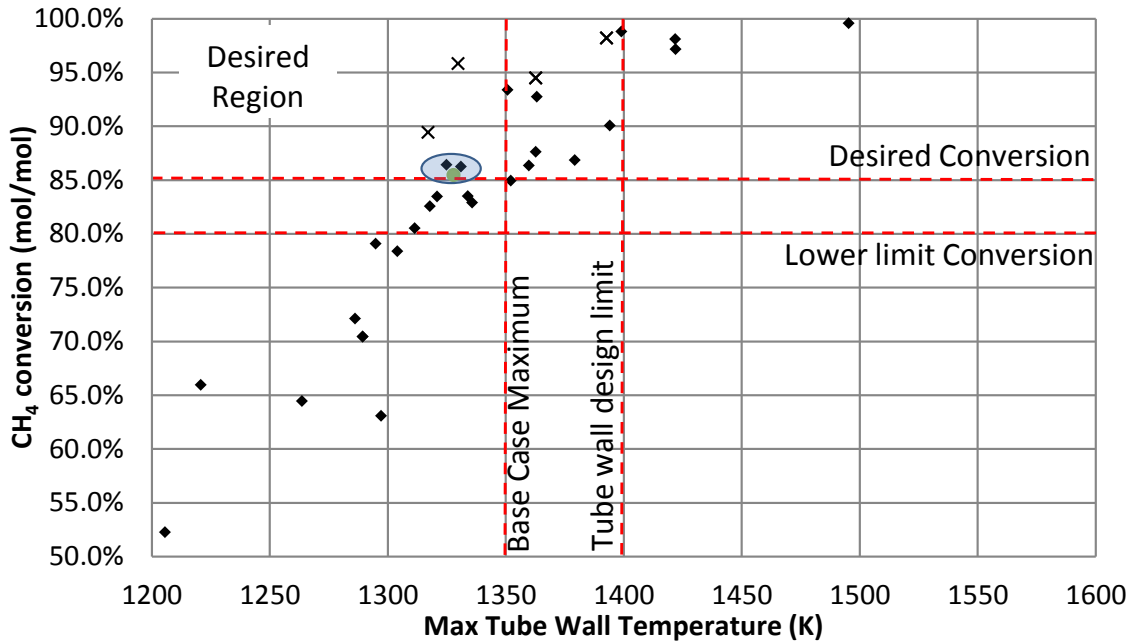
Figure 4.3: Scatter plot of CH$_4$ conversion vs. Maximum Tube Wall temperature for a variety of counter-current cases. X's denote infeasible designs due to excessive pressure drop. The green circle highlights the base case selected.

The blue ellipse on the map encases the designs that meet the CH$_4$ conversion criteria in addition to obeying all other constraints of interest. The green circle corresponds to the base case that was chosen, and the summary of decision variables for this design is provided in Table 4.5.

Table 4.5: Base case configurations for counter-current and co-current flow systems.

	Counter-Current	Co-current
$R_{W,I}$ [m]	0.102	0.102
X_W [m]	0.008	0.008
N_t	180	140
L [m]	20	20
P_T^{in} [bar]	30.1	30.1
T_T^{in} [K]	795	795
F_{SMR} [kmol/hr]	26.5	21.5
$R_{S/C}$	3.336	3.336

The axial temperature, pressure and composition profiles for this design are shown in Figure 4.4, Figure 4.5 and Figure 4.6 respectively. The average refractory outer wall temperature for this design is 552 K, which is close to the reported average refractory temperature of 541 K from the Polk Power Station Gasifier (McDaniel and Hornick, 2002) . An interesting observation is that the tube gas temperature profile initially decreases over the first two metres upon entering the RSC Length (Figure 4.4); this decrease results from the strongly endothermic reaction in the tubes, whereby the heat flux at that location is insufficient to simultaneously increase the gas temperature. The heat removed from the coal-derived syngas is approximately 77MW, and the coal-derived syngas temperature at the RSC exit is 1,013 K, which closely matches the NETL result for the conventional gasifier RSC (Woods et al., 2007).
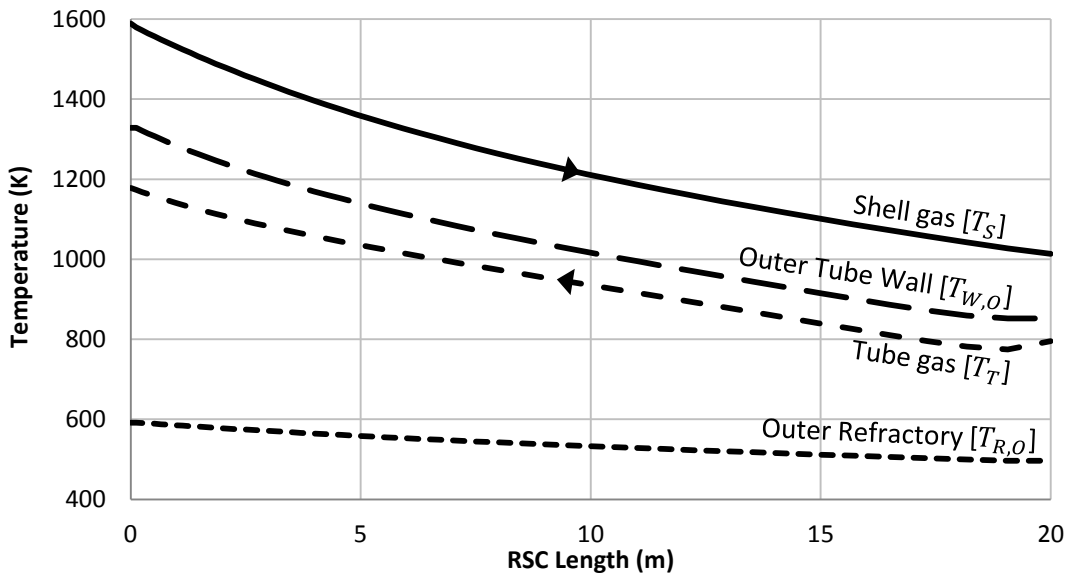
Figure 4.4: Counter-current base case axial temperature profiles. Arrows on the line indicate direction of gas flow.
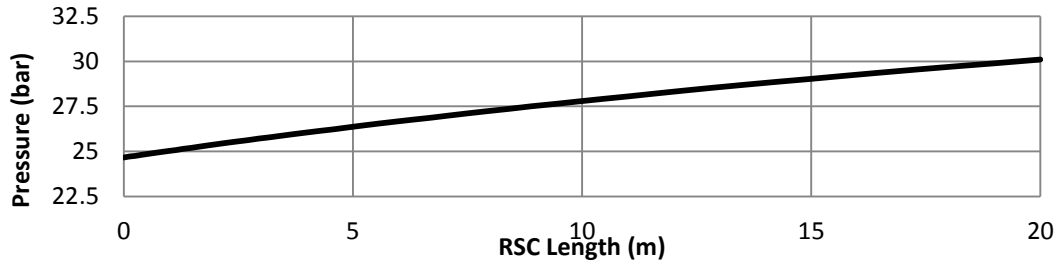
Figure 4.5: Counter-current base case axial pressure profile.
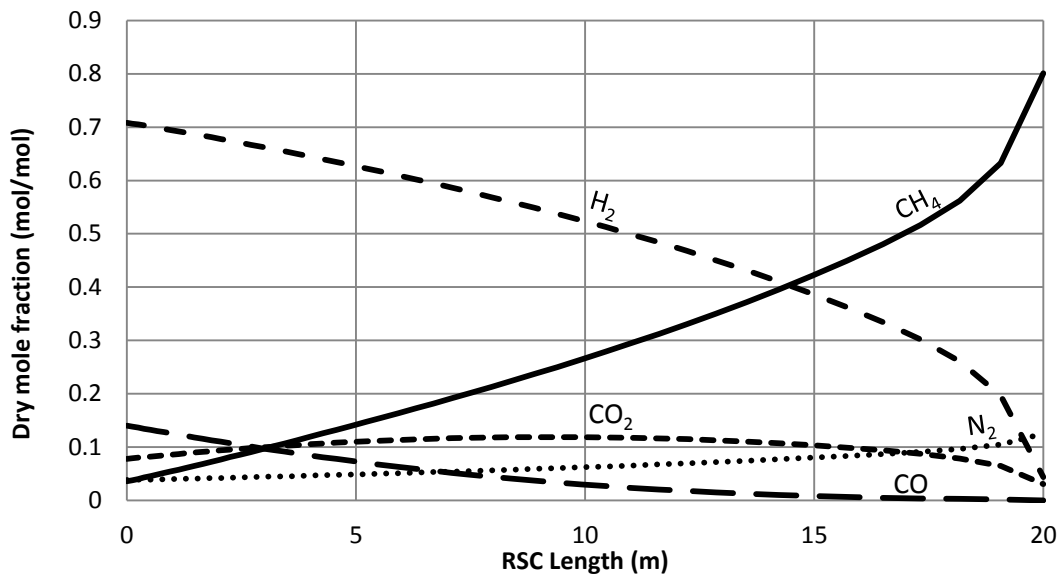
Figure 4.6: Counter-current base case axial dry mole fraction profiles.

4.1.2   Co-current Base Case Design

In using the exact same base case design from the counter-current analysis for the co-current configuration, the CH_4 conversion attained was significantly reduced. The co-current configuration inherently cannot provide as much cooling duty to the coal-derived syngas, as reducing the coal-derived syngas temperature to levels attained in the counter-current design will result in an unacceptably low CH_4 conversion, due to markedly lower average tube wall temperatures. For the co-current system, the main temperature to consider is not the maximum tube wall temperature, but rather the coal-derived syngas exit temperature. These differences can be seen in Figure 4.7, where all of the investigated co-

current base case design cases result in maximum tube wall temperatures well below the design limit. It is still desirable to choose a base case with sufficient conversion and a temperature as far to the left of Figure 4.7 as possible. This is because the maximum tube temperatures correlate strongly with coal-derived syngas exit temperature, and higher tube temperatures imply insufficient shell gas cooling. In Figure 4.7, designs marked by an 'X' denote pressure drop greater than the maximum desired for a base case. The chosen base case design parameters correspond to the green circle in Figure 4.7 and are listed in Table 4.5.

Figure 4.7: Scatter plot of CH₄ conversion vs. Maximum Tube Wall temperature for a variety of co-current cases. X's denote infeasible designs due to excessive pressure drop. The green circle highlights the base case selected.

The axial profiles for the co-current base case are shown in Figure 4.8, Figure 4.9 and Figure 4.10. As a result of less efficient heat utilization, the coal-derived syngas temperature at the RSC exit is significantly higher than the counter-current design (Figure 4.4), by 193 K. It is anticipated that the quench system immediately downstream can tolerate this elevated shell gas temperature due to its large cooling capacity. The co-current base case provides a cooling duty of 51 MW, which is 33% less than the counter-current case. Outer

refractory temperatures are similar to those seen in the counter-current case. However, the maximum temperature of the tube wall is 1,214 K, which is 114 K lower than the maximum temperature in the counter-current case. From a steady-state perspective, although the thermal efficiency and throughput of the co-current design is lower, the overall decreased tube wall temperatures make it an inherently safer design.
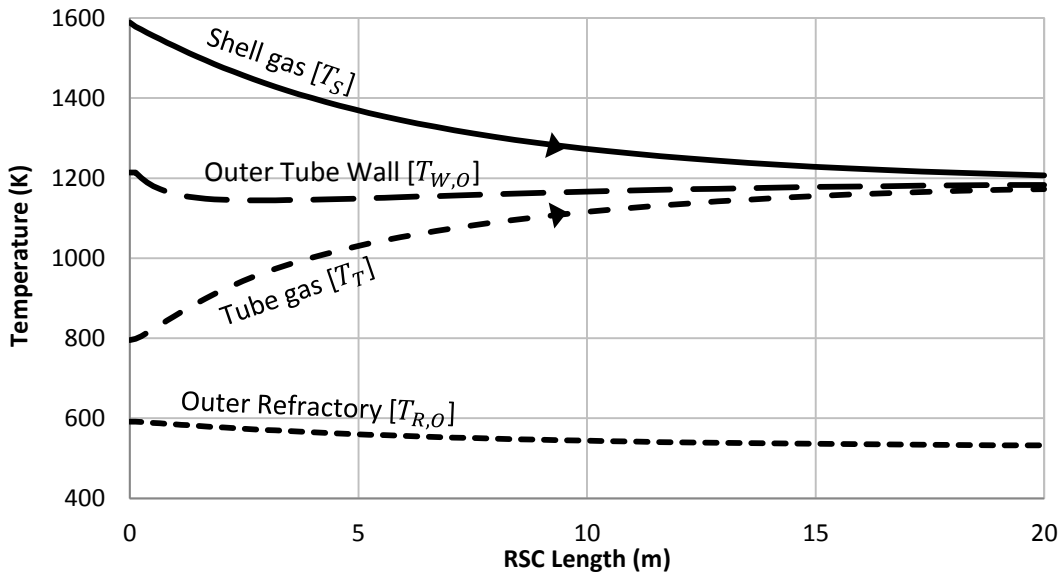
Figure 4.8: Co-current base case axial temperature profiles. Arrows on the line indicate direction of gas flow.
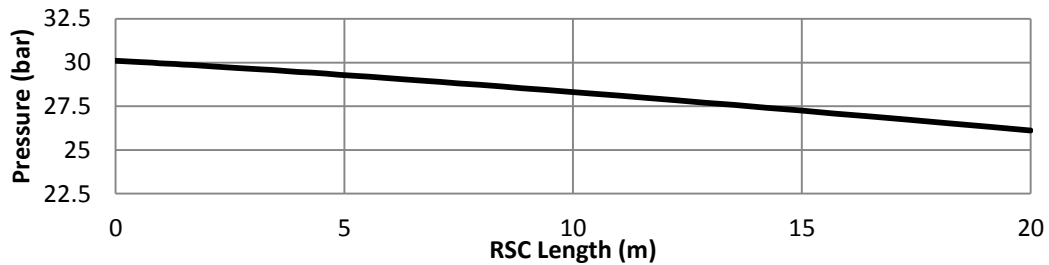
Figure 4.9: Co-current base case axial pressure profile.
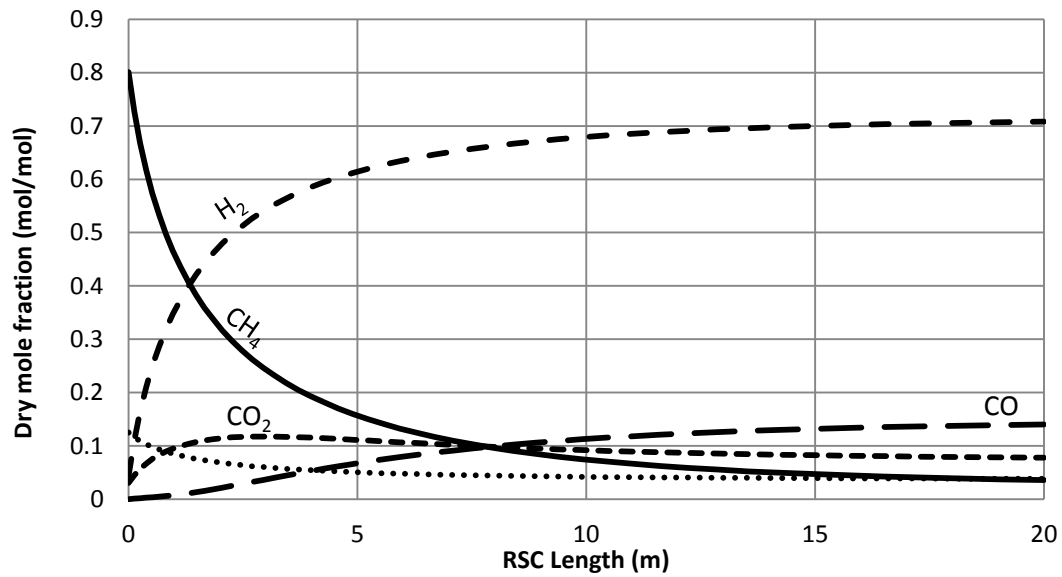
Figure 4.10: Co-current base case axial dry mole fraction profiles.

4.2   Control Development and Analysis (Counter-current)

The control structure to be implemented for this system must be able to respond to transient conditions on the coal-derived syngas side. It is unrealistic to demand a change in the operation of the gasifier in order to satisfy the performance criteria of the SMR/RSC system. Rather, all aspects of the gasifier operation and resulting coal-derived syngas properties are to be regarded as disturbances (whether measured or unmeasured). This represents the fundamental difference between the control of this RSC/SMR hybrid system, versus the control of a conventional SMR furnace.

Typically, with a conventional SMR furnace, the operator has control over the heat duty provided to the reformer tubes. A large factor in the performance of the conventional SMR, in terms of attaining acceptable CH_4 conversion, is the ability to adjust the rate of fuel gas flow to the furnace. However, in the case of the RSC/SMR system, heat duty that is available to the reformer tubes is a disturbance, rather than a manipulated variable (MV). As such, when a higher conversion of CH_4 is required, it is not possible to adjust the flow rate of coal-derived syngas, or the gasifier temperature. Rather, the rate at which NG and steam are fed to the tubes must be adjusted as MVs, in response to the level of heat duty that is available. This is contrary to stand-alone SMR systems that consider the NG feed as a disturbance variable (DV).

The MVs and CVs considered for both the counter-current and the co-current RSC/SMR system are the same, as listed in Table 4.6.

Table 4.6: Controlled and Manipulated variables used for PI control design (both counter-current and co-current).

CV$_1$	CV$_2$	MV$_1$	MV$_2$
T_{gas}	y_{CH_4}	F_{SMR}	$R_{S/C}$

4.2.1   Open Loop Step Test and Relative Gain Array:

In this configuration, the MVs are total flow rate into the SMR (F_{SMR}), and steam-to-carbon ratio ($R_{S/C}$). These MVs simultaneously determine the flow rate of NG (F_{NG}) and steam (F_{STM}) to the tubes via equations (3.20) and (3.21).

Open loop step testing was performed on each MV separately. First, the steady state corresponding to the base case design was attained. F_{SMR} was then subjected to a +1000 mol hr^{-1} step after 100 seconds of steady-state operation. $R_{S/C}$ remained unchanged for this scenario. The dynamic response of both CVs was tracked until the system reached a new steady state. The simulation was rerun with providing a +10% step in $R_{S/C}$, while maintaining fixed F_{SMR}. Note that in this scenario, both F_{NG} and F_{STM} become adjusted according to the new $R_{S/C}$, but the summation of the flows (F_{SMR}) remains fixed. The results of the open loop step test can be seen in Figure 4.11.
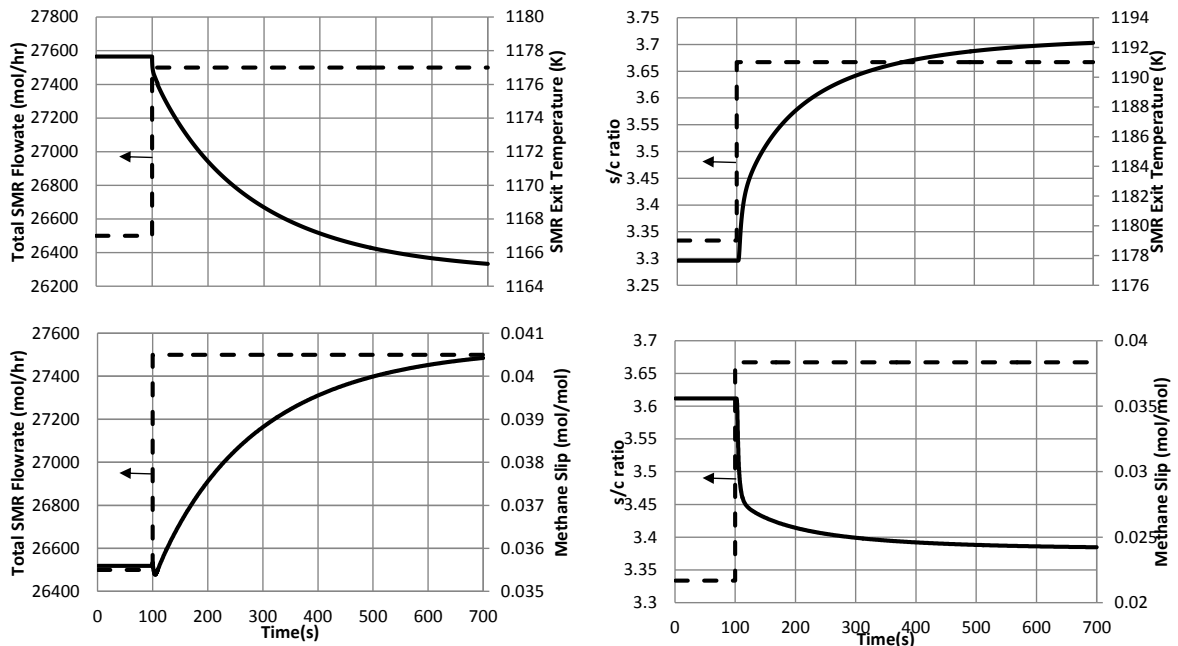
Figure 4.11: Open Loop response data for the counter-current configuration.

Using the graphical result (Figure 4.11), the process reaction curve method (Marlin, 2000) was employed to obtain the key process parameters to describe the response dynamics.

The temperature dynamics closely resemble a typical first-order response for both MV step inputs. The y_{CH_4} response is first-order with an initial inverse trajectory following the step change in F_{SMR}.

The Relative Gain Array (RGA) method was employed using the steady state process gains, to assess the interaction between the loops, and select an appropriate pairing (Marlin, 2000):

$$\lambda_{11} = \frac{1}{1 - \frac{K_{12}K_{21}}{K_{11}K_{22}}} \tag{4.1}$$

$$RGA = \begin{bmatrix} \lambda_{11} & 1 - \lambda_{11} \\ 1 - \lambda_{11} & \lambda_{11} \end{bmatrix} \rightarrow \begin{bmatrix} 2.02 & -1.02 \\ -1.02 & 2.02 \end{bmatrix} \tag{4.2}$$

The RGA analysis suggested the following pairing: F_{SMR} should be used to control T_{gas}, and $R_{S/C}$ should be used to control y_{CH_4}. The RGA parameter $\lambda_{11} > 1$, implying that for multi-loop control, each loop may need to be more aggressively tuned to combat process interaction, relative to single-input-single-output control. Figure 4.12 illustrates the control design chosen for the counter-current case based on this analysis.
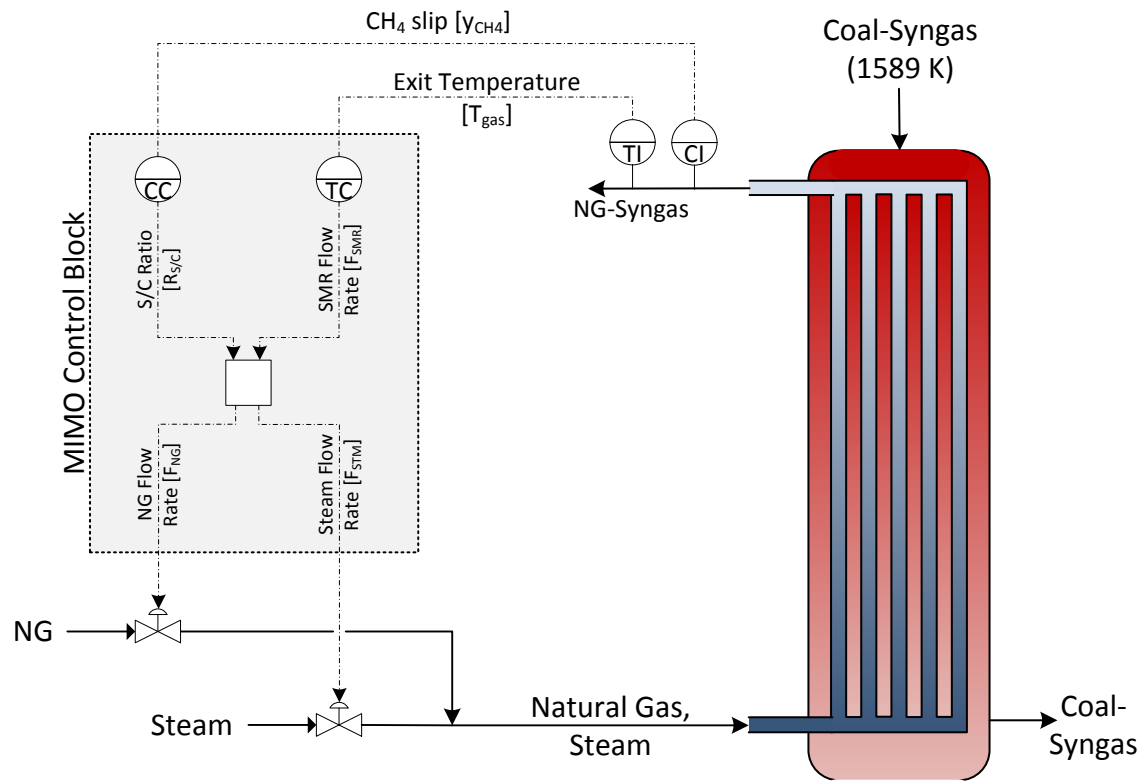
Figure 4.12: Control design illustration for counter-current case.

4.2.2   Control Performance Comparison of Tuning Rules

Three methods were investigated to obtain initial values for the controller tunings, chosen due to their historical prevalence in the industry as a simple but effective means of obtaining desired PI control performance. Table 4.8 summarizes the calculated tuning parameters from the different rules of Table 4.7. The Z-N and C-C tuning rules yield very aggressive control which is beneficial for disturbance rejection, but may lead to overly demanding moves in the MVs for set point (SP) changes. As seen in Table 4.8, the T_{gas} controller gains (K_C) computed using the Z-N and C-C rules are extremely large; this is a result of the process transfer function having almost no dead time, in conjunction with a long time constant. In contrast, IMC tuning rules result in slower, less aggressive and less oscillatory control. To obtain a more conservative and robust control response in the face of loop interaction, τ_C was chosen to be equal to τ_p as per the recommendation by Seborg et al. (2010).

Table 4.7: Equations used to determine control parameters from process data.

	K_C	τ_I	τ_C
Ziegler-Nichols (Z-N) **(Chau, 2002)**	$\dfrac{0.9\tau_p}{K_p t_d}$	$3.3 t_d$	-
Cohen-Coon (C-C) **(Chau, 2002)**	$\dfrac{1}{K_p}\left(\dfrac{0.9\tau_p}{t_d}+\dfrac{1}{12}\right)$	$t_d\dfrac{30+3(\frac{t_d}{\tau})}{9+20(\frac{t_d}{\tau})}$	-
IMC (Seborg et al., 2010)	$\dfrac{\tau_p}{K_p(\tau_c+t_d)}$	τ_p	$\tau_p \geq \tau_C \geq t_d$

Table 4.8: Tuning Parameters for counter-current control.

	$F_{SMR} \rightarrow T_{gas}$			$R_{S/C} \rightarrow y_{CH_4}$		
	K_C	τ_I	τ_C	K_C	τ_I	τ_C
Z-N	-12158.2	3.3	-	-83.2	9.9	-
C-C	-12165.0	3.3	-	-85.6	6.0	-
IMC	-264.9	166.5	166.5	-22.2	9.5	9.5

Disturbance Rejection

To compare the different tunings, the dynamic performance of the system was tested following a -10% step disturbance in the gasifier syngas flow rate (M_S^{in}) (Figure 4.13). C-C tuning parameters are not illustrated here due to their closeness to the Z-N values. The Z-N tuned controllers were much more effective in maintaining the CVs at set point for this scenario, with slightly more aggressive movement in F_{SMR}. Relative to IMC, the Z-N deviation for T_{gas} from set point after the disturbance is hardly noticeable. The IMC response is still considered satisfactory, returning the T_{gas} and y_{CH_4} to set point within 15 minutes.
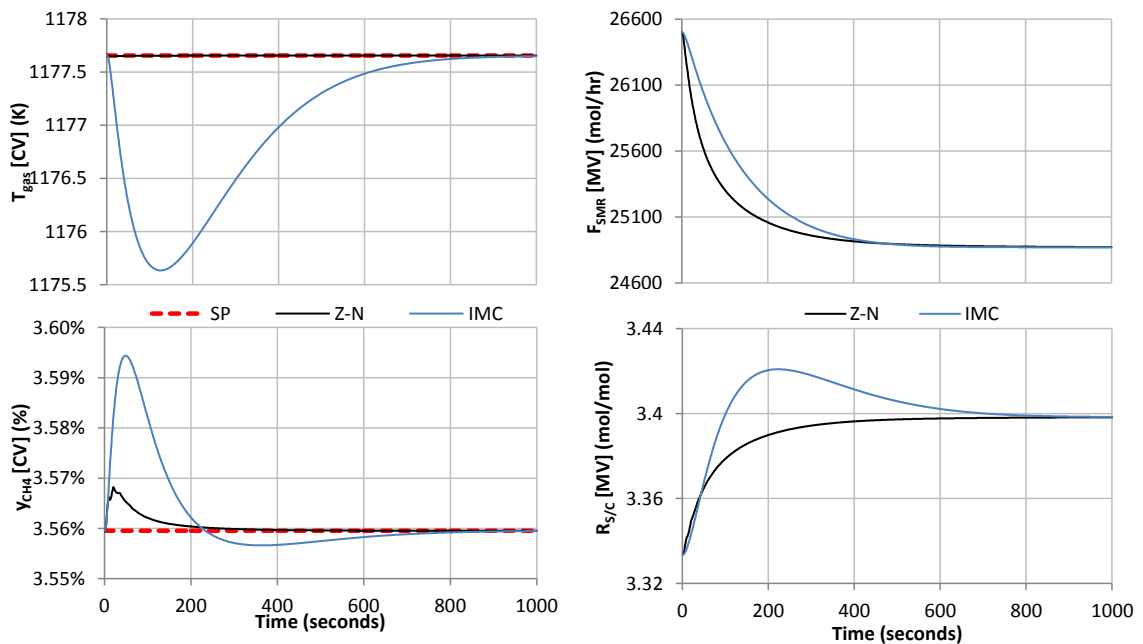
Figure 4.13: Comparison of controller tunings for disturbance rejection (counter-current).

Set point changes

Depending on the demand for syngas, or the operation of the gasifier, it may be necessary to adjust the set points of the CVs. This is particularly true for instances where it is desired to move the RSC/SMR system from one operating point to another, as may be the case in the context of a flexible polygeneration plant. The Z-N and IMC tunings were

tested against a set point change in both the temperature and the composition controller (Figure 4.14). At time zero, a -10 K ramp in the T_{gas} set point was implemented over a period of sixty seconds, to 1,167.6 K, and kept at that set point for the remainder of the simulation. At 500 seconds, a +1.0 percentage point step in the y_{CH_4} set point was implemented, and maintained for the remainder of the simulation. The IMC tuned controllers were easily able to drive the CVs to the new set point, while the Z-N tuned controllers were unable to handle the sudden change in y_{CH_4} set point. While a fast response is desired, it should never be at the expense of the stability of the system. It is expected that with the introduction of measurement noise, the MV movement of the Z-N tuned controllers will become grossly exaggerated, leading to unwanted instability. As a result, the IMC tuning parameters were chosen for subsequent analysis. The oscillatory Z-N response was suspected of being caused by numerical error resulting from the solver parameters used. The absolute and relative error tolerance were adjusted from 1×10^{-5} (the default) to 1×10^{-8}, with no observed change in the oscillatory result. As such, the Z-N response was deemed to not be the result of numerical error.
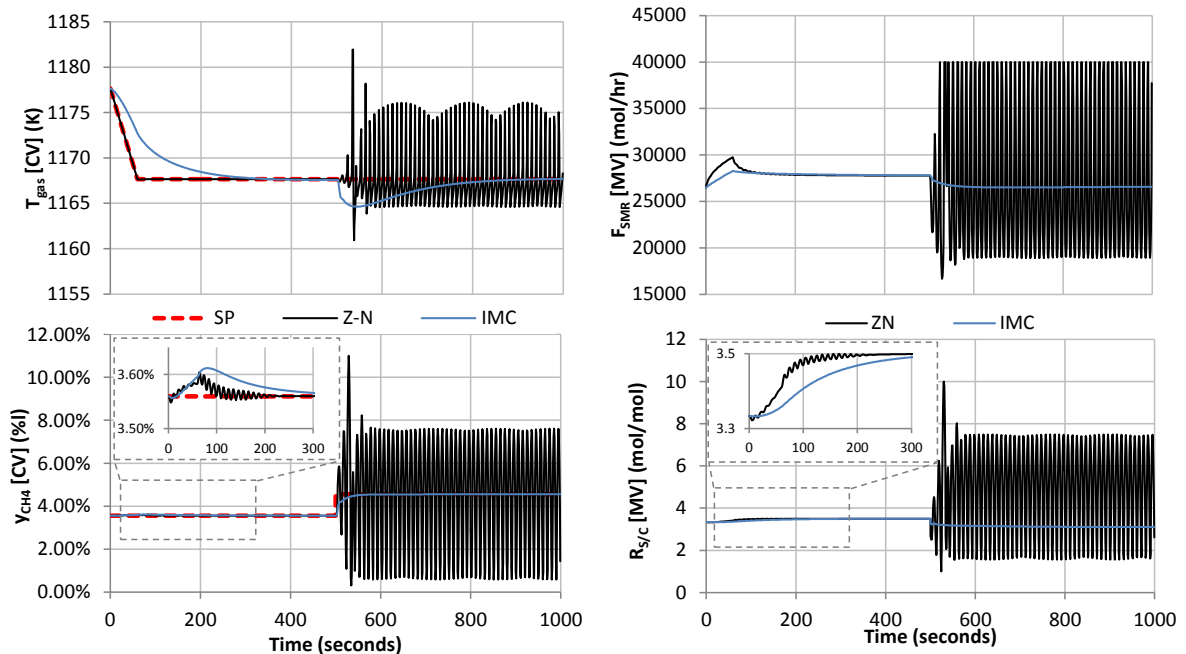
Figure 4.14: Comparison of controller tunings for set point changes (counter-current).

4.2.3   Optimal Tuning Parameters (Set Point Changes)

While the IMC tuning parameters provide a good starting point, control performance can become greatly improved by fine tuning. To obtain control that performs well for both disturbance rejection and set point changes, the dynamic optimization tool in `gPROMS` was used. For the counter-current case, the objective function to be minimized was specified as:

$$\min_{K_{c,j}, \tau_{I,j}} \left[\mu \times IAE_{y_{CH_4}}(t) + (1 - \mu) \times IAE_{T_{gas}}(t) \right],$$
(4.3)

subject to:

$$K_{c,min} \leq K_{c,j} \leq K_{c,max} \quad , \quad \forall\, j = 1,2$$
(4.4)

$$\tau_{I,min} \leq \tau_{I,j} \leq \tau_{I,max} \quad , \quad \forall\, j = 1,2$$
(4.5)

$$MV_{min} \leq MV_j(t) \leq MV_{max} \quad , \quad \forall\, j = 1,2.$$
(4.6)

Integral Absolute Error (IAE) is commonly used for evaluating the performance of a controller, defined as:

$$IAE(t) = \int_0^t \frac{|CV(t) - SP(t)|}{SP(t)} \, dt.$$
(4.7)

The μ term in equation (4.3) represents a relative weighting factor, between 0 and 1 (i.e., $\mu \in [0,1]$), with 0.5 representing equal weight being placed on both controller objectives. Tuning parameters K_C and τ_I are fixed for the optimization window. The values for the bounds in equations (4.4) to (4.6) are listed in Table 4.9. The upper bound for F_{SMR} was set at 40000 mol/hr to prevent excessive pressure drop across the tubes, while the lower bound for $R_{S/C}$ was set at 1, as carbon deposition onto the catalyst becomes an issue in this regime and promotes catalyst deactivation (Hawkins, 2013).

Table 4.9: Bounds used for optimization (counter-current and co-current).

	$K_{C,T_{gas}}$	$\tau_{I,T_{gas}}$	$K_{C,y_{CH_4}}$	$\tau_{I,y_{CH_4}}$	F_{SMR}	$R_{S/C}$
min	-15000	1	-1000	1	10	1
max	-1	1000	-1	1000	40000	10

The dynamic optimization run initially starts at steady-state, with T_{gas} and y_{CH_4} at their respective set points. At time zero, a -10 K ramp in the T_{gas} set point is implemented over a period of sixty seconds, and maintained at the new set point for the remainder of the 1,000 second run. At time 500 seconds, a +1.0 percentage point step in the y_{CH_4} set point is implemented, and maintained at that new set point for the remainder of the 1000 second run. The IMC tuning parameters were used as an initial guess for the optimization.

A Pareto front for the counter-current case was established by re-running the optimization using different values of μ, as shown in Figure 4.15. With μ chosen between 0.25 and 0.75, the IAE for both the temperature and composition loops are improved over the IMC tuning parameters, with most of the performance gain in the temperature control. With μ between 0.75 and 0.98, the optimal tuning yields a much improved IAE in the temperature loop, but slightly worsened IAE in the composition loop, relative to the IMC tuning. Choosing μ outside of the above mentioned ranges yields highly unsatisfactory control performance for both CVs. For the case studies discussed herein, μ was chosen be 0.5 to balance the IAEs between each of the two controllers; the corresponding tuning parameters are listed in Table 4.10. Note that $\tau_{I,T_{gas}}$ in Table 4.10 is at the minimum bound. Upon relaxing the bound (to $\tau_{I,min} = 0.1$ seconds), $\tau_{I,T_{gas}}$ settled to a new optimal value of 0.997 seconds. This miniscule difference from the previous value of $\tau_{I,T_{gas}}$ offered negligible improvement in the objective function of equation (4.3).

Table 4.10: Comparison of IMC vs Optimal PI tuning parameters for counter-current control.

	T_{gas}		y_{CH_4}	
	K_C	τ_I	K_C	τ_I
IMC	-264.9	105.5	-26.9	9.5
Optimal ($\mu = 0.5$)	-136.4	1.0	-28.8	3.7
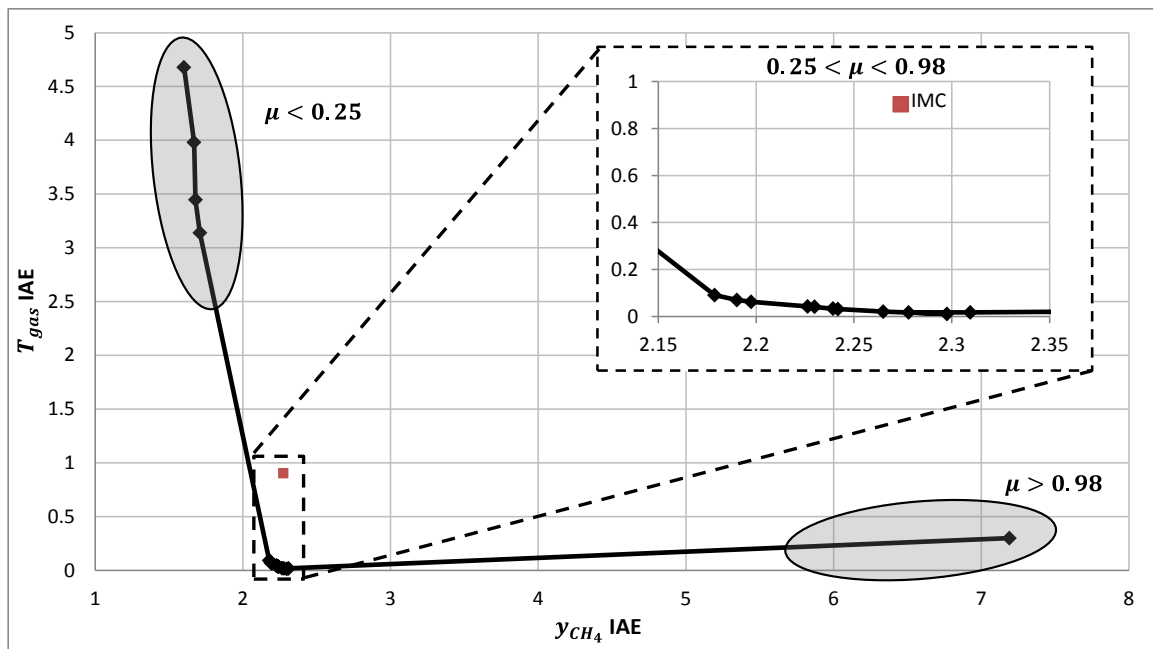
Figure 4.15: Pareto front for optimal PI tuning parameters for the counter-current case. IMC result is shown as the red square for comparison.

4.2.4   Control Case Studies

With a PI control structure now in place, the RSC/SMR system was tested against cases of set point changes and disturbance rejection. The gasifier dynamics are known to be quite fast, on the order of several minutes (Robinson and Luyben, 2008). The conventional RSC system had one primary objective, which was to provide cooling to the gasifier syngas. On the other hand, the hybrid RSC/SMR system has two primary objectives: provide cooling to the gasifier syngas, and maintain CH_4 conversion within the SMR tubes.

The following scenarios were developed to test the control performance and demonstrate potential operation of the RSC/SMR device:

Case 0a: +1 percentage point step in y_{CH_4} set point

This set point change in y_{CH_4} may occur when a reduction in NG-derived syngas production rate is desired, due to decreased demand by the liquid fuels section downstream.

Case 0b: -10 K ramp in T_{gas} set point

This ramp in T_{gas} set point may occur when additional cooling duty to the coal-derived syngas is required, or if additional NG-derived syngas throughput is demanded by downstream processes. The -10 K ramp in T_{gas} occurs over a sixty second period, following which the new set point is maintained for the remainder of the simulation.

Case 1a and 1b: Shell gas temperature disturbance (T_S^{in})

The exact temperature of the gasifier syngas is a complex product of the gasification conditions and coal feedstock properties and feed flow rates, and Bockelie et al. (2004) mention that the gasifier can have an exit temperature between 1,422 K and 1,644 K. As a reasonable estimate of the temperature variation in the coal-derived syngas gasifier exit temperature (prior to entering the RSC), case 1a implements a 50 K step increase in T_S^{in}, while case 1b implements a 50 K step reduction in T_S^{in}.

Case 2: Change in the gasifier feed ratios – affects shell gas composition (T_S^{in}, y_S^{in})

While the gasifier (POX section) is not modeled in this study, Bockelie et al. (2003) provide estimates of the impact of gasifier H_2O/coal and O_2/coal feed ratios on coal-derived syngas properties. While a shift in the gasifier feed ratios does not have a large effect on the coal-derived syngas composition, the temperatures vary significantly. This case implements a step change in the H_2O/Coal ratio from 0.6 to 0.5, which corresponds to the shift in shell gas inlet conditions (T_S^{in}, y_S^{in}) specified in Table 4.11.

Table 4.11: Effect of changing gasifier feed conditions on RSC shell gas inlet conditions for Case 2 (derived from (Bockelie et al., 2003)).

Gasifier Feed ratios		Corresponding shell gas inlet conditions				
H_2O/Coal	O_2/Coal	T_S^{in} [K]	$y_{S,CO}^{in}$	y_{S,CO_2}^{in}	y_{S,H_2O}^{in}	y_{S,H_2}^{in}
0.6	1.0	1589	0.400	0.100	0.187	0.286
0.5	1.0	1644	0.425	0.0825	0.185	0.287

Case 3a and 3b: Moderate disturbance in gasifier flow rate (M_S^{in})

As observed in Table 4.3, there is sizeable variation in assumed nominal feed flow rate to the gasifier across the various literature sources. Solids handling systems also tend to exhibit significant variability in performance, with the nozzles feeding the coal slurry to the gasifier being mentioned as one of the most troublesome components of the gasifier (McDaniel and Hornick, 2002). Taking these considerations into account, case 3a implements a 10% step increase in M_S^{in}, while case 3b implements a 10% step reduction in M_S^{in}.

Case 4: Severe reduction in gasifier flow rate (M_S^{in})

This case is meant to test the RSC/SMR control system under an extreme disturbance. Gasifiers have difficulty maintaining uptime for long periods (McDaniel and Hornick, 2002), and many operational issues are linked to the coal-slurry feed system. This case represents a failure in one of the two coal feed hoppers to the gasifier, and is simulated by a 50% step reduction in M_S^{in}.

4.2.4.1   IMC Tuning Case Study Results

Case 0a and 0b: set point changes

In case 0a (Figure 4.16), for a +1 percentage point step in y_{CH_4} set point, the IMC control response is quite favourable. The new set point for y_{CH_4} is met in under 150 seconds, with

no overshoot in the trajectory. T_{gas} experiences a small peak deviation from set point of -3.0 K, and returns to set point in under 500 seconds. Movements in both MVs are non-oscillatory, and catalyst core and tube wall temperatures throughout the system vary very little.
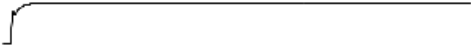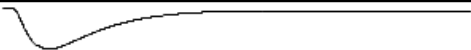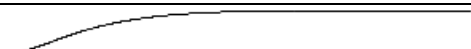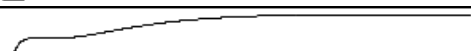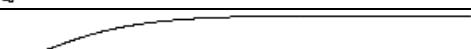
Set Point Change						
Variable	**Units**	**Initial**	**Trend (1000 second span)**	**Final**	**Min %**	**Max %**
y_{CH4}	mol %	3.56		4.56	0.0%	28.1%
Controlled Variables						
Variable	**Units**	**Initial**	**Trend (1000 second span)**	**Final**	**Max Dev**	**IAE**
T_{gas}	K	1177.66		1177.66	-3.01	0.41
y_{CH4}	mol %	3.56		4.56	-1.00	2.98
Manipulated Variables						
Variable	**Units**	**Initial**	**Trend (1000 second span)**	**Final**	**Min %**	**Max %**
F_{SMR}	kmol/hr	26.50		25.36	-4.7%	+0.0%
$R_{S/C}$	mol/mol	3.33		2.95	-11.5%	+0.0%
Other State Variables						
Variable	**Units**	**Initial**	**Trend (1000 second span)**	**Final**	**Min %**	**Max %**
$T_{W|z=0}$	K	1327.99		1328.92	-0.1%	+0.1%
$T_{W|z=0.5L}$	K	1018.26		1023.33	-0.0%	+0.5%
$T_{W|z=L}$	K	852.17		854.40	-0.0%	+0.3%
$T_{cat|z=0}$	K	1174.87		1174.59	-0.3%	+0.0%
$T_{cat|z=0.5L}$	K	934.73		940.00	-0.0%	+0.6%
$T_{cat|z=L}$	K	777.67		777.82	-0.0%	+0.0%
T_S^{out}	K	1013.50		1016.05	-0.0%	+0.3%
ΔP_T	bar	5.43		4.95	-9.9%	+0.0%

Figure 4.16: Counter-current PI response using IMC tuning (Case 0a).

In case 0b (Figure 4.17), it can be seen that the -10 K ramp in T_{gas} set point is easily achieved by the control system. Both CVs return to set point in under 500 seconds, and the peak deviation in y_{CH_4} of +0.04 percentage points is tolerable. The 6.7% increase in F_{SMR} is manageable by the system, and the resultant increase in pressure drop to 5.99 bar is not a cause for concern.
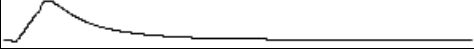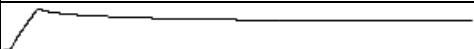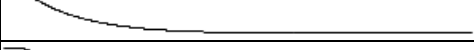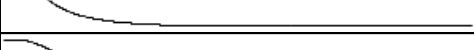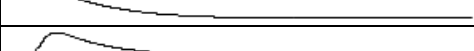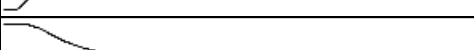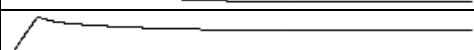
Set Point Change						
Variable	**Units**	**Initial**	**Trend (1000 second span)**	**Final**	**Min %**	**Max %**
T_{gas}	K	1177.66		1167.66	-0.8%	0.0%
Controlled Variables						
Variable	**Units**	**Initial**	**Trend (1000 second span)**	**Final**	**Max Dev**	**IAE**
T_{gas}	K	1177.66		1167.65	+5.07	0.48
y_{CH4}	mol %	3.56		3.56	+0.04	1.69
Manipulated Variables						
Variable	**Units**	**Initial**	**Trend (1000 second span)**	**Final**	**Min %**	**Max %**
F_{SMR}	kmol/hr	26.50		27.77	+0.0%	+6.7%
$R_{S/C}$	mol/mol	3.33		3.50	-0.0%	+5.1%
Other State Variables						
Variable	**Units**	**Initial**	**Trend (1000 second span)**	**Final**	**Min %**	**Max %**
$T_{W|z=0}$	K	1327.99		1319.77	-0.6%	+0.0%
$T_{W|z=0.5L}$	K	1018.26		1010.55	-0.8%	+0.0%
$T_{W|z=L}$	K	852.17		849.09	-0.4%	+0.0%
$T_{cat|z=0}$	K	1174.87		1164.86	-0.9%	+0.0%
$T_{cat|z=0.5L}$	K	934.73		927.54	-0.8%	+0.0%
$T_{cat|z=L}$	K	777.67		777.80	+0.0%	+0.0%
T_S^{out}	K	1013.50		1009.62	-0.4%	+0.0%
ΔP_T	bar	5.43		5.99	+0.0%	+15.4%

Figure 4.17: Counter-current PI response using IMC tuning (Case 0b).

Case 1a and 1b: ±50 K in Shell gas temperature (T_S^{in})

Figure 4.18 and Figure 4.19 illustrate the results from this disturbance. Using IMC tuning, these disturbances were effectively rejected. As seen in Figure 4.18, the peak deviation of T_{gas} from set point is about +4.0 K, and occurs approximately 77 seconds after the T_S^{in} increase (Figure 4.18). For the composition loop (y_{CH_4}), the maximum deviation of -0.08 percentage points occurs 34 seconds after the disturbance (Figure 4.18). Most of the state variables of interest exhibit minimal variation, and settle at values close to the original

69

steady state. However, the maximum tube wall temperature (at $z = 0$) increases by 20 K to 1,347.4 K, due to the increased coal-derived syngas temperature (Figure 4.18). While this is still less than the tube wall design limit of 1,400 K, it is a cause for concern as such a rise, if sustained, may reduce the useful lifetime of the tubes. In Case 1b, the reduction in coal-derived syngas temperature brings about a corresponding 20 K reduction in max tube temperature (Figure 4.19), which is not a cause for concern.
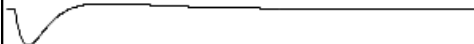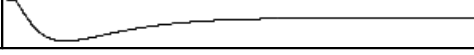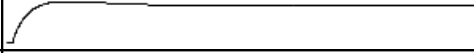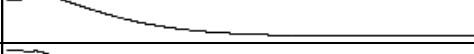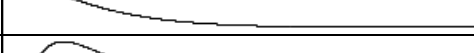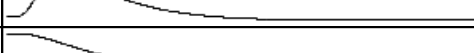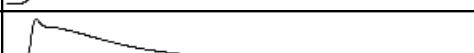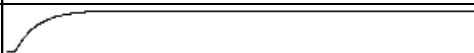
Disturbance Variable						
Variable	**Units**	**Initial**	**Trend (1000 second span)**	**Final**	**Min %**	**Max %**
T_S^{in}	K	1589.15		1639.15	0.0%	3.1%
Controlled Variables						
Variable	**Units**	**Initial**	**Trend (1000 second span)**	**Final**	**Max Dev**	**IAE**
T_{gas}	K	1177.66		1177.66	+4.06	0.69
y_{CH4}	mol %	3.56		3.56	-0.08	2.22
Manipulated Variables						
Variable	**Units**	**Initial**	**Trend (1000 second span)**	**Final**	**Min %**	**Max %**
F_{SMR}	kmol/hr	26.50		28.53	+0.0%	+7.8%
$R_{S/C}$	mol/mol	3.33		3.28	-3.6%	+0.0%
Other State Variables						
Variable	**Units**	**Initial**	**Trend (1000 second span)**	**Final**	**Min %**	**Max %**
$T_{W|z=0}$	K	1327.99		1347.37	+0.0%	+1.6%
$T_{W|z=0.5L}$	K	1018.26		1013.78	-0.4%	+0.1%
$T_{W|z=L}$	K	852.17		849.71	-0.3%	+0.0%
$T_{cat|z=0}$	K	1174.87		1174.53	-0.0%	+0.3%
$T_{cat|z=0.5L}$	K	934.73		928.16	-0.7%	+0.0%
$T_{cat|z=L}$	K	777.67		778.21	+0.0%	+0.1%
T_S^{out}	K	1013.50		1013.44	-0.0%	+0.3%
ΔP_T	bar	5.43		6.38	+0.0%	+17.8%

Figure 4.18: Counter-current PI response using IMC tuning (Case 1a).

Case 1a results in an increase to the pressure drop of 0.9 bar, which is quite tolerable (Figure 4.18). Catalyst core temperatures experience minor perturbations in Case 1a and 1b. Interestingly, the coal-derived syngas exit temperature from the RSC (T_S^{out}) is largely unaffected despite the variation in shell inlet temperature. As seen in Figure 4.18, the increased coal-derived syngas temperature (T_S^{in}) results in the RSC/SMR system being able to maintain the same conversion with a smaller $R_{S/C}$, resulting in greater NG-derived syngas throughput.
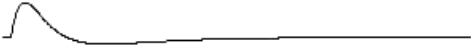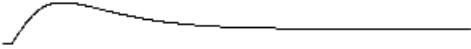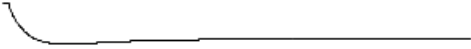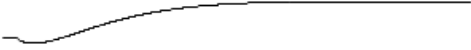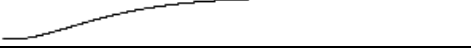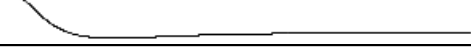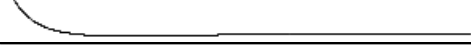
Disturbance Variable						
Variable	**Units**	**Initial**	**Trend (1000 second span)**	**Final**	**Min %**	**Max %**
T_S^{in}	K	1589.15		1539.15	-3.1%	0.0%
Controlled Variables						
Variable	**Units**	**Initial**	**Trend (1000 second span)**	**Final**	**Max Dev**	**IAE**
T_{gas}	K	1177.66		1177.66	-4.19	0.72
y_{CH4}	mol %	3.56		3.56	+0.08	2.40
Manipulated Variables						
Variable	**Units**	**Initial**	**Trend (1000 second span)**	**Final**	**Min %**	**Max %**
F_{SMR}	kmol/hr	26.50		24.41	-8.2%	+0.0%
$R_{S/C}$	mol/mol	3.33		3.38	+0.0%	+3.7%
Other State Variables						
Variable	**Units**	**Initial**	**Trend (1000 second span)**	**Final**	**Min %**	**Max %**
$T_{W|z=0}$	K	1327.99		1309.43	-1.6%	+0.0%
$T_{W|z=0.5L}$	K	1018.26		1023.30	-0.1%	+0.5%
$T_{W|z=L}$	K	852.17		855.08	+0.0%	+0.3%
$T_{cat|z=0}$	K	1174.87		1175.20	-0.3%	+0.0%
$T_{cat|z=0.5L}$	K	934.73		942.10	+0.0%	+0.8%
$T_{cat|z=L}$	K	777.67		777.09	-0.1%	+0.0%
T_S^{out}	K	1013.50		1013.80	-0.3%	+0.0%
ΔP_T	bar	5.43		4.56	-16.8%	+0.0%

Figure 4.19: Counter-current PI response using IMC tuning (Case 1b).

Case 2: Change in the gasifier feed ratios (T_S^{in}, y_S^{in})

This result for Case 2 is quite similar to the result obtained from simulating Case 1a, which illustrates that for the shift in gasifier feed ratios, the corresponding shift in shell gas composition does not have a significant effect on the SMR tube operation. The maximum tube wall temperature and pressure drop increase is greater for Case 2 than Case 1a due to the slightly elevated shell gas inlet temperature.
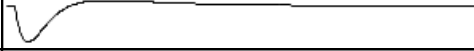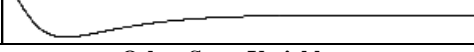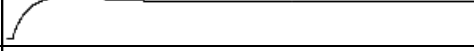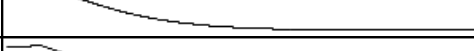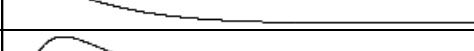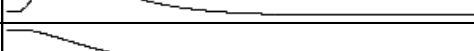
Disturbance Variable						
Variable	**Units**	**Initial**	**Trend (1000 second span)**	**Final**	**Min %**	**Max %**
T_S^{in}	K	1589.15		1644.00	0.0%	3.5%
Controlled Variables						
Variable	**Units**	**Initial**	**Trend (1000 second span)**	**Final**	**Max Dev**	**IAE**
T_{gas}	K	1177.66		1177.66	+5.21	0.89
y_{CH4}	mol %	3.56		3.56	-0.10	2.83
Manipulated Variables						
Variable	**Units**	**Initial**	**Trend (1000 second span)**	**Final**	**Min %**	**Max %**
F_{SMR}	kmol/hr	26.50		29.15	+0.0%	+10.1%
$R_{S/C}$	mol/mol	3.33		3.26	-4.6%	+0.0%
Other State Variables						
Variable	**Units**	**Initial**	**Trend (1000 second span)**	**Final**	**Min %**	**Max %**
$T_{W|z=0}$	K	1327.99		1352.29	+0.0%	+2.1%
$T_{W|z=0.5L}$	K	1018.26		1013.29	-0.5%	+0.1%
$T_{W|z=L}$	K	852.17		849.50	-0.3%	+0.0%
$T_{cat|z=0}$	K	1174.87		1174.44	-0.0%	+0.4%
$T_{cat|z=0.5L}$	K	934.73		926.91	-0.8%	+0.0%
$T_{cat|z=L}$	K	777.67		778.37	+0.0%	+0.1%
T_S^{out}	K	1013.50		1013.90	+0.0%	+0.4%
ΔP_T	bar	5.43		6.68	+0.0%	+23.5%

Figure 4.20: Counter-current PI response using IMC tuning (Case 2).

Case 3a and 3b: ±10% Gasifier flow rate (M_S^{in})

The IMC tuning parameters are able to effectively reject these disturbances. The maximum deviation of T_{gas} from set point occurs 126 seconds after the step disturbance, 48 seconds later than case 1. Settling time for both controllers is also increased.

Disturbance Variable						
Variable	**Units**	**Initial**	**Trend (1000 second span)**	**Final**	**Min %**	**Max %**
M_S^{in}	t/h	237.43		261.17	+0.0%	+10.0%
Controlled Variables						
Variable	**Units**	**Initial**	**Trend (1000 second span)**	**Final**	**Max Dev**	**IAE**
T_{gas}	K	1177.66		1177.66	+1.89	0.51
y_{CH4}	mol %	3.56		3.56	-0.03	1.22
Manipulated Variables						
Variable	**Units**	**Initial**	**Trend (1000 second span)**	**Final**	**Min %**	**Max %**
F_{SMR}	kmol/hr	26.50		28.00	+0.0%	+5.7%
$R_{S/C}$	mol/mol	3.33		3.27	-2.5%	+0.0%
Other State Variables						
Variable	**Units**	**Initial**	**Trend (1000 second span)**	**Final**	**Min %**	**Max %**
$T_{W|z=0}$	K	1327.99		1327.09	-0.1%	+0.1%
$T_{W|z=0.5L}$	K	1018.26		1026.98	+0.0%	+0.9%
$T_{W|z=L}$	K	852.17		859.20	+0.0%	+0.8%
$T_{cat|z=0}$	K	1174.87		1174.89	+0.0%	+0.2%
$T_{cat|z=0.5L}$	K	934.73		939.80	+0.0%	+0.6%
$T_{cat|z=L}$	K	777.67		778.09	+0.0%	+0.1%
T_S^{out}	K	1013.50		1028.22	+0.0%	+1.5%
ΔP_T	bar	5.43		6.17	+0.0%	+13.6%

Figure 4.21: Counter-current PI response using IMC tuning (Case 3a).

State variables in general suffer from less variation than seen in Case 1 and 2. However, the shape of the trend for max tube wall temperature is quite different. Max tube temperature for Case 3a experiences a peak of 1,329.7 K, settling afterwards to a final value of

1,327.1 K (Figure 4.21). In contrast, the maximum tube temperature for Case 3b initially decreases, but settles at an overall hotter steady state of 1,329.2 K (Figure 4.22). Catalyst core temperature variation is less than 6 K at all points along the SMR tube.

Disturbance Variable						
Variable	Units	Initial	Trend (1000 second span)	Final	Min %	Max %
M_S^{in}	t/h	237.43		213.69	-10.0%	+0.0%
Controlled Variables						
Variable	Units	Initial	Trend (1000 second span)	Final	Max Dev	IAE
T_{gas}	K	1177.66		1177.65	-2.02	0.55
y_{CH4}	mol %	3.56		3.56	+0.03	1.32
Manipulated Variables						
Variable	Units	Initial	Trend (1000 second span)	Final	Min %	Max %
F_{SMR}	kmol/hr	26.50		24.87	-6.2%	+0.0%
$R_{S/C}$	mol/mol	3.33		3.40	+0.0%	+2.6%
Other State Variables						
Variable	Units	Initial	Trend (1000 second span)	Final	Min %	Max %
$T_{W|z=0}$	K	1327.99		1329.20	-0.1%	+0.1%
$T_{W|z=0.5L}$	K	1018.26		1008.82	-1.0%	+0.0%
$T_{W|z=L}$	K	852.17		844.81	-0.9%	+0.0%
$T_{cat|z=0}$	K	1174.87		1174.84	-0.2%	+0.0%
$T_{cat|z=0.5L}$	K	934.73		929.23	-0.6%	+0.0%
$T_{cat|z=L}$	K	777.67		777.19	-0.1%	+0.0%
T_S^{out}	K	1013.50		997.60	-1.6%	+0.0%
ΔP_T	bar	5.43		4.70	-13.5%	+0.0%

Figure 4.22: Counter-current PI response using IMC tuning (Case 3b).

Case 4: -50% Gasifier flow rate (M_S^{in})

For this severe disturbance, the IMC tuned controllers perform very well (Figure 4.23). State variable transients generally follow the same pattern and trajectory observed in Case 3b (Figure 4.22). Peak deviation of the temperature T_{gas} from set point is 12 K (Figure

4.23). There is significant reduction in coolant throughput (F_{SMR}) and tube pressure drop (ΔP_T) due to the decreased coal-derived syngas flow. Since the heat duty has been reduced, $R_{S/C}$ has to be increased to obtain the same level of conversion. Temperatures throughout the RSC and SMR tubes generally fall, with the exception of the max tube wall temperature ($T_{W|z=0}$), which increases by 11.3 K. The shell gas exit temperature (T_S^{out}) experiences a significant reduction, which is not detrimental to downstream processes.

Variable	Units	Initial	Trend (1000 second span)	Final	Min %	Max %
Disturbance Variable						
M_S^{in}	t/h	237.43		118.71	-50.0%	+0.0%
Controlled Variables						
Variable	Units	Initial	Trend (1000 second span)	Final	Max Dev	IAE
T_{gas}	K	1177.66		1177.56	-11.96	3.29
y_{CH4}	mol %	3.56		3.56	+0.20	7.83
Manipulated Variables						
Variable	Units	Initial	Trend (1000 second span)	Final	Min %	Max %
F_{SMR}	kmol/hr	26.50		16.76	-36.8%	+0.0%
$R_{S/C}$	mol/mol	3.33		3.64	+0.0%	+14.5%
Other State Variables						
Variable	Units	Initial	Trend (1000 second span)	Final	Min %	Max %
$T_{W|z=0}$	K	1327.99		1339.30	-0.8%	+0.9%
$T_{W|z=0.5L}$	K	1018.26		959.85	-5.7%	+0.0%
$T_{W|z=L}$	K	852.17		810.68	-4.9%	+0.0%
$T_{cat|z=0}$	K	1174.87		1174.45	-1.0%	+0.0%
$T_{cat|z=0.5L}$	K	934.73		900.41	-3.7%	+0.0%
$T_{cat|z=L}$	K	777.67		774.45	-0.4%	+0.0%
T_S^{out}	K	1013.50		917.87	-9.4%	+0.0%
ΔP_T	bar	5.43		1.99	-63.4%	+0.0%

Figure 4.23: Counter-current PI response using IMC tuning (Case 4).

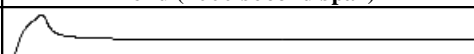#### 4.2.4.2   Optimal Tuning

Significant benefits were observed by using the optimal tuning parameters determined in Section 4.2.3. Two disturbance cases will be used to illustrate this, along with the set point change cases (Figure 4.24 to Figure 4.27).

For all of the cases (Figure 4.24 to Figure 4.27), the overall speed of response is greatly improved by using the optimal PI tuning parameters. As seen in Table 4.12, reduction in IAE from using optimal tuning vs IMC tuning is between 93% and 98% for the temperature loop, and 42% and 86% for the composition loop. The manipulated variables, though more aggressive in general, are non-oscillatory. The state variables of the system generally have quicker transient responses, but settle at the same final value as in the IMC case. This illustrates that the choice of tuning parameters, once able to achieve a stable response, do not have an influence on the final steady-state of the system.

The most severe disturbance (Case 4) effects a maximum deviation in T_{gas} of -1.2 K from set point using the optimal tuning parameters (Figure 4.27). This represents a 90% reduction from the IMC case. In general, using the optimal tuning parameters, the disturbance rejection and set point tracking was found to be excellent for the counter-current configuration.

Table 4.12: IAE values obtained for the set point and disturbance cases using IMC and optimal tuning parameters (Counter-current system).

	T_{gas} IAE			y_{CH_4} IAE		
	IMC	**Optimal**	**Reduction**	**IMC**	**Optimal**	**Reduction**
Case 0a	0.41	0.03	93%	2.98	1.74	42%
Case 0b	0.48	0.03	94%	1.69	0.66	61%
Case 1a	0.69	0.02	97%	2.22	0.35	84%
Case 1b	0.72	0.02	97%	2.4	0.32	87%
Case 2	0.89	0.02	98%	2.83	0.45	84%
Case 3a	0.51	0.01	98%	1.22	0.24	80%
Case 3b	0.55	0.01	98%	1.32	0.24	82%
Case 4	3.29	0.06	98%	7.83	1.13	86%

Table 4.13: Settling times observed for the set point and disturbance cases using IMC and optimal tuning parameters (Counter-current system).

	T_{gas} Settling Time [s]			y_{CH_4} Settling Time [s]		
	IMC	**Optimal**	**Reduction**	**IMC**	**Optimal**	**Reduction**
Case 0a	192	16	92%	148	40	73%
Case 0b	187	0	100%	231	97	58%
Case 1a	283	0	100%	268	37	86%
Case 1b	290	0	100%	307	36	88%
Case 2	314	17	95%	307	40	87%
Case 3a	313	0	100%	149	31	79%
Case 3b	332	0	100%	151	31	79%
Case 4	617	29	95%	549	100	82%

Table 4.12 illustrates the comparison of IAE obtained for all the cases via the different tunings, and Table 4.13 compares the settling times observed. For all of the cases investigated, settling time for the controller is defined as the following: for T_{gas}, it is the time taken for the temperature to return to within ±1 K of the T_{gas} set point; for y_{CH_4}, it is the time taken to return to within ±0.01 percentage points of the y_{CH_4} set point.

Using the IMC tuning parameters, with the exception of Case 4, the average settling time for T_{gas} is 4.5 minutes, and average settling time for y_{CH_4} is 3.7 minutes (Table 4.13). This settling time falls in line with the expected gasifier dynamics, and is quite good for an initial estimate of tuning parameters. The settling time for both controllers in Case 4 is approximately 10 minutes using IMC tuning (see Figure 4.23 for trajectories). Significant improvements in performance for all cases were observed by switching to the optimal tuning parameters. For Case 4, after a 50% reduction in the gasifier flow rate, T_{gas} is brought back around its set point within 0.5 minutes (Figure 4.27, Table 4.13). The average settling time across both controllers was reduced by 88% using the optimal tuning parameters (Table 4.13). For several of the cases using optimal tuning (case 0b, 1a, 1b, 3a, 3b), the T_{gas} settling time was reported in Table 4.13 as zero seconds. For those cases, this is due to T_{gas} staying within ±1 K of the set point at all times throughout its trajectory (e.g.: Figure 4.25), which was the defined criterion for settling time.
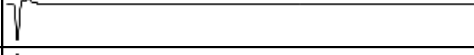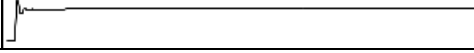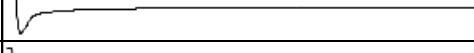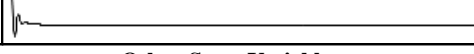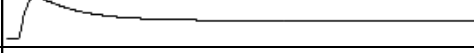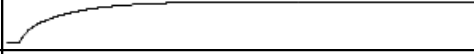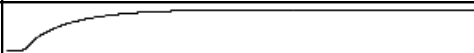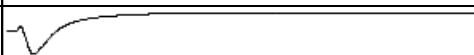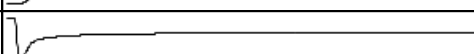
Set Point Change						
Variable	**Units**	**Initial**	**Trend (1000 second span)**	**Final**	**Min %**	**Max %**
y_{CH4}	mol %	3.56		4.56	0.0%	+28.1%
Controlled Variables						
Variable	**Units**	**Initial**	**Trend (1000 second span)**	**Final**	**Max Dev**	**IAE**
T_{gas}	K	1177.66		1177.66	-2.82	0.03
y_{CH4}	mol %	3.56		4.56	-1.00	1.74
Manipulated Variables						
Variable	**Units**	**Initial**	**Trend (1000 second span)**	**Final**	**Min %**	**Max %**
F_{SMR}	kmol/hr	26.50		25.36	-11.5%	+0.0%
$R_{S/C}$	mol/mol	3.33		2.95	-15.9%	+0.0%
Other State Variables						
Variable	**Units**	**Initial**	**Trend (1000 second span)**	**Final**	**Min %**	**Max %**
$T_{W|z=0}$	K	1327.99		1328.92	-0.0%	+0.2%
$T_{W|z=0.5L}$	K	1018.26		1023.33	-0.0%	+0.5%
$T_{W|z=L}$	K	852.17		854.40	-0.0%	+0.3%
$T_{cat|z=0}$	K	1174.87		1174.58	-0.1%	+0.0%
$T_{cat|z=0.5L}$	K	934.73		939.99	-0.0%	+0.6%
$T_{cat|z=L}$	K	777.67		777.82	-0.0%	+0.0%
T_S^{out}	K	1013.50		1016.05	-0.0%	+0.3%
ΔP_T	bar	5.43		4.95	-23.4%	+0.0%

Figure 4.24: Counter-current PI response using optimal tuning (Case 0a).
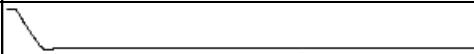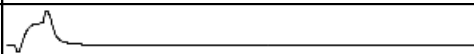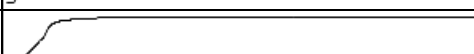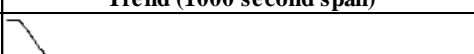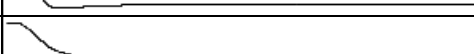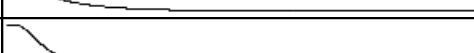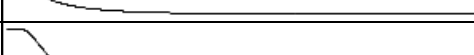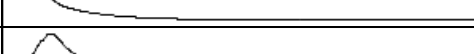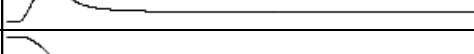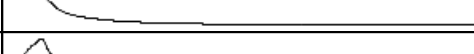
Set Point Change						
Variable	**Units**	**Initial**	**Trend (1000 second span)**	**Final**	**Min %**	**Max %**
T_{gas}	K	1177.66		1167.66	-0.8%	+0.0%
Controlled Variables						
Variable	**Units**	**Initial**	**Trend (1000 second span)**	**Final**	**Max Dev**	**IAE**
T_{gas}	K	1177.66		1167.66	+0.79	0.03
y_{CH4}	mol %	3.56		3.56	+0.04	0.66
Manipulated Variables						
Variable	**Units**	**Initial**	**Trend (1000 second span)**	**Final**	**Min %**	**Max %**
F_{SMR}	kmol/hr	26.50		27.77	-0.0%	+12.3%
$R_{S/C}$	mol/mol	3.33		3.50	-0.2%	+5.0%
Other State Variables						
Variable	**Units**	**Initial**	**Trend (1000 second span)**	**Final**	**Min %**	**Max %**
$T_{W|z=0}$	K	1327.99		1319.78	-0.7%	+0.0%
$T_{W|z=0.5L}$	K	1018.26		1010.55	-0.8%	+0.0%
$T_{W|z=L}$	K	852.17		849.09	-0.4%	+0.0%
$T_{cat|z=0}$	K	1174.87		1164.86	-0.9%	+0.0%
$T_{cat|z=0.5L}$	K	934.73		927.55	-0.8%	+0.0%
$T_{cat|z=L}$	K	777.67		777.80	+0.0%	+0.1%
T_S^{out}	K	1013.50		1009.62	-0.4%	+0.0%
ΔP_T	bar	5.43		5.98	-0.0%	+29.2%

Figure 4.25: Counter-current PI response using optimal tuning (Case 0b).

Disturbance Variable						
Variable	**Units**	**Initial**	**Trend (1000 second span)**	**Final**	**Min %**	**Max %**
T_S^{in}	K	1589.15		1644.00	-0.0%	+3.5%
Controlled Variables						
Variable	**Units**	**Initial**	**Trend (1000 second span)**	**Final**	**Max Dev**	**IAE**
T_{gas}	K	1177.66		1177.66	+1.01	0.02
y_{CH4}	mol %	3.56		3.56	-0.06	0.45
Manipulated Variables						
Variable	**Units**	**Initial**	**Trend (1000 second span)**	**Final**	**Min %**	**Max %**
F_{SMR}	kmol/hr	26.50		29.15	-0.0%	+11.4%
$R_{S/C}$	mol/mol	3.33		3.26	-2.9%	+0.0%
Other State Variables						
Variable	**Units**	**Initial**	**Trend (1000 second span)**	**Final**	**Min %**	**Max %**
$T_{W|z=0}$	K	1327.99		1352.29	+0.0%	+1.8%
$T_{W|z=0.5L}$	K	1018.26		1013.29	-0.5%	+0.0%
$T_{W|z=L}$	K	852.17		849.50	-0.3%	+0.0%
$T_{cat|z=0}$	K	1174.87		1174.44	-0.0%	+0.0%
$T_{cat|z=0.5L}$	K	934.73		926.90	-0.8%	+0.0%
$T_{cat|z=L}$	K	777.67		778.37	-0.0%	+0.1%
T_S^{out}	K	1013.50		1013.89	+0.0%	+0.4%
ΔP_T	bar	5.43		6.68	-0.0%	+27.0%

Figure 4.26: Counter-current PI response using optimal tuning (Case 2).
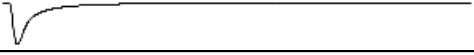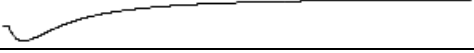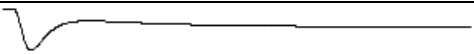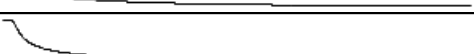
Disturbance Variable						
Variable	**Units**	**Initial**	**Trend (1000 second span)**	**Final**	**Min %**	**Max %**
M_S^{in}	t/h	237.43		118.71	-50.0%	+0.0%
Controlled Variables						
Variable	**Units**	**Initial**	**Trend (1000 second span)**	**Final**	**Max Dev**	**IAE**
T_{gas}	K	1177.66		1177.65	-1.22	0.06
y_{CH4}	mol %	3.56		3.56	+0.07	1.13
Manipulated Variables						
Variable	**Units**	**Initial**	**Trend (1000 second span)**	**Final**	**Min %**	**Max %**
F_{SMR}	kmol/hr	26.50		16.78	-36.7%	+0.0%
$R_{S/C}$	mol/mol	3.33		3.64	+0.0%	+9.2%
Other State Variables						
Variable	**Units**	**Initial**	**Trend (1000 second span)**	**Final**	**Min %**	**Max %**
$T_{W\|z=0}$	K	1327.99		1339.27	-0.5%	+0.8%
$T_{W\|z=0.5L}$	K	1018.26		960.24	-5.7%	+0.0%
$T_{W\|z=L}$	K	852.17		810.81	-4.9%	+0.0%
$T_{cat\|z=0}$	K	1174.87		1174.57	-0.1%	+0.0%
$T_{cat\|z=0.5L}$	K	934.73		900.78	-3.6%	+0.0%
$T_{cat\|z=L}$	K	777.67		774.46	-0.4%	+0.0%
T_S^{out}	K	1013.50		918.10	-9.4%	+0.0%
ΔP_T	bar	5.43		2.00	-63.3%	+0.0%

Figure 4.27: Counter-current PI response using optimal tuning (Case 4).

4.3   Control Development and Analysis (Co-current)

As was the case for the counter-current system, the CVs and MVs considered for the co-current control structure are the same, as listed in Table 4.6. The key difference in the co-current design is that the CVs are now situated at the RSC exit, whereas the MVs are situated at the RSC inlet, as illustrated in Figure 4.29.

4.3.1   Open Loop Step Test and Relative Gain Array

As with the counter-current configuration, open loop step testing was performed on each input separately. The simulation procedure was previously described in Section 4.2.1. While the CV responses have the same gain direction as observed with the counter-current system, the process time constants are longer for the co-current case.
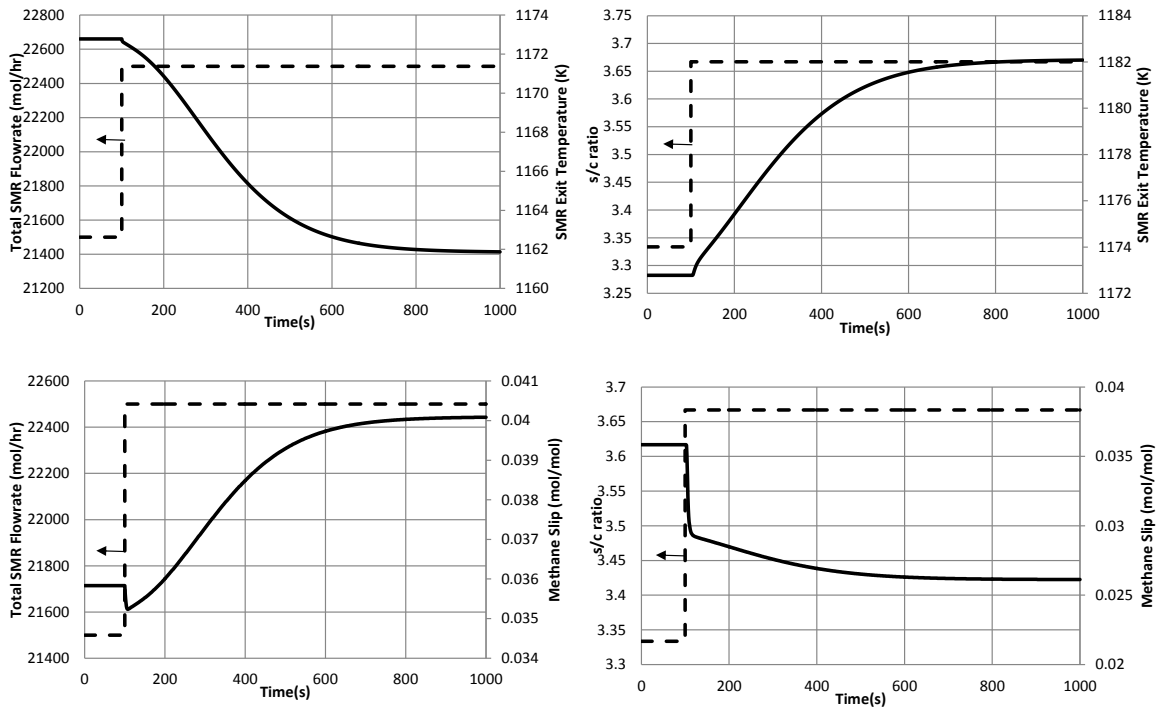
Figure 4.28: Open Loop response data for the co-current configuration.

The dynamics of the co-current open loop response bear elements of non-linear interaction (Figure 4.28), and the responses are less first order than the counter-current responses (Figure 4.11). The initial inverse response of the y_{CH_4} from a step change in F_{SMR} is more prominent than it was for the counter-current configuration. These non-linearities may result in co-current control being less straightforward to design than counter-current.

Table 4.14: Process parameters derived from co-current open loop step tests.

T_{gas}			y_{CH_4}		
K_P	τ_P	θ_D	K_P	τ_P	θ_D
-0.01059	195	1	-0.02890	9	3

The RGA was determined for the co-current configuration to be:

$$RGA = \begin{bmatrix} 1.58 & -0.58 \\ -0.58 & 1.58 \end{bmatrix} \tag{4.8}$$

The RGA analysis suggests F_{SMR} should be used to control T_{gas}, and $R_{S/C}$ should be used to control y_{CH_4}. The RGA parameter λ_{11} suggests that the co-current loop interaction is less significant than for counter-current, but this only takes the steady-state gains into consideration. Figure 4.29 illustrates the control design for the co-current case based on this analysis.
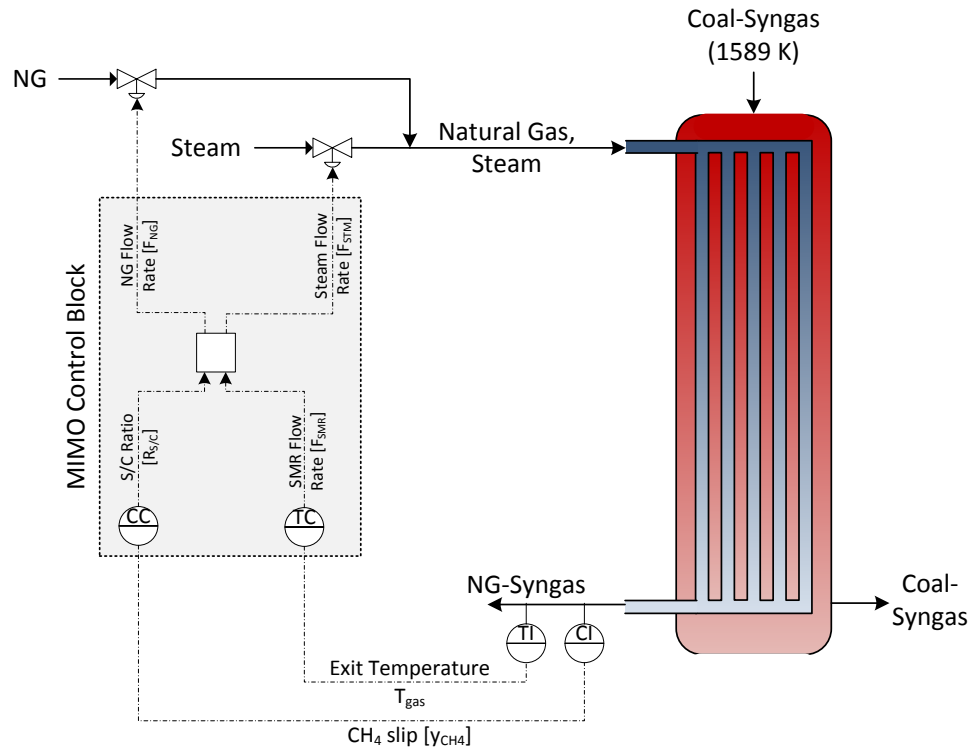
Figure 4.29: Control design illustration for co-current case.

4.3.2   Optimal Tuning Parameters for Set Point Changes

To obtain control that performs well for both disturbance rejection and set point changes, the dynamic optimization tool in gPROMS was used. For the co-current case, the objective function to be minimized is analogous to the formulation shown in equations (4.3) to (4.7).

While IMC tuning parameters provide a good initial point for acceptable control performance, it was observed with the counter-current analysis that significant improvements can be made upon finding optimal tuning parameters. Set point changes were used as the basis for optimization, as that tends to be more demanding on the MVs than disturbance rejection (due to initial sudden movements after a set point change).

Since the co-current design has longer time delay, the optimization time window was increased accordingly to 2,000 seconds. The dynamic optimization run initially starts at

steady-state, with T_{gas} and y_{CH_4} at their respective set points. At time zero, a -10 K ramp in the T_{gas} set point is implemented over a period of sixty seconds, and maintained at the new set point for the remainder of the 2,000 second run. At time 1,000 seconds, a +1.0 percentage point step in the y_{CH_4} set point is implemented, and maintained at that new set point for the remainder of the 2,000 second run. As with the counter-current study, the co-current IMC tuning parameters were used as an initial guess for the optimization.

μ was fixed at 0.5 for all co-current runs, as it was found to yield balanced results with the counter-current design, and adjusting μ around this value did not result in a significant change in performance.

4.3.3   Control Case Studies

The disturbance and set point change cases described in Section 4.2.4 were used to assess the co-current control configuration in order to provide a fair comparison with the counter-current control performance. Note however that due to the nature of the inherent dynamics of the co-current system, settling time is significantly increased, and all simulations discussed in Section 4.3.3.1 span 2,000 seconds, as opposed to the 1,000 second simulations used for the counter-current analyses.

4.3.3.1   IMC and Optimal Tuning

Despite the increase in settling time, the co-current control performance for all of the cases (with the exception of Case 4) is overall satisfactory. Table 4.15 shows the comparison of IAE for the cases via the IMC and optimal tunings, while Table 4.16 compares observed settling times. The improvements in IAE by using optimal tuning vs. IMC tuning is still significant (61% on average), but this increase is smaller than that observed with the counter-current design (86% on average). Using optimal tuning parameters, the average settling time observed for T_{gas} and y_{CH_4} is 8.3 minutes and 2.7 minutes respectively (Table 4.16), which is acceptable, considering the expected dynamics of the gasifier sys-

tem. The system trajectories are similar between IMC and optimal tuning, so only the optimal results will be presented (Figure 4.30 to Figure 4.37).

Table 4.15: IAE values obtained for the SP and disturbance cases using IMC and optimal tuning parameters (Co-current system).

	T_{gas} IAE			y_{CH_4} IAE		
	IMC	**Optimal**	**Reduction**	**IMC**	**Optimal**	**Reduction**
Case 0a	1.58	0.62	61%	4.03	2.34	42%
Case 0b	2.33	1.11	52%	2.15	1.36	37%
Case 1a	3.81	1.50	61%	4.02	0.98	76%
Case 1b	3.92	1.56	60%	4.48	1.23	73%
Case 2	4.93	1.94	61%	5.13	1.23	76%
Case 3a	2.77	1.09	61%	3.04	0.78	74%
Case 3b	2.97	1.30	56%	3.74	1.21	68%
Case 4	51.42	41.01	20%	67.65	261.78	-287%

Table 4.16: Settling times observed for the set point and disturbance cases using IMC and optimal tuning parameters (Co-current system).

	T_{gas} Settling time [s]			y_{CH_4} Settling Time [s]		
	IMC	**Opt PI**	**Reduction**	**IMC**	**Opt PI**	**Reduction**
Case 0a	584	302	48%	182	52	71%
Case 0b	698	582	17%	398	238	40%
Case 1a	1108	490	56%	650	192	70%
Case 1b	1090	502	54%	746	188	75%
Case 2	1196	786	34%	664	210	68%
Case 3a	918	396	57%	548	124	77%
Case 3b	714	418	41%	662	138	79%
Case 4	N/A	N/A	N/A	N/A	N/A	N/A

The co-current system is still able to achieve fast y_{CH_4} set point changes (Figure 4.30), but the delay associated with a T_{gas} set point change (Figure 4.31) is significantly larger than found with counter-current using IMC tuning (Figure 4.17).

Overall, for co-current, tube wall and catalyst core temperatures exhibit on average, 5 - 10 K larger variations during transients, as compared to counter-current. However, this is not a significant issue, as the absolute temperatures are lower for the co-current system and

therefore do not threaten the maximum temperature thresholds. For example, in Case 2, the co-current design max tube wall temperature increases by 33 K (Figure 4.34), which is larger than the 24 K rise seen for the counter-current design (Figure 4.26). However, the counter-current final temperature of 1,352 K is substantially closer to the 1,400 K design limit than the co-current temperature of 1,247 K.

For all of the cases explored, the co-current system states exhibit oscillation, which may not be acceptable if the disturbance is also oscillatory. While the co-current system can handle moderate shell flow rate disturbances (Figure 4.35 and Figure 4.36), the severe disturbance case (Case 4) results in unstable performance with both IMC and optimal tuning. With IMC tuning (Figure 4.38), average catalyst and tube wall temperature fluctuations exceed 100 K in a short time span, likely encouraging material failure. With optimal tuning (Figure 4.37), the Case 4 performance is even worse, with both MVs cycling between their lower and upper bounds. Due to the flow rate of tube gas hitting its lower bound, cooling duty is effectively eliminated, and maximum tube temperature surpasses the 1,400 K design limit (Figure 4.37). This will result in catastrophic tube failure, and shows the need for a minimum flow rate above the lower bound (fully closed) during gasifier operation to protect the tubes. In Case 4, catalyst core temperatures in the midsection of the tube also experience a rapid 300 K thermal swing (Figure 4.37), which will result in sintering.

Overall, for the co-current system (with the exception of Case 4), all investigated cases can be effectively controlled using both IMC and optimal tuning parameters.
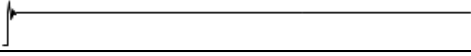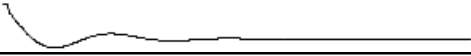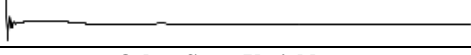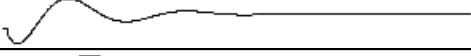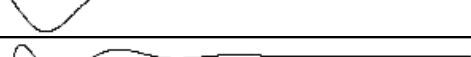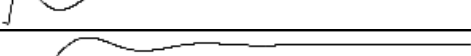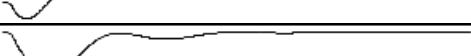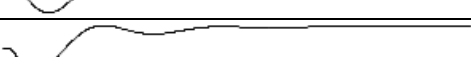
Set Point Change						
Variable	**Units**	**Initial**	**Trend (2000 second span)**	**Final**	**Min %**	**Max %**
y_{CH4}	mol %	3.58		4.58	-0.0%	+27.9%
Controlled Variables						
Variable	**Units**	**Initial**	**Trend (2000 second span)**	**Final**	**Max Dev**	**IAE**
T_{gas}	K	1172.78		1172.78	-2.48	0.62
y_{CH4}	mol %	3.58		4.58	-1.00	2.34
Manipulated Variables						
Variable	**Units**	**Initial**	**Trend (2000 second span)**	**Final**	**Min %**	**Max %**
F_{SMR}	kmol/hr	21.50		20.60	-5.1%	+0.0%
$R_{S/C}$	mol/mol	3.33		2.95	-18.6%	+0.0%
Other State Variables						
Variable	**Units**	**Initial**	**Trend (2000 second span)**	**Final**	**Min %**	**Max %**
$T_{W|z=0}$	K	1214.28		1215.55	-0.1%	+0.2%
$T_{W|z=0.5L}$	K	1165.86		1168.30	-0.1%	+0.3%
$T_{W|z=L}$	K	1182.62		1183.09	-0.2%	+0.0%
$T_{cat|z=0}$	K	776.33		776.54	-0.0%	+0.0%
$T_{cat|z=0.5L}$	K	1113.59		1115.89	-0.2%	+0.3%
$T_{cat|z=L}$	K	1172.58		1172.55	-0.2%	+0.0%
T_S^{out}	K	1206.57		1207.70	-0.1%	+0.1%
ΔP_T	bar	3.99		3.65	-10.6%	+0.0%

Figure 4.30: Co-current PI response using Optimal Tuning (Case 0a).
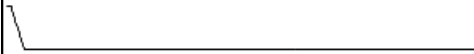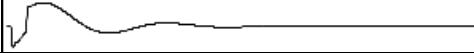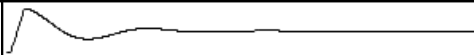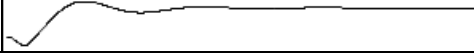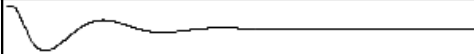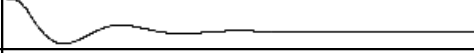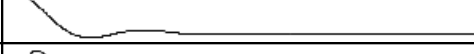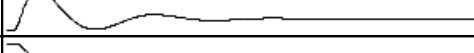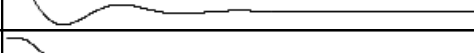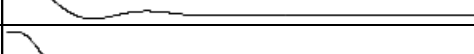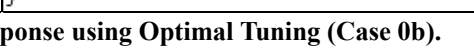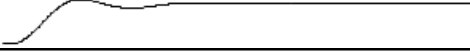
Set Point Change						
Variable	**Units**	**Initial**	**Trend (2000 second span)**	**Final**	**Min %**	**Max %**
T_{gas}	K	1172.78		1162.78	-0.9%	+0.0%
Controlled Variables						
Variable	**Units**	**Initial**	**Trend (2000 second span)**	**Final**	**Max Dev**	**IAE**
T_{gas}	K	1172.78		1162.78	+8.24	1.11
y_{CH4}	mol %	3.58		3.58	+0.02	1.36
Manipulated Variables						
Variable	**Units**	**Initial**	**Trend (2000 second span)**	**Final**	**Min %**	**Max %**
F_{SMR}	kmol/hr	21.50		22.81	+0.0%	+12.5%
$R_{S/C}$	mol/mol	3.33		3.50	-1.6%	+6.2%
Other State Variables						
Variable	**Units**	**Initial**	**Trend (2000 second span)**	**Final**	**Min %**	**Max %**
$T_{W|z=0}$	K	1214.28		1208.41	-0.9%	+0.0%
$T_{W|z=0.5L}$	K	1165.86		1156.75	-1.1%	+0.0%
$T_{W|z=L}$	K	1182.62		1173.20	-0.9%	+0.0%
$T_{cat|z=0}$	K	776.33		776.52	+0.0%	+0.1%
$T_{cat|z=0.5L}$	K	1113.59		1103.97	-1.2%	+0.0%
$T_{cat|z=L}$	K	1172.58		1162.56	-0.9%	+0.0%
T_S^{out}	K	1206.57		1199.36	-0.7%	+0.0%
ΔP_T	bar	3.99		4.49	+0.0%	+28.5%

Figure 4.31: Co-current PI response using Optimal Tuning (Case 0b).
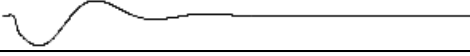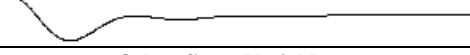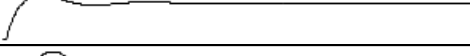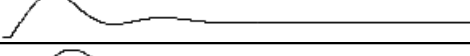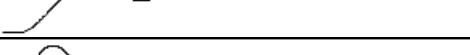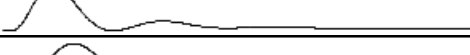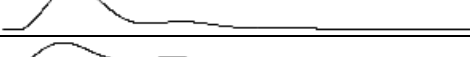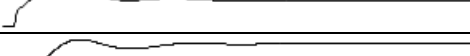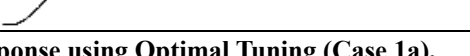
Disturbance Variable						
Variable	**Units**	**Initial**	**Trend (2000 second span)**	**Final**	**Min %**	**Max %**
T_S^{in}	K	1589.15		1639.15	-0.0%	+3.1%
Controlled Variables						
Variable	**Units**	**Initial**	**Trend (2000 second span)**	**Final**	**Max Dev**	**IAE**
T_{gas}	K	1172.78		1172.80	+4.96	1.50
y_{CH4}	mol %	3.58		3.58	-0.01	0.98
Manipulated Variables						
Variable	**Units**	**Initial**	**Trend (2000 second span)**	**Final**	**Min %**	**Max %**
F_{SMR}	kmol/hr	21.50		23.67	-0.0%	+10.9%
$R_{S/C}$	mol/mol	3.33		3.26	-5.2%	+0.0%
Other State Variables						
Variable	**Units**	**Initial**	**Trend (2000 second span)**	**Final**	**Min %**	**Max %**
$T_{W|z=0}$	K	1214.28		1240.84	+0.0%	+2.7%
$T_{W|z=0.5L}$	K	1165.86		1169.14	-0.0%	+0.9%
$T_{W|z=L}$	K	1182.62		1183.92	-0.0%	+0.5%
$T_{cat|z=0}$	K	776.33		777.02	-0.0%	+0.1%
$T_{cat|z=0.5L}$	K	1113.59		1113.92	-0.0%	+0.7%
$T_{cat|z=L}$	K	1172.58		1172.57	-0.0%	+0.4%
T_S^{out}	K	1206.57		1211.83	+0.0%	+0.7%
ΔP_T	bar	3.99		4.92	+0.0%	+25.5%

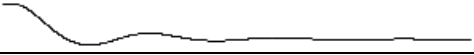**Figure 4.32: Co-current PI response using Optimal Tuning (Case 1a).**
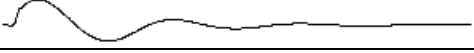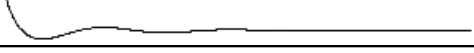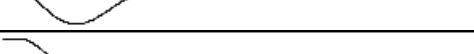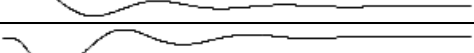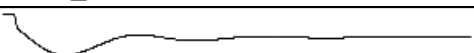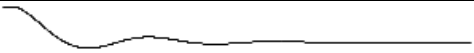
Disturbance Variable						
Variable	**Units**	**Initial**	**Trend (2000 second span)**	**Final**	**Min %**	**Max %**
T_S^{in}	K	1589.15		1539.15	-3.1%	+0.0%
Controlled Variables						
Variable	**Units**	**Initial**	**Trend (2000 second span)**	**Final**	**Max Dev**	**IAE**
T_{gas}	K	1172.78		1172.73	-5.15	1.56
y_{CH4}	mol %	3.58		3.58	+0.01	1.23
Manipulated Variables						
Variable	**Units**	**Initial**	**Trend (2000 second span)**	**Final**	**Min %**	**Max %**
F_{SMR}	kmol/hr	21.50		19.26	-12.0%	+0.0%
$R_{S/C}$	mol/mol	3.33		3.40	-0.0%	+5.4%
Other State Variables						
Variable	**Units**	**Initial**	**Trend (2000 second span)**	**Final**	**Min %**	**Max %**
$T_{W|z=0}$	K	1214.28		1189.38	-2.6%	+0.0%
$T_{W|z=0.5L}$	K	1165.86		1163.01	-0.9%	+0.0%
$T_{W|z=L}$	K	1182.62		1181.24	-0.5%	+0.0%
$T_{cat|z=0}$	K	776.33		775.58	-0.1%	+0.0%
$T_{cat|z=0.5L}$	K	1113.59		1114.02	-0.7%	+0.2%
$T_{cat|z=L}$	K	1172.58		1172.55	-0.4%	+0.0%
T_S^{out}	K	1206.57		1201.20	-0.8%	+0.0%
ΔP_T	bar	3.99		3.16	-24.0%	+0.0%

Figure 4.33: Co-current PI response using Optimal Tuning (Case 1b).
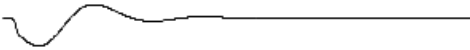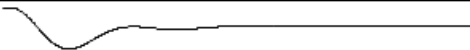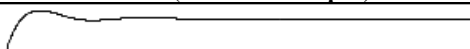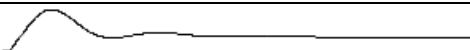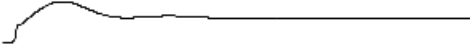
Disturbance Variable						
Variable	Units	Initial	Trend (2000 second span)	Final	Min %	Max %
T_S^{in}	K	1589.15		1644.00	+0.0%	+3.5%
Controlled Variables						
Variable	Units	Initial	Trend (2000 second span)	Final	Max Dev	IAE
T_{gas}	K	1172.78		1172.80	+6.40	1.94
y_{CH4}	mol %	3.58		3.58	-0.02	1.23
Manipulated Variables						
Variable	Units	Initial	Trend (2000 second span)	Final	Min %	Max %
F_{SMR}	kmol/hr	21.50		24.31	+0.0%	+13.9%
$R_{S/C}$	mol/mol	3.33		3.24	-6.8%	+0.0%
Other State Variables						
Variable	Units	Initial	Trend (2000 second span)	Final	Min %	Max %
$T_{W|z=0}$	K	1214.28		1247.59	+0.0%	+3.5%
$T_{W|z=0.5L}$	K	1165.86		1170.16	+0.0%	+1.1%
$T_{W|z=L}$	K	1182.62		1184.35	+0.0%	+0.6%
$T_{cat|z=0}$	K	776.33		777.22	+0.0%	+0.1%
$T_{cat|z=0.5L}$	K	1113.59		1113.98	+0.0%	+0.9%
$T_{cat|z=L}$	K	1172.58		1172.56	-0.0%	+0.5%
T_S^{out}	K	1206.57		1213.47	+0.0%	+1.0%
ΔP_T	bar	3.99		5.22	+0.0%	+33.4%

Figure 4.34: Co-current PI response using Optimal Tuning (Case 2).
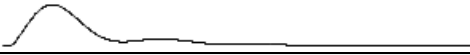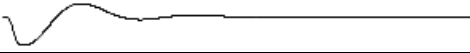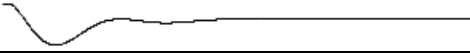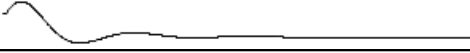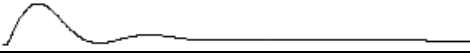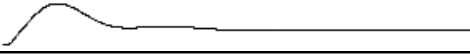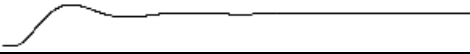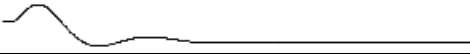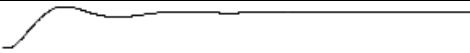
Disturbance Variable						
Variable	**Units**	**Initial**	**Trend (2000 second span)**	**Final**	**Min %**	**Max %**
M_S^{in}	t/h	237.43		261.17	-0.0%	+10.0%
Controlled Variables						
Variable	**Units**	**Initial**	**Trend (2000 second span)**	**Final**	**Max Dev**	**IAE**
T_{gas}	K	1172.78		1172.79	+3.98	1.09
y_{CH4}	mol %	3.58		3.58	-0.01	0.78
Manipulated Variables						
Variable	**Units**	**Initial**	**Trend (2000 second span)**	**Final**	**Min %**	**Max %**
F_{SMR}	kmol/hr	21.50		23.07	+0.0%	+8.3%
$R_{S/C}$	mol/mol	3.33		3.28	-4.0%	+0.0%
Other State Variables						
Variable	**Units**	**Initial**	**Trend (2000 second span)**	**Final**	**Min %**	**Max %**
$T_{W|z=0}$	K	1214.28		1209.65	-0.5%	+0.2%
$T_{W|z=0.5L}$	K	1165.86		1166.53	+0.0%	+0.5%
$T_{W|z=L}$	K	1182.62		1184.50	+0.0%	+0.5%
$T_{cat|z=0}$	K	776.33		776.83	+0.0%	+0.1%
$T_{cat|z=0.5L}$	K	1113.59		1109.91	-0.4%	+0.3%
$T_{cat|z=L}$	K	1172.58		1172.55	-0.0%	+0.3%
T_S^{out}	K	1206.57		1213.14	+0.0%	+0.8%
ΔP_T	bar	3.99		4.63	+0.0%	+18.7%

Figure 4.35: Co-current PI response using Optimal Tuning (Case 3a).
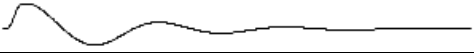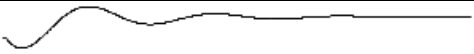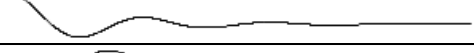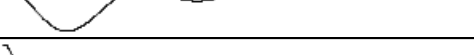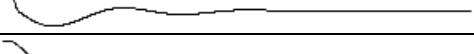
Disturbance Variable						
Variable	**Units**	**Initial**	**Trend (2000 second span)**	**Final**	**Min %**	**Max %**
M_S^{in}	t/h	237.43		213.69	-10.0%	+0.0%
Controlled Variables						
Variable	**Units**	**Initial**	**Trend (2000 second span)**	**Final**	**Max Dev**	**IAE**
T_{gas}	K	1172.78		1172.75	-4.51	1.30
y_{CH4}	mol %	3.58		3.58	+0.01	1.21
Manipulated Variables						
Variable	**Units**	**Initial**	**Trend (2000 second span)**	**Final**	**Min %**	**Max %**
F_{SMR}	kmol/hr	21.50		19.81	-10.0%	+0.0%
$R_{S/C}$	mol/mol	3.33		3.38	+0.0%	+4.6%
Other State Variables						
Variable	**Units**	**Initial**	**Trend (2000 second span)**	**Final**	**Min %**	**Max %**
$T_{W|z=0}$	K	1214.28		1220.09	-0.2%	+0.7%
$T_{W|z=0.5L}$	K	1165.86		1165.55	-0.6%	+0.1%
$T_{W|z=L}$	K	1182.62		1180.73	-0.5%	+0.0%
$T_{cat|z=0}$	K	776.33		775.77	-0.1%	+0.0%
$T_{cat|z=0.5L}$	K	1113.59		1118.01	-0.3%	+0.6%
$T_{cat|z=L}$	K	1172.58		1172.57	-0.4%	+0.0%
T_S^{out}	K	1206.57		1199.96	-0.9%	+0.0%
ΔP_T	bar	3.99		3.36	-19.9%	+0.0%

Figure 4.36: Co-current PI response using Optimal Tuning (Case 3b).

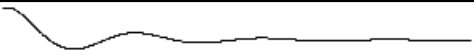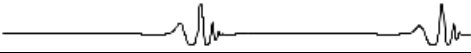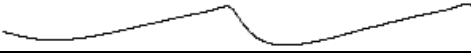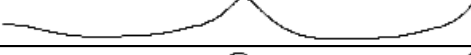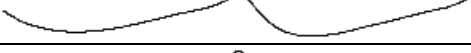| Disturbance Variable						
Variable	**Units**	**Initial**	**Trend (2000 second span)**	**Final**	**Min %**	**Max %**
M_S^{in}	t/h	237.43		118.71	-50.0%	+0.0%
Controlled Variables						
Variable	**Units**	**Initial**	**Trend (2000 second span)**	**Final**	**Max Dev**	**IAE**
T_{gas}	K	1172.78		1242.15	+71.78	41.01
y_{CH4}	mol %	3.58		3.38	+8.78	261.78
Manipulated Variables						
Variable	**Units**	**Initial**	**Trend (2000 second span)**	**Final**	**Min %**	**Max %**
F_{SMR}	kmol/hr	21.50		30.37	-100.0%	+60.4%
$R_{S/C}$	mol/mol	3.33		1.87	-70.0%	+200.0%
Other State Variables						
Variable	**Units**	**Initial**	**Trend (2000 second span)**	**Final**	**Min %**	**Max %**
$T_{W|z=0}$	K	1214.28		1230.63	-5.8%	+23.5%
$T_{W|z=0.5L}$	K	1165.86		1338.31	-6.8%	+15.7%
$T_{W|z=L}$	K	1182.62		1230.80	-3.7%	+5.6%
$T_{cat|z=0}$	K	776.33		777.31	-2.9%	+0.6%
$T_{cat|z=0.5L}$	K	1113.59		1338.19	-5.9%	+20.6%
$T_{cat|z=L}$	K	1172.58		1220.47	-3.0%	+6.0%
T_S^{out}	K	1206.57		1254.67	-5.9%	+4.9%
ΔP_T	bar	3.99		9.63	-100.0%	+216.4%

Figure 4.37: Co-current PI response using Optimal Tuning (Case 4).
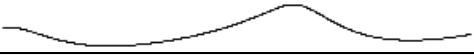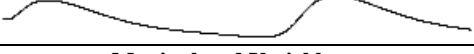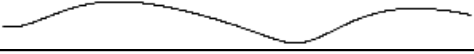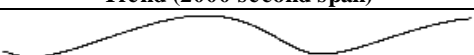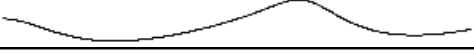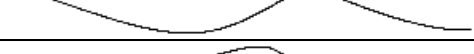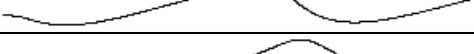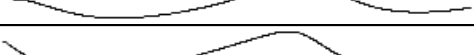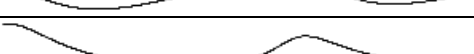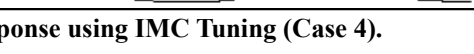
Disturbance Variable						
Variable	**Units**	**Initial**	**Trend (2000 second span)**	**Final**	**Min %**	**Max %**
M_S^{in}	t/h	237.43		118.71	-50.0%	+0.0%
Controlled Variables						
Variable	**Units**	**Initial**	**Trend (2000 second span)**	**Final**	**Max Dev**	**IAE**
T_{gas}	K	1172.78		1154.04	+59.95	51.42
y_{CH4}	mol %	3.58		3.48	+0.26	67.65
Manipulated Variables						
Variable	**Units**	**Initial**	**Trend (2000 second span)**	**Final**	**Min %**	**Max %**
F_{SMR}	kmol/hr	21.50		6.59	-71.9%	+0.0%
$R_{S/C}$	mol/mol	3.33		4.05	-28.0%	+45.4%
Other State Variables						
Variable	**Units**	**Initial**	**Trend (2000 second span)**	**Final**	**Min %**	**Max %**
$T_{W|z=0}$	K	1214.28		1326.73	-1.7%	+10.1%
$T_{W|z=0.5L}$	K	1165.86		1206.25	-5.4%	+8.9%
$T_{W|z=L}$	K	1182.62		1156.52	-4.7%	+4.1%
$T_{cat|z=0}$	K	776.33		768.61	-1.1%	+0.0%
$T_{cat|z=0.5L}$	K	1113.59		1189.46	-3.8%	+13.3%
$T_{cat|z=L}$	K	1172.58		1150.40	-4.2%	+5.0%
T_S^{out}	K	1206.57		1173.07	-6.2%	+2.2%
ΔP_T	bar	3.99		0.38	-91.9%	+0.0%

Figure 4.38: Co-current PI response using IMC Tuning (Case 4).

4.3.4   Optimal PI Tuning Parameters for Case 4

As both the IMC tuning parameters and the optimal tuning parameters were inadequate in controlling Case 4, dynamic optimization was used to identify a set of detuned tuning parameters that would result in a stable system response for the 50% reduction in gasifier flow rate (M_S^{in}).

For this optimization, at time $t = 0$, a -50% step in M_S^{in} is implemented, and the window for optimization is set at one hour, which represents the longest acceptable time frame for returning the CVs to set point. In addition to using IAE, two additional performance met-

rics were explored to obtain improved minimization of the T_{gas} deviation from set point: integral squared error (ISE) and integral time absolute error (ITAE). These are defined as:

$$ISE(t) = \int_0^t \left(\frac{|CV(t) - SP(t)|}{SP(t)} \right)^2 dt \qquad (4.9)$$

$$ITAE(t) = \int_0^t t \cdot \left(\frac{|CV(t) - SP(t)|}{SP(t)} \right) dt \qquad (4.10)$$

The bounds for these optimizations are the same as those defined in equations (4.4) – (4.6), and listed in Table 4.9. As the purpose of this optimization is to obtain optimal de-tuned parameters for Case 4, the following analysis is restricted solely to this case. The tuning parameters obtained from the different objective functions are shown in Table 4.17. The comparison of trajectories is shown in Figure 4.39.

Table 4.17: PI tuning parameters from the different objective functions for Case 4.

	T_{gas}		y_{CH_4}	
Objective Fn.	K_C	τ_I	K_C	τ_I
IAE	-95.4	410.3	-41.9	3.974
ISE	-183.0	765.2	-35.6	3.345
ITAE	-55.3	267.5	-38.3	3.681
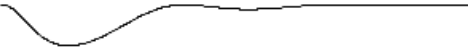
Disturbance Variable						
Variable	**Units**	**Initial**	**Trend (3600 second span)**	**Final**	**Min %**	**Max %**
M_S^{in}	t/h	237.43		118.71	-50.0%	+0.0%
Controlled Variable T_{gas}						
Objective	**Units**	**Initial**	**Trend (3600 second span)**	**Final**	**Max Dev**	**IAE**
IAE	K	1172.78		1172.39	-53.84	37.30
ISE	K	1172.78		1178.42	-43.61	40.32
ITAE	K	1172.78		1172.74	-61.10	40.78

Figure 4.39: Comparison of optimal detuned PI tuning parameters for Case 4 (co-current).

As seen in Figure 4.39, only the tuning parameters obtained from the IAE and ITAE objective functions were able to return T_{gas} to within ±1 K of the set point within one hour,

with settling times of 3,450 and 2,475 seconds respectively. The ISE tuning for Case 4 resulted in persistent oscillation of the states well beyond the one hour timeframe. While all three tunings show general improvement over the IMC case, the maximum deviation of T_{gas} from set point is still excessive. Temperatures for the tube wall and catalyst core throughout the system still exhibit sizeable fluctuations of 50 to 90 K, which is undesirable. It was observed that feedback-PI control is inadequate in rejecting this magnitude of disturbance for the co-current design.

4.3.5   Optimal PID Tuning Parameters for Case 4

The option of implementing PID control has not been explored thus far, generally due to the stigma associated with its implementation in the industry. Control engineers typically avoid PID control unless absolutely necessary, due to the increased difficulty of tuning compared to PI and its tendency to prescribe excessive MV movement in the presence of measurement noise. However derivative action may yield benefit for processes that are second-order, such as T_{gas} for the co-current design.

As with the previous section, it is desired to obtain the optimal tuning parameters for Case 4, now adding τ_D as one of the decision variables to the temperature controller. IAE was used in the objective function for both controllers, with a μ of 0.5 and a time horizon of one hour. The -50% step in M_S^{in} was implemented at time $t = 0$. Table 4.18 shows the resulting tuning parameters.

Table 4.18: PID tuning parameters from minimizing IAE for Case 4.

T_{gas}			y_{CH_4}		
K_C	τ_I	τ_D	K_C	τ_I	τ_D
-114.6	276.7	8.4	-58.7	6.3	0.0
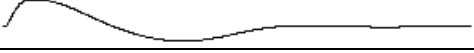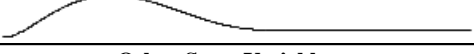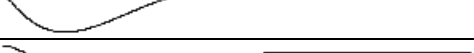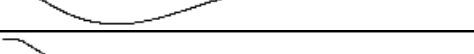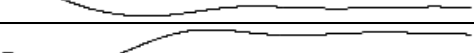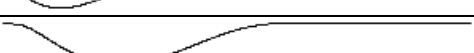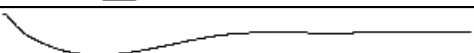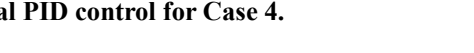
Disturbance Variable						
Variable	**Units**	**Initial**	**Trend (2000 second span)**	**Final**	**Min %**	**Max %**
M_S^{in}	t/h	237.43		118.71	-50.0%	+0.0%
Controlled Variables						
Variable	**Units**	**Initial**	**Trend (2000 second span)**	**Final**	**Max Dev**	**IAE**
T_{gas}	K	1172.78		1173.63	-40.28	21.02
y_{CH4}	mol %	3.58		3.58	+0.05	6.78
Manipulated Variables						
Variable	**Units**	**Initial**	**Trend (2000 second span)**	**Final**	**Min %**	**Max %**
F_{SMR}	kmol/hr	21.50		11.84	-46.2%	+0.0%
$R_{S/C}$	mol/mol	3.33		3.52	+0.0%	+35.9%
Other State Variables						
Variable	**Units**	**Initial**	**Trend (2000 second span)**	**Final**	**Min %**	**Max %**
$T_{W|z=0}$	K	1214.28		1260.89	-1.3%	+4.5%
$T_{W|z=0.5L}$	K	1165.86		1168.82	-4.3%	+0.8%
$T_{W|z=L}$	K	1182.62		1174.95	-4.0%	+0.0%
$T_{cat|z=0}$	K	776.33		772.56	-0.6%	+0.0%
$T_{cat|z=0.5L}$	K	1113.59		1144.80	-2.6%	+3.5%
$T_{cat|z=L}$	K	1172.58		1173.75	-3.4%	+0.1%
T_S^{out}	K	1206.57		1176.44	-5.4%	+0.0%
ΔP_T	bar	3.99		1.19	-71.6%	+0.0%

Figure 4.40: Co-current optimal PID control for Case 4.

Implementation of this PID tuning for Case 4 is illustrated in Figure 4.40. The maximum deviation of T_{gas} from set point is -40.3 K, a modest improvement from the detuned PI cases (Figure 4.39). Settling times are 1,964 seconds for T_{gas} and 1,020 seconds for y_{CH_4}, which are reduced from the detuned PI cases. Catalyst core and tube wall temperatures also exhibit decreased transient variation between 40 and 70 K, which is improved from the PI cases, but still unsatisfactory. The results obtained show that, even with derivative action implemented, feedback control is inadequate at maintaining satisfactory performance when subjected to a severe gasifier flow rate disturbance.

4.3.6   Implementation of Feedforward for Disturbance Rejection (Case 4)

It has been adequately demonstrated that the shell gas flow rate disturbance has an enormous effect on the co-current system. The explored control strategies have been largely unable to maintain system stability in the face of a large drop in the shell gas flow rate. The adopted strategies thus far aimed to maintain control within the RSC without any knowledge of gasifier operation. It has been shown that some knowledge may be necessary for the co-current system to maintain acceptable operation for extreme disturbance cases.

Since the control of case 4 has proven to be exceptionally difficult, a feed forward control scheme was developed. Marlin (2000) mentions that feedforward control should only be explored when feedback control is inadequate. For this strategy, it is assumed that a measurement of the gasifier flow rate is available. Within an industrial gasifier, it is unlikely that the gasifier syngas flow rate can be directly measured upon entering the RSC, but this information can be inferred from the measureable coal-slurry and O_2 feeds, upstream of the gasifier. The block diagram in Figure 4.41 illustrates the principle of feedforward control. Note that removal of the $G_{ff}(s)$ block reduces the block diagram of Figure 4.41 to the feedback control loop previously discussed.
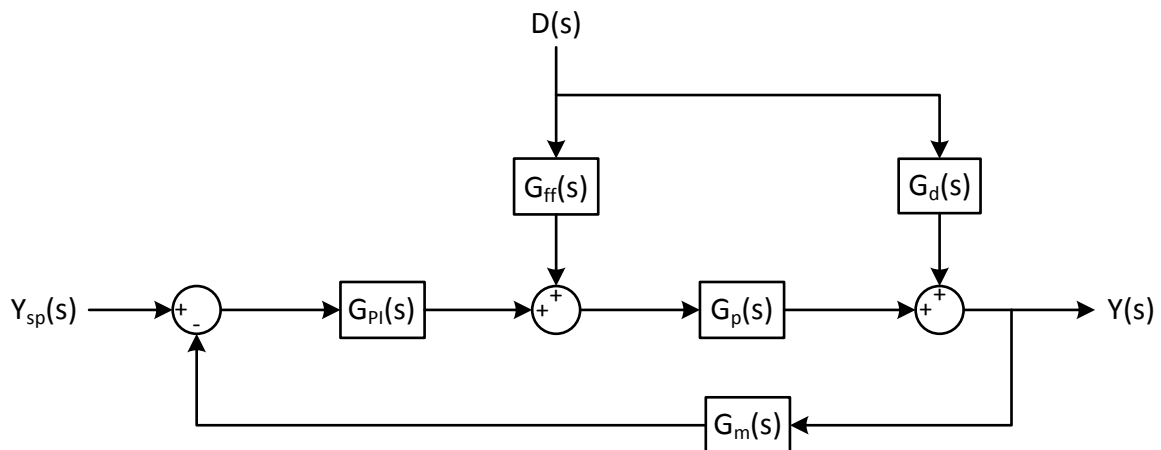
Figure 4.41: Block diagram illustrating feedforward concept.

Here, it can be seen that the output $Y(s)$ $[T_{gas}]$ is affected by the input $U(s)$ $[F_{SMR}]$ and the disturbance $D(s)$ $[M_S^{in}]$. The output is determined as:

$$Y(s) = D(s)G_d(s) + U(s)G_p(s),$$
<div align="right">(4.11)</div>

where $G_d(s)$ and $G_p(s)$ are the disturbance and process transfer functions respectively. It is desired to maintain $Y(s)$ at zero, meaning that the output is at set point. The input required for this is determined as:

$$U(s) = -D(s)\left(\frac{G_d(s)}{G_p(s)}\right)$$
<div align="right">(4.12)</div>

The feedforward controller is thus a function of the process and disturbance transfer functions:

$$G_{ff}(s) = \frac{G_d(s)}{G_p(s)} = -\frac{\dfrac{K_d e^{-\theta_d s}}{\tau_d s + 1}}{\dfrac{K_p e^{-\theta_p s}}{\tau_p s + 1}} \rightarrow G_{ff}(s) = -\frac{K_d}{K_p}\frac{\tau_p s + 1}{\tau_d s + 1}e^{-(\theta_d - \theta_p)s}$$
<div align="right">(4.13)</div>

The $G_p(s)$ transfer function is the effect of the input F_{SMR} on output T_{gas}, and was previously determined in Section 4.2.1. The effect of $G_d(s)$ was determined by performing an open loop step test of -10% in M_S^{in}, with the results illustrated in Figure 4.42. The process parameters obtained to derive the feedforward controller are listed in Table 4.19.

Table 4.19: Process parameters required for the development of the feedforward controller.

K_d	τ_d	θ_d	K_p	τ_p	θ_d
0.000809	196	1	-0.01059	195	1
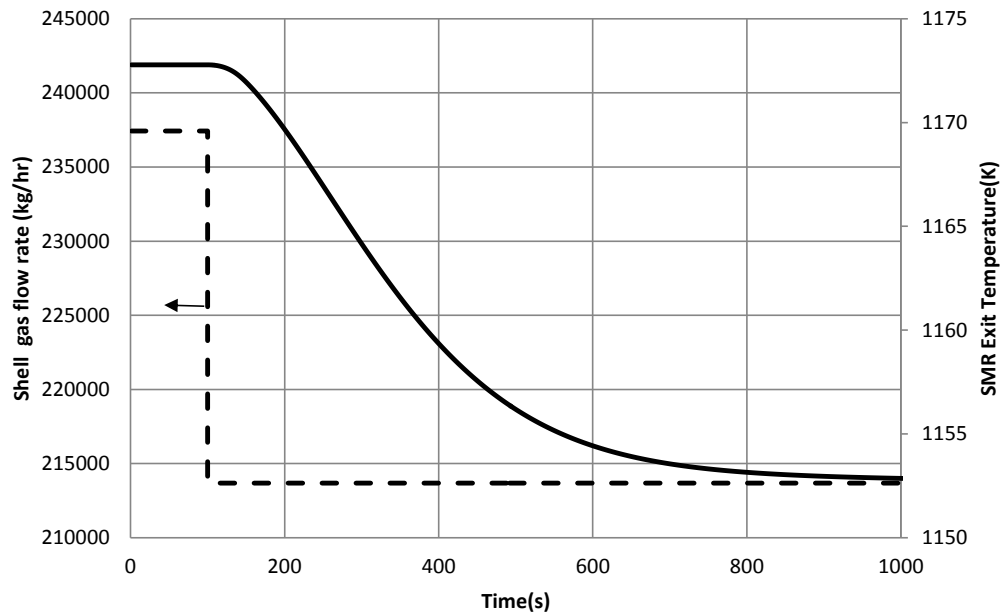
Figure 4.42: Open loop step test of disturbance shell mass flow rate (M_S^{in}) on T_{gas}.

Due to the similarity in the process dynamics between the process and disturbance transfer functions, a steady-state version of the feedforward controller can be used, which is simpler to implement. Marlin (2000) mentions that this simplification does not result in significant degradation in control performance. It is expected that the dynamics of the process and disturbance transfer functions are similar, as the effect of both inputs (F_{SMR} and F_S^{in}) travel the same length of the RSC to affect the output (T_{gas}). The steady-state feedforward reduces to:

$$G_{ff} = -\frac{K_d}{K_p} \qquad (4.14)$$
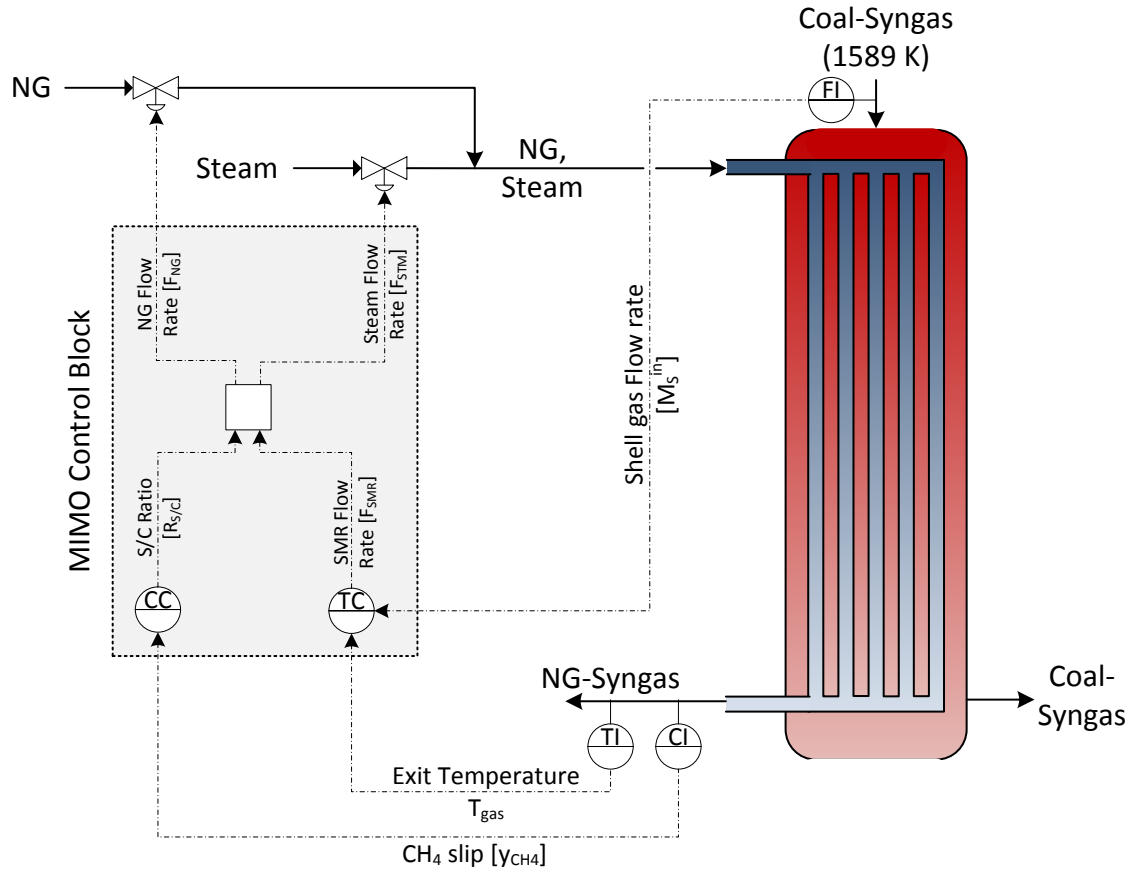
Figure 4.43: Control design illustration for co-current case with feedforward/feedback.

The feedforward controller was added to feedback control for the temperature loop (Figure 4.43). The feedforward/feedback controller was tested using the extreme disturbance case (Case 4). Using a detuned temperature controller, the result is slightly oscillatory, but overall stable (Figure 4.44). IAE for the temperature loop is reduced by 83.2% compared to the IMC feedback control performance. The peak tube wall temperature ($T_{W|z=0}$) during the transient is 1,268.6 K, which is considerably reduced from feedback-only results for Case 4. Catalyst core and tube wall temperatures, though oscillatory, do not exhibit the catastrophic variations seen in previous cases. The optimal tuning parameters determined for feedback PI control are still too aggressive for this disturbance, and result in persistent oscillation in the composition controller, as shown in Figure 4.45. This

highlights the tremendous difficulty in controlling this particular case with the co-current design, and shows why a detuned controller was needed.
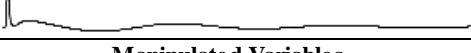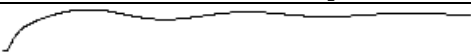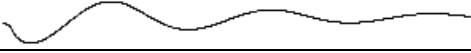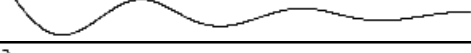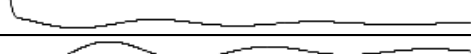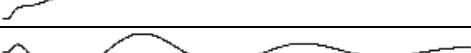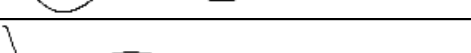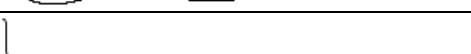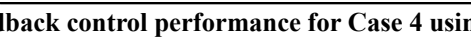
Disturbance Variable						
Variable	**Units**	**Initial**	**Trend (3600 second span)**	**Final**	**Min %**	**Max %**
M_S^{in}	t/h	237.43		118.71	-50.0%	+0.0%
Controlled Variables						
Variable	**Units**	**Initial**	**Trend (3600 second span)**	**Final**	**Max Dev**	**IAE**
T_{gas}	K	1172.78		1174.00	-8.48	8.61
y_{CH4}	mol %	3.58		3.59	+0.28	14.26
Manipulated Variables						
Variable	**Units**	**Initial**	**Trend (3600 second span)**	**Final**	**Min %**	**Max %**
F_{SMR}	kmol/hr	21.50		11.90	-47.8%	+0.0%
$R_{S/C}$	mol/mol	3.33		3.51	+0.0%	+12.1%
Other State Variables						
Variable	**Units**	**Initial**	**Trend (3600 second span)**	**Final**	**Min %**	**Max %**
$T_{W|z=0}$	K	1214.28		1260.92	-0.1%	+4.5%
$T_{W|z=0.5L}$	K	1165.86		1169.68	-1.0%	+1.1%
$T_{W|z=L}$	K	1182.62		1175.22	-1.4%	+0.0%
$T_{cat|z=0}$	K	776.33		772.58	-0.6%	+0.0%
$T_{cat|z=0.5L}$	K	1113.59		1145.89	-0.0%	+3.8%
$T_{cat|z=L}$	K	1172.58		1174.04	-0.7%	+0.6%
T_S^{out}	K	1206.57		1176.72	-3.1%	+0.0%
ΔP_T	bar	3.99		1.20	-73.2%	+0.0%

Figure 4.44: Feedforward/Feedback control performance for Case 4 using detuned IMC tuning.
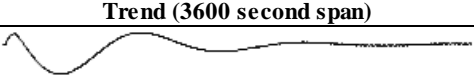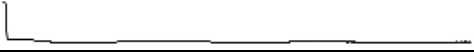
Disturbance Variable						
Variable	**Units**	**Initial**	**Trend (3600 second span)**	**Final**	**Min %**	**Max %**
M_S^{in}	t/h	237.43		118.71	-50.0%	+0.0%
Controlled Variables						
Variable	**Units**	**Initial**	**Trend (3600 second span)**	**Final**	**Max Dev**	**IAE**
T_{gas}	K	1172.78		1172.80	-8.43	5.25
y_{CH4}	mol %	3.58		3.98	+1.24	330.04
Manipulated Variables						
Variable	**Units**	**Initial**	**Trend (3600 second span)**	**Final**	**Min %**	**Max %**
F_{SMR}	kmol/hr	21.50		11.84	-46.2%	+0.0%
$R_{S/C}$	mol/mol	3.33		4.37	-14.1%	+32.1%

Figure 4.45: Feedforward/Feedback control performance for Case 4 using ITAE optimal tuning parameters.

4.4   Chapter Summary

This chapter focused on the development of a base case design and control structure for the counter-current and co-current RSC/SMR systems. A suitable base case design was established for implementation in an existing GE-Texaco gasifier under similar operating conditions, whilst obtaining 85% CH_4 conversion in the SMR tubes and satisfying temperature and pressure constraints. The counter-current design provided superior cooling duty and greater NG throughput than the co-current design, at the expense of elevated maximum tube wall temperatures far above those seen in conventional SMR systems. The co-current design provides safer tube wall temperatures which will prolong tube life, but at the expense of loss of thermal efficiency.

A multi-loop PI control structure was developed for both systems, whereby taking process interactions into consideration, SMR flow rate (F_{SMR}) was used to control tube gas exit temperature (T_{gas}), and S/C ratio ($R_{S/C}$) was used to control CH_4 slip (y_{CH_4}). Open-loop step tests were performed to identify the process transfer functions and derive controller tunings. Of the conventional tuning rules, IMC tuned parameters provided far more robust control, relative to Z-N and C-C tuning. For the set point change and moderate disturbance scenarios explored, IMC tuned controllers provided satisfactory performance in both

the co-current and counter-current systems. Significant improvements in performance were realized for both systems upon using dynamic optimization to identify optimal controller tunings.

Taking the difficulty of gasifier operation into account, the control systems were also tested against a severe 50% reduction in gasifier flow rate. While the counter-current feedback PI control system effortlessly rejected this disturbance, the co-current response was catastrophically unstable. However, with implementation of feedforward control using measurement of the gasifier flow rate (M_S^{in}), the co-current design can handle the severe disturbance, yielding a more stable system response.

While the counter-current feedback PI control system is extremely robust, it was found that the maximum tube wall temperature during transients came within 50 K of the absolute tube-wall temperature limit, which could result in premature tube failure. For the co-current RSC/SMR system, despite the more desirable tube wall temperature profiles, feedback-PI is less robust, on account of process interactions and heightened sensitivity to gasifier flow rate fluctuations; this drawback can be rectified by adding feedforward control, or by implementing a model based controller.

Chapter 5

Digital and Model Predictive Control

The control study performed in Chapter 4 showed several desirable characteristics for the co-current RSC/SMR System: namely that PI control was able to achieve system stability, acceptable responses for set point changes, reliable disturbance rejection, and an ability to maintain tube wall temperatures well below their maximum limits. However, controller interactions were quite significant, and the continuous control that was implemented represents an idealized case which does not take into account hardware limitations of measurement devices. With the knowledge that feedback can be used to stabilize the system, the effect of reducing measurement and control action frequency of that feedback needs to be explored. This situation naturally lends itself to the opportunity of developing a Model Predictive Controller (MPC), which will be compared with the multi-loop PI design to assess performance improvements for a fixed sample time. While only the co-current case is explored in the following chapter, the dynamics of the counter-current system were much more favourable (faster settling times, less oscillatory); hence the following general discussion focuses on the co-current design as a "worst case".

5.1   Implementation of Digital PI Control

5.1.1   Digital PI Model and Implementation

The control results of Chapter 4 should be considered as the PI feedback response theoretically achievable due to the continuous signals received by the controllers. In reality, however, the hardware that is utilized to obtain process measurements must invariably take time to process the sample and send a measurement signal to the controller. With increasing sampling frequency (decreasing sampling time), the digital PI control performance tends toward continuous PI control. Considering the CVs defined for this system (Table 5.1), the CH_4 slip control is most likely to suffer from long sampling times.

Table 5.1: CVs and MVs considered in PI and MPC design.

	Variable	Description
CV_1	T_{gas}	Exit temperature of SMR tube gas
CV_2	y_{CH_4}	Exit CH_4 slip of SMR tube gas
MV_1	F_{SMR}	Total feed flow to SMR tube ($F_{NG} + F_{STM}$)
MV_2	$R_{S/C}$	S/C ratio of SMR feed

The problem is two-fold: firstly, the dynamics of y_{CH_4} ($\tau_p \approx 10$ seconds) are significantly faster than the T_{gas} dynamics ($\tau_p \approx 200$ seconds), where τ_P represents the time taken for the CV to complete 63.2% of its step-response trajectory; secondly, CH_4 slip (y_{CH_4}) requires a composition analyzer to measure, which can suffer from long sample times relative to common temperature sensors (Marlin, 2000). As an example, one particular composition analyzer vendor offers a product specifically tailored to industrial NG and syngas applications (Precisive LLC, 2013). The Precisive analyzer feedback frequency can be user-adjusted between one second and five minutes, with longer sample times corresponding to higher measurement accuracy.

The digital PI controller model differs from the continuous PI controller form; the full position version was used in this work (Marlin, 2000):

$$MV_k = Bias + K_C[E_k + \frac{\Delta t}{\tau_I} S_k] \tag{5.1}$$

$$S_k = \sum_{i=1}^{k} E_i = E_k + S_{k-1} \tag{5.2}$$

$$E_i = SP_i - CV_i, \tag{5.3}$$

where K_C and τ_I are the tuning parameters, E_i is the ith sampled error, k is the current sample, Δt is sampling time, and S_k represents the summation of past and present errors (analogous to integrating the error in continuous time). As it is not possible to implement a discrete model explicitly within gPROMS (all equations are inherently continuous), the act of sampling and determining the next controller move takes place within a Task (Process Systems Enterprise, 2011). A Task is used in gPROMS to specify an operating procedure, which in this case (see Figure 5.1 for description) is periodic and constitutes: 1) sampling the CV, 2) implementing a new control action (MV) and 3) maintaining that MV for the controller sample time.

```
WHILE Time < EndTime DO
  SEQUENCE
    REASSIGN
      WITHIN Controller DO
        Error := OLD(SP - CV) ;
        Integral_Error := OLD(Integral_Error) + OLD(Error) ;
        MV := OLD(Bias + Gain * ( Error + (Ts/tau_I)*Integral_Error )) ;
      END
    END
    CONTINUE FOR Controller.Ts
  END
END
```

Figure 5.1: Discrete PI TASK implementation in gPROMS.

This discrete sampling imposes a zero-order-hold (ZOH) on the process measurement. The continuous time signal of the process can be perfectly reconstructed from the discrete measurements, albeit with a phase lag of $\Delta t/2$ from the original signal. As a result, the continuous time tuning parameters must be detuned to account for this phase lag by incorporating the $\Delta t/2$ term into the process dead-time (θ_d). Subsequent simulation tests

use the IMC tunings listed in Table 5.2, based on the process parameters of Table 4.14 and tuning rules in Table 4.7.

Table 5.2: Process and tuning parameters for continuous and discrete PI control (co-current).

	Continuous		$\Delta t = 10\ sec$		$\Delta t = 30\ sec$	
	K_C	τ_I	K_C	τ_I	K_C	τ_I
T_{gas}	-94.0	195.0	-91.6	195.0	-87.3	195.0
y_{CH_4}	-23.6	10.2	-17.1	10.2	-11.0	10.2

The performance of two different sample time (Δt) choices was investigated. A sample time of ten seconds was chosen to represent the case where $\Delta t < \tau_{p,y_{CH_4}}$. A 'slower' sample time of thirty seconds was also investigated to represent the case where limitations of the analyzer-feedback result in $\Delta t > \tau_{p,y_{CH_4}}$. The performance of these two discrete cases relative to continuous PI control is demonstrated in the following section.

5.1.2   Discrete PI Results

Several scenarios are selected from those described in Section 4.2.4 to illustrate the significance of incorporating sample time on set point tracking and disturbance rejection.

Case 0a: + 1 percentage point step in y_{CH_4} set point

For a step change in the y_{CH_4} set point, the ten-second PI control performance overall is only slightly worse than the continuous case (see Figure 5.2). The return of T_{gas} to set point follows roughly the same dynamics as the continuous controller. In the case of y_{CH_4}, a small initial overshoot is quickly corrected to have the CV effectively settled in under two minutes. However, the reduced rate of feedback is detrimental to the thirty-second PI control performance. The composition control in this case is ineffective in meeting the new set point, and destabilizes both controllers in the process. This adverse effect high-

lights the importance of obtaining sufficiently frequent measurements to ensure system stability under digital multi-loop PI control.
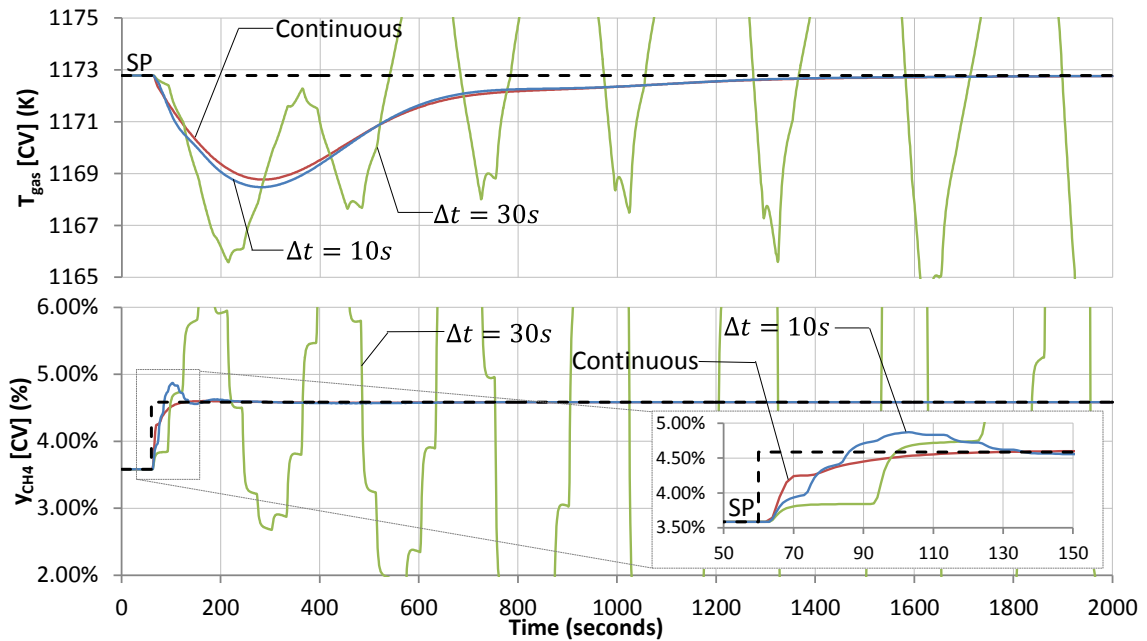
Figure 5.2: Comparison of continuous and discrete PI (ten and thirty second sampling) control for case 0a (+ 1 percentage point step in y_{CH_4} set point).

Case 0b: - 10 K step in T_{gas} set point

For this case (presented in Figure 5.3), unlike in Chapter 4, the T_{Gas} set point change is represented as a step instead of a ramp in order to obtain a fairer comparison across different sampling times. Increasing the sample time causes minor deterioration in temperature control. The effect of discrete sampling is much more evident in the composition control, where using a sample time of thirty seconds results in oscillation in y_{CH_4} that decays at a much slower rate than with the continuous and ten second controllers. The y_{CH_4} CV appears to eventually approach the set point, but this would occur well beyond the simulated 2,000 second window. Such sustained oscillation is unacceptable.
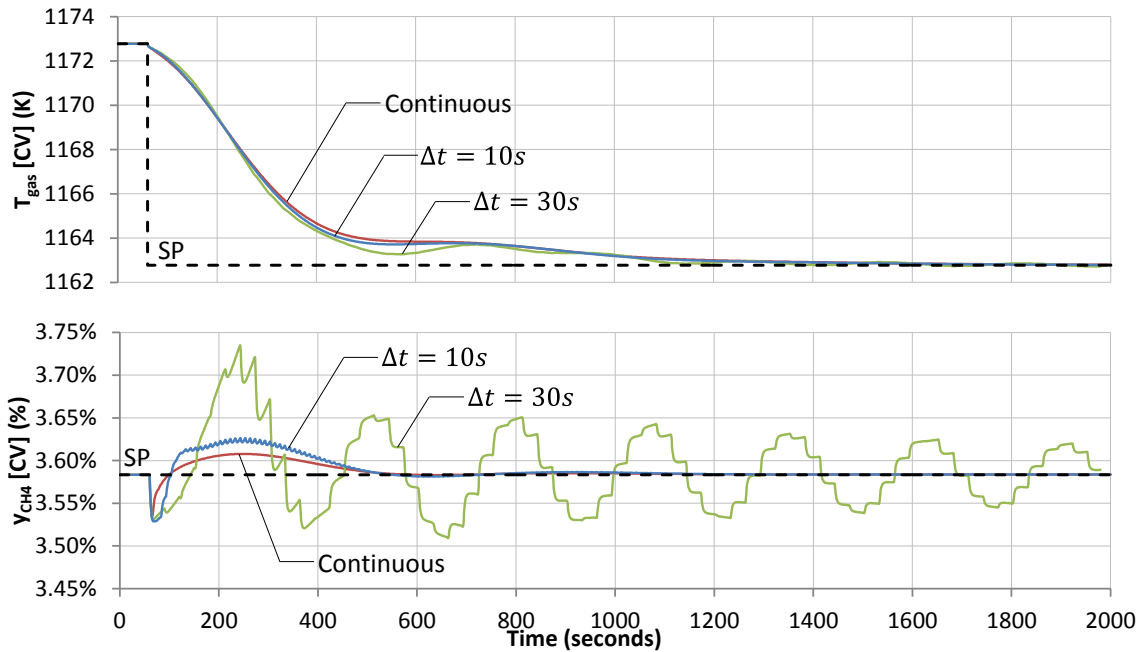
Figure 5.3: Comparison of continuous and discrete PI (10 and 30 second sampling) control for Case 0b (-10 K step in T_{gas} set point).

Case 3b: 10% reduction in gasifier flow rate (M_S^{in})

For this disturbance scenario (Figure 5.4), all continuous and discrete controllers were able to successfully reject the disturbance effect on T_{gas}. Increasing the sample time results in a larger maximum deviation of T_{gas} from its set point, and more pronounced oscillations. For the control of y_{CH_4}, as was observed in Case 0b, the amplitude of the deviation increases significantly with increasing sample times, with the thirty-second PI control not being able to settle the CV within the simulated time frame.
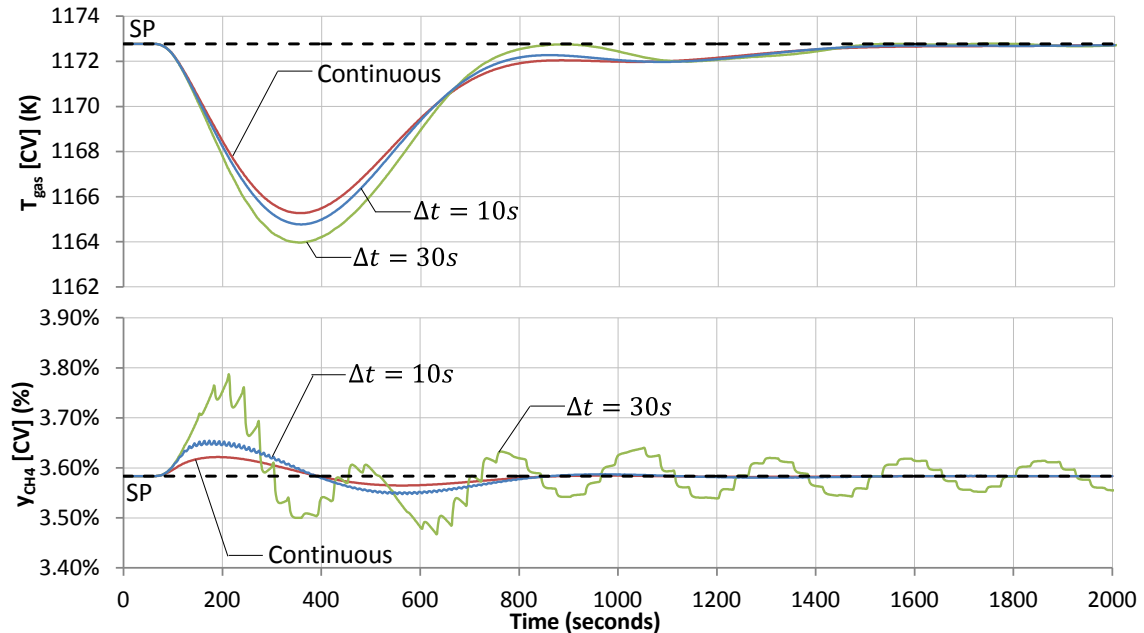
Figure 5.4: Comparison of continuous and discrete PI (ten and thirty second sampling) control for Case 3b (10% reduction in gasifier flow rate).

As seen in the investigated cases, while the temperature control performance does not degrade significantly by increasing sampling time to thirty seconds, composition control performance exhibits substantial deterioration. With a thirty-second sample time, the PI multi-loop scheme destabilizes the plant for set point changes in composition, even with controller detuning. As such, for the control objectives considered, employing a feedback PI control strategy is inadequate for a sample time of more than ten seconds. These observations promote the need for a more effective method of control to overcome the impact of discrete sampling on the overall stability of the controlled system.

5.2   Implementation of Offset-Free Model Predictive Control

To obtain improved control performance of the co-current RSC/SMR system in the face of discrete sampling and process interactions, an MPC controller was developed. Having knowledge of the plant dynamics captured within a model predictive framework is expected to yield improved performance relative to PI control. To capture important dynam-

ics in the coal-derived syngas, tube-gas, catalyst, tube wall and refractory wall phases, the number of time-varying states resulting from spatial discretization for the non-linear plant model is in excess of 60,000 variables. Such a model cannot be used as a control model for MPC purposes; a reduction of the model order is necessary. In addition, the vast majority of the states, such as catalyst core temperatures and partial pressures, are not directly measurable. The common practice in this situation is to assume a rigorous non-linear model as the plant (Sanandaji et al., 2011; Wallace et al., 2012), and to develop a data-driven model (typically linear) from plant simulations, with which to implement model-based control techniques.

Within this section, a linear data-driven model is developed in order to implement an MPC controller and interface it with the plant model. While it is desired to characterize the majority of the important non-linear dynamics with the linear model, there will invariably be some degree of offset (plant-model mismatch) due to loss of accuracy. To this end, an offset-free mechanism equipped with a Luenberger observer is used to modify the linear model and eliminate the plant-model mismatch. The principles of this mechanism are discussed in Section 5.2.1. Following this, the MPC is described in Section 5.2.3, with an analysis of the MPC results provided in Section 5.3.

5.2.1   Offset-Free Mechanism (Observer Design)

In an effort to correct any potential plant-model mismatch, the mechanism described by Wallace et al. (2012) was adopted in this work. To motivate the purpose of implementing an offset-free mechanism, one must first look at what the reduced linear model is trying to represent and achieve. The plant model developed and described in Chapter 3 and (Ghouse et al., 2014), and simulated in Chapter 4, can be characterized by the general non-linear representation:

$$\dot{x}_{NL} = f(x_{NL}) + g(x_{NL})u \tag{5.4}$$

$$y_{NL} = h(x_{NL}), \tag{5.5}$$

where $\boldsymbol{x} \in \mathbb{R}^n, \boldsymbol{u} \in \mathbb{R}^m, \boldsymbol{y} \in \mathbb{R}^l$ are the vectors of the model states, inputs and measured outputs respectively. In the following analysis and MPC implementation, the measured outputs are T_{gas} and y_{CH_4}, thus $\boldsymbol{y} \in \mathbb{R}^2$. For model-based control, it is desired to approximate this system using a linear model, derived from system identification methods, of the general form:

$$\dot{\boldsymbol{x}}_L = A\boldsymbol{x}_L + B\boldsymbol{u} \tag{5.6}$$

$$\boldsymbol{y}_L = C\boldsymbol{x}_L, \tag{5.7}$$

where A, B and C are coefficient matrices that describe the linearized dynamics of the system. The linear model is developed around the same nominal operating point of the non-linear model; that is to say, the origin of both models should correspond to each other:

$$\dot{\boldsymbol{x}}_{NL} = 0|_{x_{NL}=0,\boldsymbol{u}=0} \tag{5.8}$$

$$\dot{\boldsymbol{x}}_L = 0|_{x_L=0,\boldsymbol{u}=0}. \tag{5.9}$$

At this particular operating point, there is zero offset seen between the linear model and the non-linear plant model, that is to say: $\boldsymbol{x}_L^0 = \boldsymbol{x}_{NL}^0$. Suppose now, that the same step input ($\boldsymbol{u}_{step}$) is applied to both models. If the linear and non-linear models were allowed to reach a new steady-state, the result derived from (5.4) and (5.6) would be:

$$0 = f(\boldsymbol{x}_{NL}^{ss}) + g(\boldsymbol{x}_L^{ss})\boldsymbol{u}_{step} \tag{5.10}$$

$$0 = A\boldsymbol{x}_L^{ss} + B\boldsymbol{u}_{step} \quad \rightarrow \quad \boldsymbol{x}_L^{ss} = -A^{-1}B\boldsymbol{u}_{step}. \tag{5.11}$$

Unlike the steady-state at the origin, the results from the two models will not be the same at the new steady-state (i.e.: $\boldsymbol{x}_L^{ss} \neq \boldsymbol{x}_{NL}^{ss}$). This difference is referred to as plant-model mismatch, and arises from the linear model being unable to capture all of the dynamics and interactions of the plant. This plant-model mismatch may be captured and described as a 'fictitious state', designated as θ, which is estimated using the difference between the outputs of the linear and non-linear models. As the objective is to eliminate plant-model

mismatch of the two measured outputs, $\boldsymbol{\theta} \in \mathbb{R}^2$. To incorporate $\boldsymbol{\theta}$ into the identified linear model of equations (5.5)and (5.6) yields an augmented model of the form:

$$\begin{bmatrix} \dot{x} \\ \dot{\boldsymbol{\theta}} \end{bmatrix} = \begin{bmatrix} A & G_\theta \\ 0 & 0 \end{bmatrix} \begin{bmatrix} x_L \\ \boldsymbol{\theta} \end{bmatrix} + \begin{bmatrix} B \\ 0 \end{bmatrix} u \tag{5.12}$$

$$y_L = \begin{bmatrix} C & 0 \end{bmatrix} \begin{bmatrix} x_L \\ \boldsymbol{\theta} \end{bmatrix}. \tag{5.13}$$

Note that the in the above expression, $\boldsymbol{\theta}$ is assumed to not be a function of time, and is not directly influenced by the inputs or states. The discrete implementation of the augmented linear model becomes:

$$\begin{bmatrix} \mathbf{x}(k+1) \\ \boldsymbol{\theta}(k+1) \end{bmatrix} = \begin{bmatrix} A & G_\theta \\ 0 & I \end{bmatrix} \begin{bmatrix} \mathbf{x}(k) \\ \boldsymbol{\theta}(k) \end{bmatrix} + \begin{bmatrix} B \\ 0 \end{bmatrix} \mathbf{u}(k) \tag{5.14}$$

$$\mathbf{y}(k) = \begin{bmatrix} C & 0 \end{bmatrix} \begin{bmatrix} \mathbf{x}(k) \\ \boldsymbol{\theta}(k) \end{bmatrix}. \tag{5.15}$$

This discrete time augmented model can be compactly represented as:

$$\bar{\mathbf{x}}(k+1) = \bar{\mathbf{A}}\bar{\mathbf{x}}(k) + \bar{\mathbf{B}}\mathbf{u}(k) \tag{5.16}$$

$$\mathbf{y}(k) = \bar{\mathbf{C}}\bar{\mathbf{x}}(k), \tag{5.17}$$

where $\bar{\mathbf{A}} = \begin{bmatrix} A & G_\theta \\ 0 & I \end{bmatrix}, \bar{\mathbf{B}} = \begin{bmatrix} B \\ 0 \end{bmatrix}, \bar{\mathbf{C}} = \begin{bmatrix} C & 0 \end{bmatrix}$ and $\bar{\mathbf{x}} = \begin{bmatrix} \mathbf{x} \\ \boldsymbol{\theta} \end{bmatrix}$. Ideally, this augmented model represents the non-linear model. An observer is implemented to estimate the states as:

$$\hat{\bar{\mathbf{x}}}(k+1) = \bar{\mathbf{A}}\hat{\bar{\mathbf{x}}}(k) + \bar{\mathbf{B}}\mathbf{u}(k) + \mathbf{L}\left(\mathbf{y}_{NL}(k) - \bar{\mathbf{C}}\hat{\bar{\mathbf{x}}}(k)\right), \tag{5.18}$$

where the outputs of the observer are subtracted from the plant outputs, and multiplied by $\mathbf{L}$, known as the Luenberger observer gain matrix. The observer error can be denoted as:

$$\mathbf{e}(k+1) = \bar{\mathbf{x}}(k+1) - \hat{\bar{\mathbf{x}}}(k+1). \tag{5.19}$$

Through substitutions of equations (5.16) and (5.18) into (5.19), the error expression in (5.19) can be reduced to:

$$\mathbf{e}(k+1) = (\bar{\mathbf{A}} - \mathbf{L}\bar{\mathbf{C}})\mathbf{e}(k) \tag{5.20}$$

To drive the observer error to zero as k → ∞, the Luenberger observer poles must be chosen such that the expression $(\overline{A} - L\overline{C})$ has all eigenvalues within the unit circle. The observer can be made more aggressive by choosing poles closer to zero. However, due to interfacing the controller and observer with a non-linear model, choosing overly aggressive poles can lead to instability when the model is used in a closed-loop application.

G_θ and L are the primary tuning parameters associated with the dynamics of the θ states and their effect on the overall system. Wallace et al. (2012) suggest using the B matrix derived from the linear model as an initial guess for G_θ, treating the θ states as having the same dynamic effect on the system states as the inputs.

5.2.2   System Identification

The RSC/SMR model represents an infinite-dimensional system, requiring discretization to approximate the system states. The plant model in its full form is too cumbersome to be used for model-based control; to implement MPC, a reduced-order model must be developed. System identification is a black-box, data-driven modeling approach, mapping the inputs (F_{SMR} and $R_{S/C}$) to the outputs (T_{gas} and y_{CH_4}). Note that it is not possible to measure the inside of the RSC due to the hazardous conditions, and thus real-time monitoring at any point along the system with the exception of the gas streams at the exit is impossible. Two methods were investigated to obtain a linear model that can approximate the plant response well enough for model-based control, each discussed in turn.

Method 1: Variable step duration, fixed step size

The guidelines for this method are described in (Roffel and Betlem, 2004). Each input was moved independently while keeping the others fixed; the input was stepped in alternating directions at increasing pulse widths of 1/4, 1/3, 1/2, 2/3, 3/4, 4/4 and 5/4 of the time to steady-state (roughly 600 seconds for this system). For the MV F_{SMR}, the steps were switched between ± 10 kmol/hr from its nominal value (21.5 kmol/hr), while $R_{S/C}$

was switched between ± 2 of its nominal value (3.33 mol H_2O/mol CH_4). The results of this test are shown in Figure 5.5.
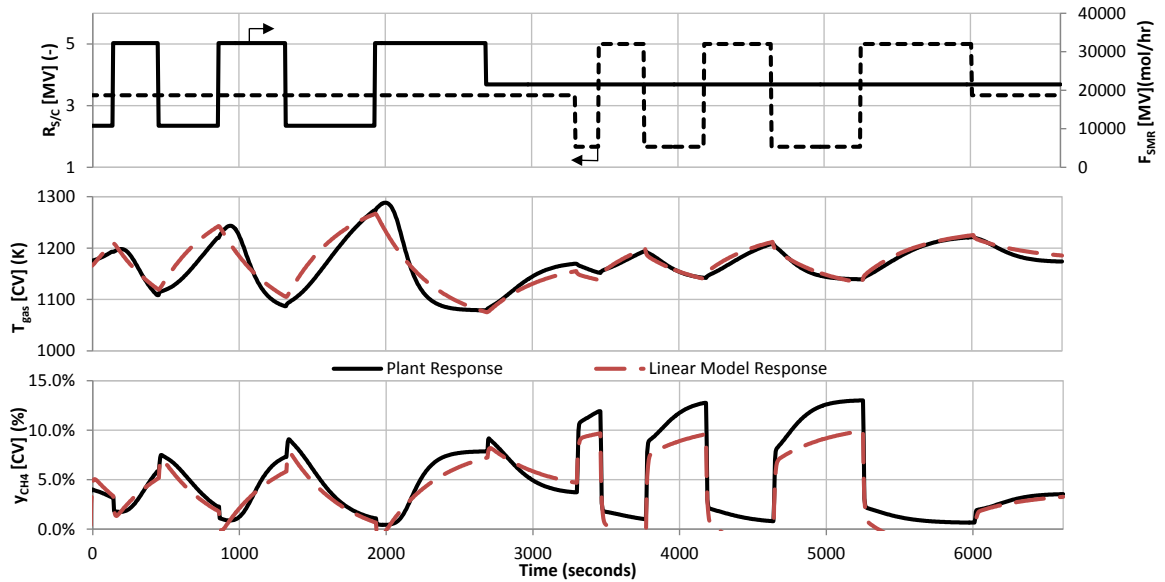
Figure 5.5: System identification test using Method A.

Method 2: Fixed step duration, variable step size.

For this method, the step duration was fixed at 1,200 seconds to ensure that all steady-states were captured, irrespective of the step magnitude. The inputs were subjected to a pseudo-random binary sequence (PRBS), multiplied with a random, appropriately scaled number, to generate variable step sizes for the inputs. F_{SMR} was allowed to move within ± 5 kmol/hr from the nominal steady state, while $R_{S/C}$ was allowed to move within ± 2 from steady-state. The results of this identification test are shown in Figure 5.6.
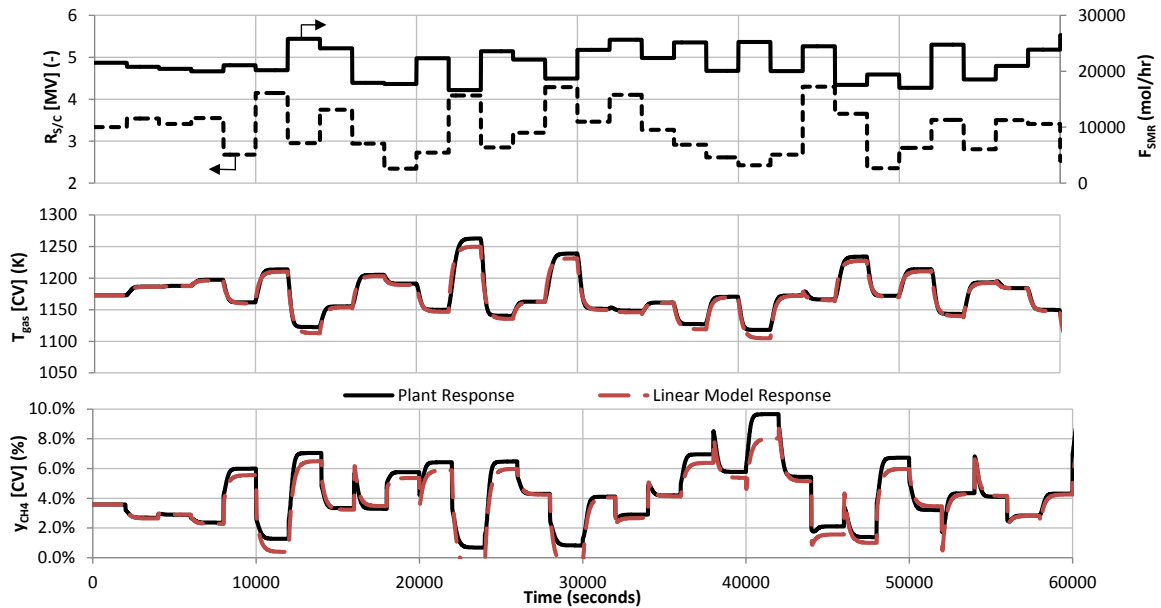
Figure 5.6: System Identification test using Method B.

Using the *System Identification Toolbox* in MATLAB, a linear state-space model was fit to the data for both identification methods. Using normalized root mean squared error (NRMSE), both methods yielded a fit to the data of about 63 - 77% (where 100% denotes zero error between the predictions and the measurements over the validation dataset). In particular, the sign of the gains for the identified models correctly matched those of the plant; however, the linear models tend to under-predict positive and over-predict negative changes in both outputs. Both methods predict a negative value for y_{CH_4} at instances where the actual CH_4 slip approaches zero, which is physically unrealizable, and represents an obvious shortcoming of using a single linear data-driven model to approximate a highly non-linear process. However, this condition never occurred in any of the applications of the linear model described in the following sections.

By augmenting the linear model with the $\boldsymbol{\theta}$ states and Luenberger observer, these deficiencies in the identified model should be negated. The model from methods A and B were compared by equipping them with the offset-eliminating mechanism and observer (tuned using the same observer poles) and subjecting to the same input step. The result of implementing a +2 kmol/hr step in F_{SMR} is shown in Figure 5.7.
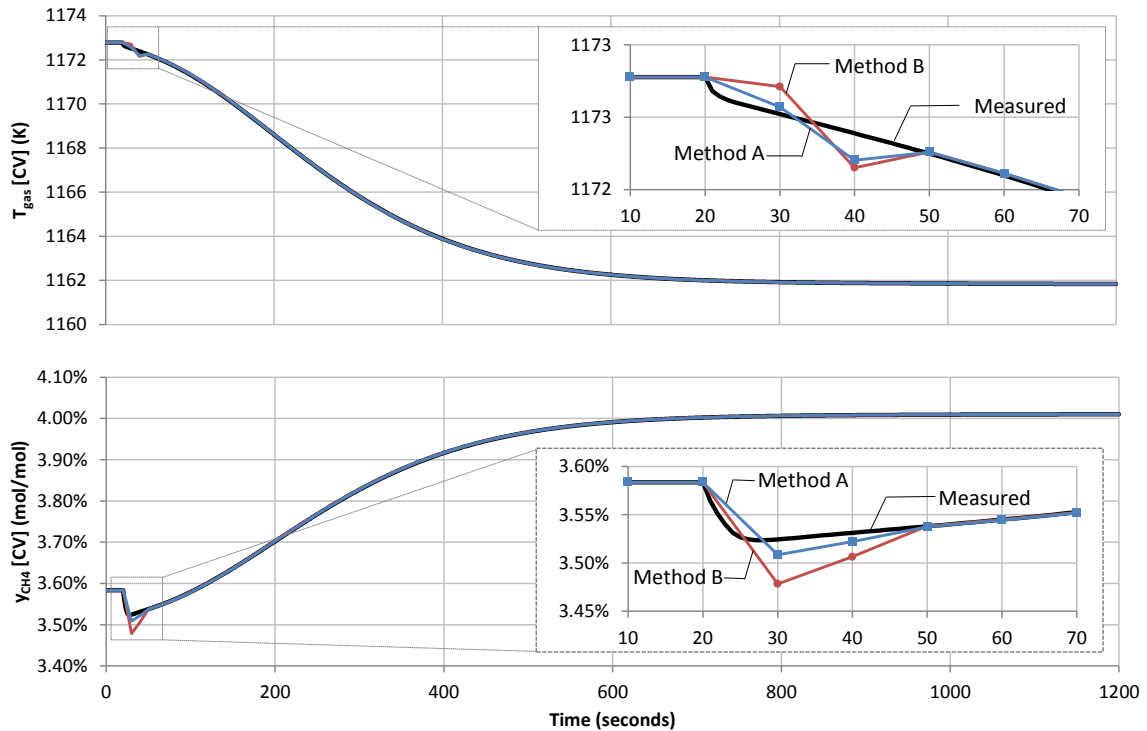
Figure 5.7: Comparison of identified linear models against non-linear plant output, for a +2 kmol/hr step change in F_{SMR} at $t = 60$ seconds. Both models are equipped with the offset eliminating mechanism. Sample time for both methods is ten seconds.

Both linear models quickly converge to the measured output, effectively matching it after three samples. However, as the end use for this augmented model is MPC (which demands input moves at every sampling instant), it is preferred to implement a model with less severe mismatch at the point of the input step (see inset of Figure 5.7). The increased severity of the mismatch 'kick' in method B's prediction would have an adverse effect on the stability of the MPC, where each significant input move would produce an initially large offset; the observer would thus have to be detuned, which reduces the speed of the offset-eliminating mechanism. Method A was selected for these reasons, and was found to produce more favourable results in the MPC controller testing stage relative to method B. The model coefficients for the identified model derived through method A are provided in Table 5.3.

Table 5.3: Linear model coefficients from identification method A.

Matrix	Value
A	$\begin{bmatrix} 1.020 & 97.734 \\ 4.0 \times 10^{-4} & 0.198 \end{bmatrix}$
B	$\begin{bmatrix} -0.207 & 3.404 \\ -0.001 & -0.021 \end{bmatrix}$
C	$\begin{bmatrix} 1 & 0 \\ 0 & 1 \end{bmatrix}$

5.2.3 OF-MPC development

The main criteria influencing the performance of an MPC controller (assuming a satisfactory model) are the objective function used for optimization and the controller tuning parameters. One of the advantages of MPC over conventional PI-control is the ability to tailor this objective function based on the requirements of the end user (a review of MPC formulations can be found in (Qin and Badgwell, 2003)). In this work, the MPC optimization problem was formulated in the standard manner to provide set point tracking and penalize excessive movement of the MVs. The objective function determined by the MPC controller is given by:

$$\min_{\Delta \mathbf{u}} \sum_{k=1}^{P} \left\| \hat{\mathbf{x}}(k+1) - \mathbf{x_{sp}}(k+1) \right\|_{\mathbf{Q}} + \sum_{k=1}^{N} \left\| \Delta \mathbf{u}(k) \right\|_{\mathbf{R}} \tag{5.21}$$

subject to:

$$\mathbf{u_{min}} \leq \mathbf{u}(k) \leq \mathbf{u_{max}} \tag{5.22}$$

$$\hat{\bar{\mathbf{x}}}(k+1) = \bar{\mathbf{A}}\hat{\bar{\mathbf{x}}}(k) + \bar{\mathbf{B}}u(k) \tag{5.23}$$

$$\text{where } \hat{\bar{\mathbf{x}}}(k)|_{k=1} = \begin{bmatrix} \mathbf{x}_k^0 & \boldsymbol{\theta}_k^0 \end{bmatrix}^\mathsf{T} \tag{5.24}$$

$$\hat{\bar{\mathbf{x}}}(k) = \begin{bmatrix} \hat{x}_1(k) & \hat{x}_2(k) & \hat{\theta}_1(k) & \hat{\theta}_2(k) \end{bmatrix}^\mathsf{T}, \tag{5.25}$$

where $\| \cdot \|_Q$ represents weighted norm, defined as $\|x\|_Q = x^T Q x$. $\mathbf{Q}$ and $\mathbf{R}$ are diagonal weighting matrices meant to penalize output and input deviations, respectively.

Guidelines for selecting MPC tuning parameters can be found in (Marlin, 2000; Roffel and Betlem, 2004; Seborg et al., 2010); the guidelines provided by Marlin were used for the MPC design of this study, with the tuning procedure by Wallace et al. (2012). used specifically for the tuning of the offset-eliminating mechanism. The following discussion briefly describes the experimentation employed with the various tuning parameters, which led to the choice of acceptable parameters as summarized in Table 5.4.

A challenging aspect of the MPC design for this system is the large difference in process time delay between the two outputs, with y_{CH_4} exhibiting significantly faster dynamics relative to T_{gas}. Based on the results of Section 5.1, the controller sampling time Δt was chosen as ten seconds to effectively control this fast output. Choosing $\Delta t > 10$ seconds results in 'drifting' of the fast output, which will be difficult to rectify by discrete control action. Also, it will become more difficult for the estimate to converge to the measured output during transients under increased sample times.

Due to the short sampling time, the prediction horizon (P) has to be large enough to be able to predict settling of the system; setting P = 100 was found to give good MPC performance. The control horizon N is usually chosen to be between one-fourth and one-third of the prediction horizon (Marlin, 2000), but was chosen to be N = 10 in this case to balance desired closed-loop performance and optimization computation time (average of 0.375 seconds per optimization solution using N = 10). Reducing N produced slightly slower control performance, with the system taking longer to settle after a disturbance. Increasing N was found to significantly increase optimization computation time, and occasionally produced erratic control movements that intensified plant-model mismatch.

As per the tuning guidelines in (Wallace et al., 2012), the observer tuning matrices G_θ and **L** were selected based on an assessment of open-loop performance (as discussed in Section 5.2.2). G_θ was chosen as the B matrix of the identified linear model (Table 5.3) and the observer poles were chosen to be aggressive, yielding the $[L_x \ L_\theta]^T$ matrix as shown in Table 5.4.

Tuning of the **Q** and **R** matrices proved especially difficult. In particular, **R** must be sufficiently large to discourage excessive movement of the inputs but still be scaled relatively to the output weightings. Increasing **R**, which is analogous to reducing controller gains, is necessary in the face of plant-model mismatch and allows the offset-eliminating mechanism to converge to a steady state more swiftly. Improper selection of **R** relative to **Q** will result in model estimates 'chasing' after the measured outputs, while never truly converging. In initial experimentation to obtain tuning parameters that result in satisfactory MPC performance, the elements of **Q** were chosen such that the quadratic error term in the objective function for both CVs varied between zero and ten. In addition, **R** was initially chosen such that the MV penalties in the objective function were large enough to severely restrict movement and deter returning the CVs to set point. Subsequent simulations involved the simultaneous reduction of R_1 and R_2, whilst adjusting Q_1 and Q_2, to obtain swift but robust performance in both CVs and effective elimination of plant-model mismatch. The individual elements of **Q** can be further fine-tuned, based on the relative importance of keeping each CV close to its respective set point.

Through extensive simulation, tuning parameters for MPC design were found to give satisfactory performance, and are summarized in Table 5.4. The MPC with this configuration was tested using several scenarios as explored in Section 5.3.

Table 5.4: MPC tuning parameters.

Parameter	Value
Δt (seconds)	10
N	10
P	100
$\mathbf{Q}$	$\begin{bmatrix} 5 \times 10^{-4} & 0 \\ 0 & 10^3 \end{bmatrix}$
$\mathbf{R}$	$\begin{bmatrix} 4.125 & 0 \\ 0 & 0.326 \end{bmatrix}$
$\{ \mathbf{u_{min}}, \mathbf{u_{max}} \}$	$\left\{ \begin{bmatrix} 1 \\ 2 \end{bmatrix}, \begin{bmatrix} 30 \\ 5 \end{bmatrix} \right\}$
$Poles\left(\begin{bmatrix} T_{gas} & y_{CH_4} & \theta_1 & \theta_2 \end{bmatrix} \right)$	$10^{-5} \times \begin{bmatrix} 4.80 & 0.07 & 4.81 & 0.09 \end{bmatrix}$
L_x	$\begin{bmatrix} 2.02 & -97.73 \\ -4.0 \times 10^{-4} & 1.20 \end{bmatrix}$
L_θ	$\begin{bmatrix} -3.02 & -498.71 \\ 0.11 & -30.38 \end{bmatrix}$
G_θ	$\begin{bmatrix} -0.207 & 3.404 \\ -0.001 & -0.021 \end{bmatrix}$

5.3   Results: Digital PI vs MPC

Case 0a: + 1 percentage point step in y_{CH_4} set point
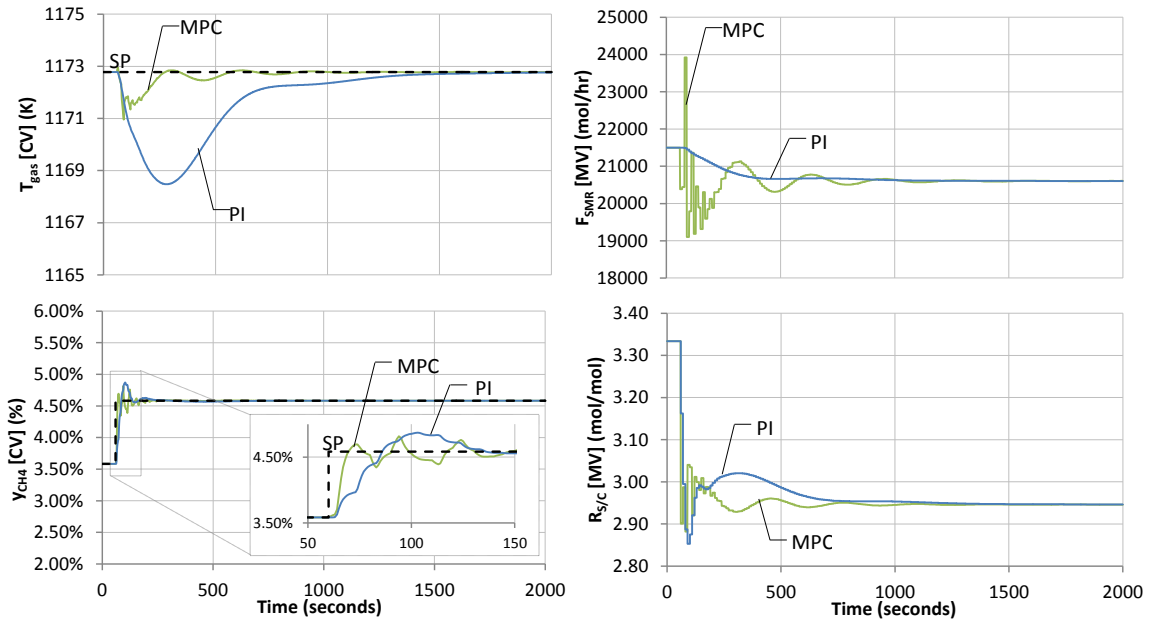
Figure 5.8: Comparison of PI and MPC (ten second sampling each) control for case 0a (+1 percentage point step in y_{CH_4} set point).

For a change in the y_{CH_4} set point, considerable performance improvement is seen with the MPC controller (Figure 5.8). Due to the MPC taking both outputs into consideration simultaneously, the flow rate F_{SMR} is aggressively moved at the time of set point change to reduce maximum deviation of T_{gas} from its set point. For y_{CH_4}, MPC drives the CV to set point faster than PI control; despite slight initial oscillation around the new set point, y_{CH_4} is effectively settled in approximately 100 seconds. When controlled by the MPC, T_{gas} returns to set point far more quickly than PI control. The aggressive movement of F_{SMR} can be reduced by relaxing the weight of the T_{gas} penalty term in the **Q** matrix, or by introducing "hard" Δu constraints within the MPC formulation.

Case 0b: -10 K step in T_{gas} set point

As with the previous case, the MPC controller takes swifter action than PI control overall due to not having to wait for error to appear between SP and CV. The performance increase is less substantial than in case 0a, with slight oscillations seen in the T_{gas} response. The F_{SMR} MV moves around significantly (see Figure 5.9), partly due to the speed of response being requested and θ chasing the plant-model mismatch. Overall MV movement of the MPC case can be reduced by increasing input penalty **R**, but will result in a more sluggish response in the T_{gas} output.
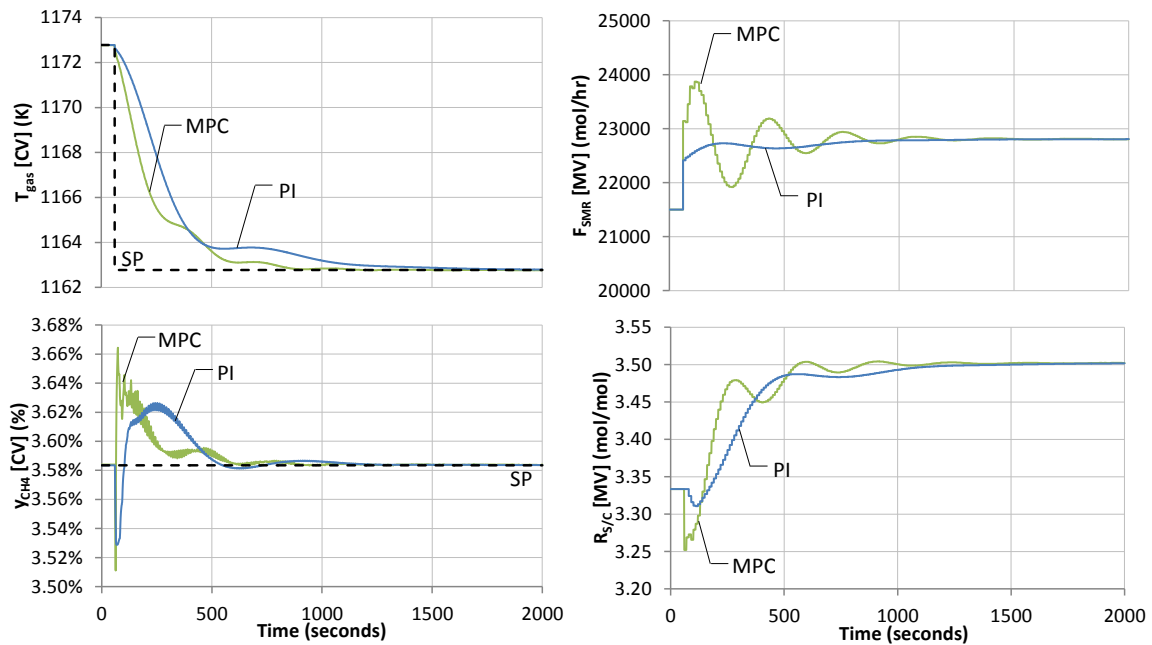
Figure 5.9: Comparison of PI and MPC (ten second sampling each) control for case 0b (- 10 K step in T_{gas} set point).

Case 1a: 50 K increase in gasifier exit temperature (T_S^{in})

For this disturbance (Figure 5.10), the MPC controller performs well with regards to both outputs. As expected, an increase in the gasifier exit temperature causes temperatures in the system to rise, requiring an increase in coolant (SMR) flow. Maximum deviation for T_{gas} using the MPC control is approximately +1.2 K, an 87% reduction from the maxi-

mum deviation observed using PI control. Similar reductions were seen with y_{CH_4} control. While the MPC control structure results in less movement in $R_{S/C}$ than PI, the flow rate F_{SMR} experiences increased movement, though not significantly so.
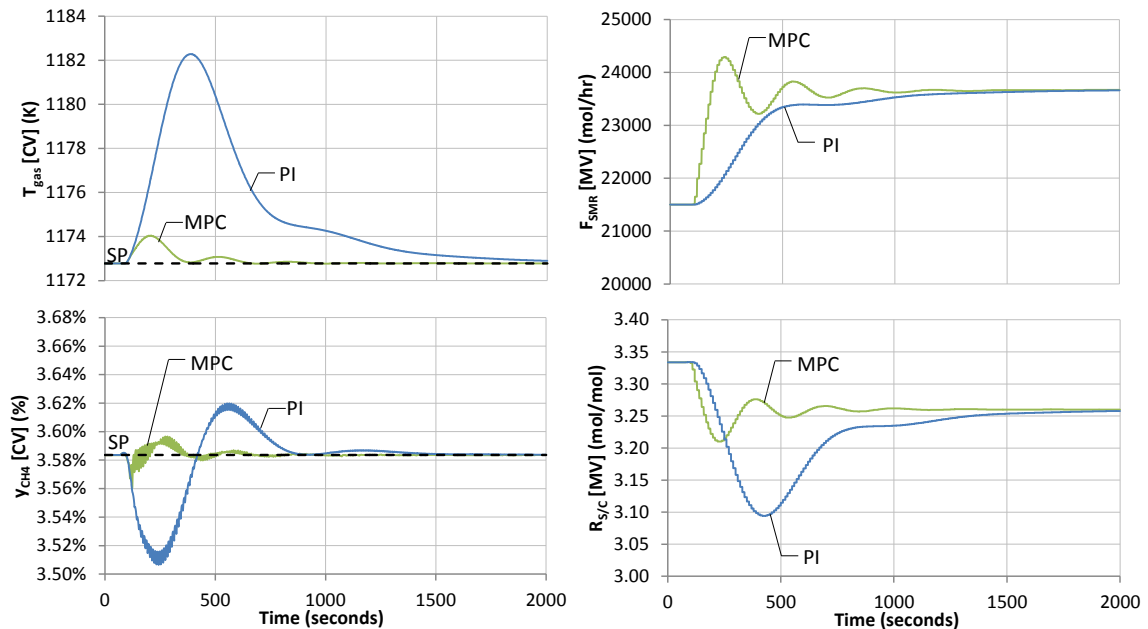
Figure 5.10: Comparison of PI and MPC (ten second sampling each) control for disturbance case 1a (50 K increase in gasifier exit temperature T_S^{in}).

Case 3b: 10% reduction in gasifier flow rate (M_S^{in})

For this disturbance in the gasifier syngas flow rate, both PI and MPC reduce the SMR flow rate due to the decreased gasifier load, but the MPC MV movement is significantly more oscillatory, especially in F_{SMR}. Maximum CV deviations from set point are drastically reduced from PI control, but experience oscillation that continue past the 2,000 second simulation window. If flow rate disturbances of this magnitude are to be expected, the MPC may need to be detuned (by increasing **R** or decreasing **Q**) to reduce these oscillations and produce a more desirable response.
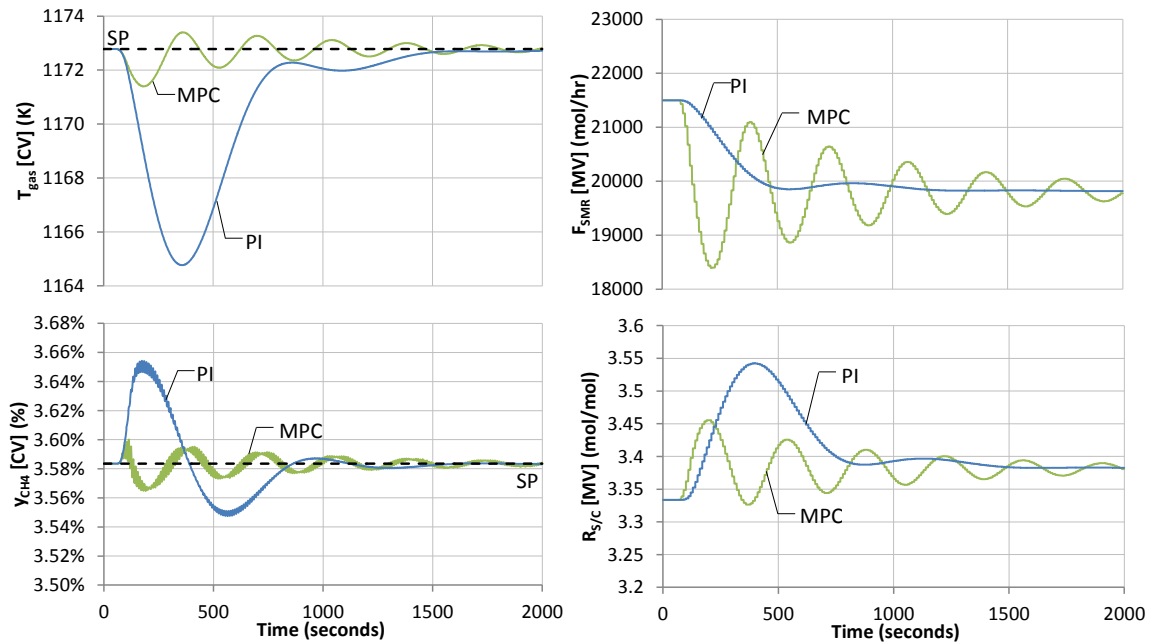
Figure 5.11: Comparison of PI and MPC (ten second sampling each) control for disturbance case 3b (10% reduction in gasifier flow rate M_S^{in}).

30 second MPC performance

Suppose that with the sensor and analyzer equipment installed in the plant, the fastest achievable sampling time of the measurements is thirty seconds. Figure 5.12 and Figure 5.13 illustrate that, when using thirty second MPC with the same tuning parameters as listed in Table 5.4, stable control performance is still achievable, even in instances where discrete PI control destabilized the system. In particular, by making a step change in the y_{CH_4} set point (Figure 5.12), there is still rapid approach of the y_{CH_4} CV to set point (case 0a). Recall that for this case (0a), the PI control strategy was completely unstable and therefore unable to achieve the requested set point change for this sample time. The penalty on T_{gas} can be reduced to obtain a less oscillatory but more sluggish return to set point. For thirty second sampled MPC, oscillations in the CVs and MVs are more pronounced for all cases relative to the ten second sampled MPC; this is expected, and detuning of the controller is required as a result.
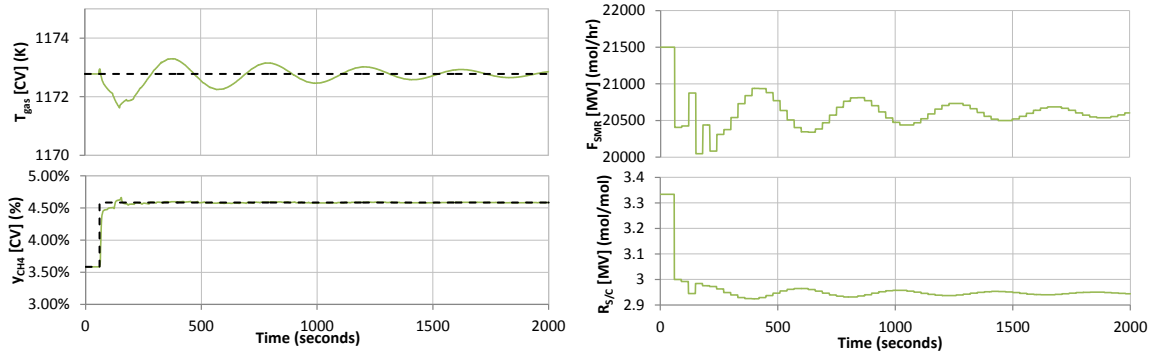
Figure 5.12: MPC (thirty second sampling) control for case 0a (+1 percentage point step in y_{CH_4} set point).
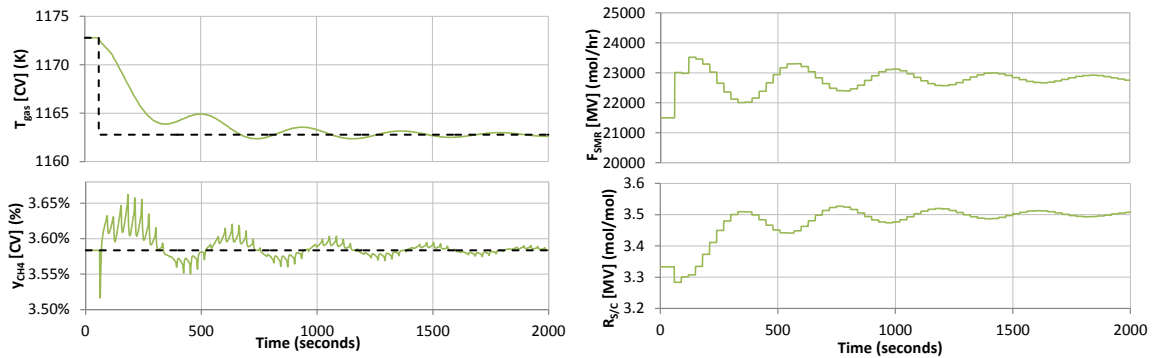
Figure 5.13: MPC (thirty second sampling) control for case 0b (-10 K step in T_{gas} set point).

5.4   Discussion/Broader Implications

The integral absolute error (IAE) metric was used to assess the relative performance of the investigated PI and MPC controllers (Table 5.5). PI control with a zero second sample time refers to continuous control. For all cases, the thirty second PI control provides the worst performance, especially for y_{CH_4} set point changes. Comparing ten second MPC to ten second PI, the average IAE for T_{gas} is reduced by 76%, while for y_{CH_4} the average IAE is reduced by 54%. Overall, ten second MPC outperforms continuous PI, with the exception of y_{CH_4} control in the set point change cases. When a sample time of thirty seconds is used, the MPC performance degrades for y_{CH_4} control, but is still within a stable and acceptable range and outperforms thirty second PI in all investigated cases.

Table 5.5: Comparison of IAE for various PI and MPC sample times.

	Δt (s)	T_{gas} IAE				y_{CH_4} IAE			
		Case 0a	Case 0b	Case 1a	Case 3b	Case 0a	Case 0b	Case 1a	Case 3b
PI	**0**	1.58	2.32	3.79	2.96	4.03	2.19	4.01	3.74
PI	**10**	1.62	2.34	3.90	3.05	6.41	3.76	6.82	6.64
MPC	**10**	0.19	1.47	0.22	0.48	4.18	2.84	0.65	2.19
PI	**30**	9.08	2.39	4.12	3.20	1407.86	20.47	38.02	20.88
MPC	**30**	0.39	1.86	1.15	2.65	6.28	5.40	5.56	12.10

The MPC control structure allows greater ease and flexibility in adjusting the control structure depending on the objectives. Depending on the end user, it may be desired to have less movement in the MVs while sacrificing set point tracking in the CVs. Through manipulation of the various MPC tuning parameters ($\mathbf{Q}, \mathbf{R}, \mathbf{L}, N, P$) the performance can be tweaked to satisfy user demands based on expected set point changes and plant disturbances. In addition, the MPC structure implemented in this work can be further improved upon by implementing disturbance models to greater counteract gasifier side upsets. However, this requires measurement of the disturbance states, which may not be possible. Additional objectives can also be implemented into the MPC design, perhaps to account for downstream syngas requirements. In particular, the set points of the MPC can be adjusted based on syngas quality requirements, while still providing adequate cooling duty to the coal-derived syngas.

Application of the device to a flexible polygeneration plant

In the context of a flexible polygeneration plant, it is desired to adjust NG-derived syngas production rates from the RSC/SMR device depending on the simultaneous demand for electricity and liquid fuels. For high liquid fuel demand, the NG-derived syngas throughput must be increased, to blend with and upgrade as much coal-derived syngas as possible, yielding syngas with a H_2/CO ratio of 2.0. Conversely, for low liquid fuel demand, the H_2 demand from NG-derived syngas is reduced as the H_2/CO ratio of syngas destined for electricity production can be less than 2.0. As such, to operate within this flexible polygeneration framework, the NG and steam flows to the SMR have to be dynamically ad-

justed to suit the desired syngas properties at any given time. However, adjustment of these flow rates must take into consideration cooling duty to the gasifier RSC, stability of the control system, and other safety considerations (such as tube wall and catalyst core temperatures). To demonstrate syngas production flexibility within the proposed RSC/SMR system, the T_{gas} set point was used as a handle to adjust the coolant (NG and steam) flow rates, while keeping y_{CH_4} (conversion) fixed.
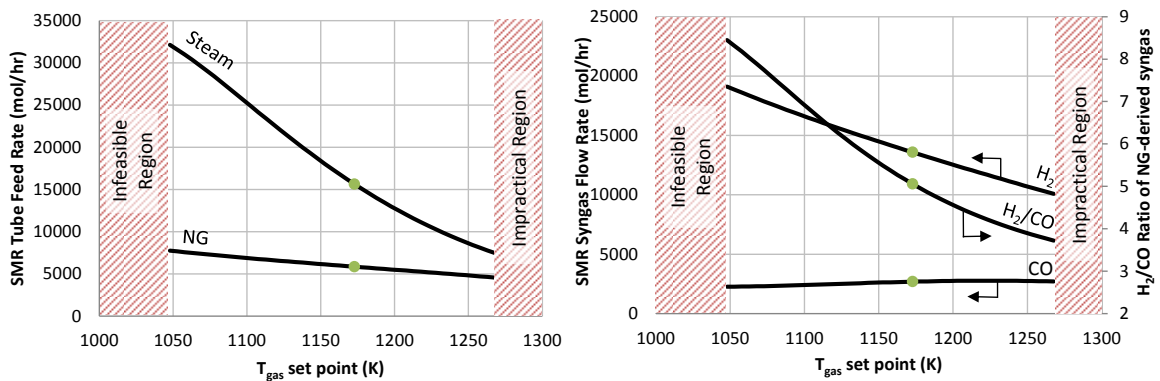
Figure 5.14: Steady state feed and product gas flow rates based on selected T$_{gas}$ set point. Green circle denotes nominal steady-state.

As seen in Figure 5.14, by increasing the T_{gas} set point, the cooling duty to the coal-derived syngas is reduced, resulting in elevated coal-derived syngas temperatures at the RSC exit. This is brought about by a reduction of the NG and steam flow rates to the SMR tubes, simultaneously reducing the production of H$_2$ and CO. The H$_2$/CO ratio also decreases in this regime, which is preferred when the requirement for upgrading the coal-syngas is reduced (minimum liquid fuel production). To maximize liquid fuel production, the T_{gas} set point can be decreased, which increases cooling duty to the coal-derived syn-gas. For a fixed CH$_4$ slip, with a reduction in T_{gas} set point the NG flow rate to the SMR tube increases, albeit at a slower rate than the increase in steam flow rate. As a result, the H$_2$/CO ratio increases at an accelerated pace at lower T_{gas} set points. The set point cannot be reduced below 1,047 K as operation of the device becomes infeasible due to excessive pressure drop across the tube (infeasible region in Figure 5.14). Increasing the T_{gas} set

point is also limited, as the controller becomes increasing oscillatory in the new operating region due to the reduced process gains. To explore operation beyond this upper T_{gas} region, the controller gains would need to be reduced; however the cooling-duty to the coal-derived syngas becomes inadequate at this point (impractical region in Figure 5.14).

Note that Figure 5.14 does not address dynamic operation of the RSC/SMR device, particularly the matter of transitioning from one steady-state operating point to another. Dynamic simulations were performed to test the ability of the device to transition from the nominal operating point (denoted by the green circle in Figure 5.14) to the hot or cold extremes of the T_{gas} set point change feasible region.
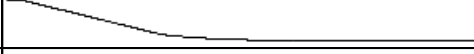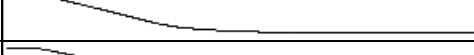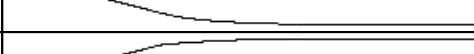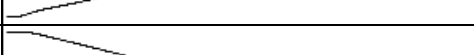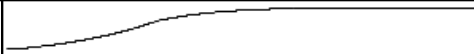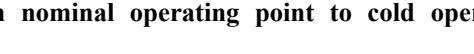
Set Point Change						
Variable	**Units**	**Initial**	**Trend (4800 second span)**	**Final**	**Min %**	**Max %**
T_{gas}	K	1172.78		1047.78	-10.7%	+0.0%
Controlled Variables						
Variable	**Units**	**Initial**	**Trend (4800 second span)**	**Final**	**Max Dev**	**IAE**
T_{gas}	K	1172.78		1047.82	+35.14	51.70
y_{CH4}	mol %	3.58		3.58	+0.04	15.48
Manipulated Variables						
Variable	**Units**	**Initial**	**Trend (4800 second span)**	**Final**	**Min %**	**Max %**
F_{SMR}	kmol/hr	21.50		39.90	+0.0%	+85.6%
$R_{S/C}$	mol/mol	3.33		5.17	-0.2%	+54.9%
Other State Variables						
Variable	**Units**	**Initial**	**Trend (4800 second span)**	**Final**	**Min %**	**Max %**
$T_{W|z=0}$	K	1214.28		1149.68	-5.3%	+0.0%
$T_{W|z=0.5L}$	K	1165.86		1066.18	-8.5%	+0.0%
$T_{W|z=L}$	K	1182.62		1067.42	-9.7%	+0.0%
$T_{cat|z=0}$	K	776.33		779.11	+0.0%	+0.4%
$T_{cat|z=0.5L}$	K	1113.59		1009.77	-9.3%	+0.0%
$T_{cat|z=L}$	K	1172.58		1047.23	-10.7%	+0.0%
T_S^{out}	K	1206.57		1127.20	-6.6%	+0.0%
ΔP_T	bar	3.99		16.07	+0.0%	+302.7%

Figure 5.15: Transition from nominal operating point to cold operating point (maximum NG throughput).
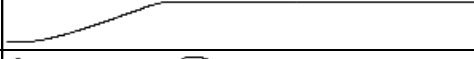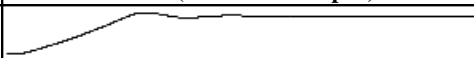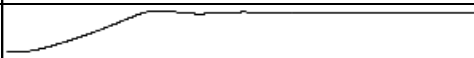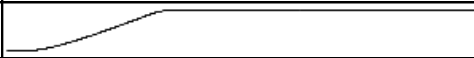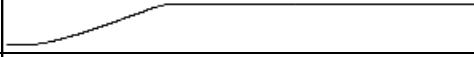
Set Point Change						
Variable	**Units**	**Initial**	**Trend (4800 second span)**	**Final**	**Min %**	**Max %**
T_{gas}	K	1172.78		1272.78	-0.0%	+8.7%
Controlled Variables						
Variable	**Units**	**Initial**	**Trend (4800 second span)**	**Final**	**Max Dev**	**IAE**
T_{gas}	K	1172.78		1272.80	-26.90	25.06
y_{CH4}	mol %	3.58		3.58	-0.03	12.35
Manipulated Variables						
Variable	**Units**	**Initial**	**Trend (4800 second span)**	**Final**	**Min %**	**Max %**
F_{SMR}	kmol/hr	21.50		11.66	-47.7%	+0.0%
$R_{S/C}$	mol/mol	3.33		1.99	-40.9%	+0.2%
Other State Variables						
Variable	**Units**	**Initial**	**Trend (4800 second span)**	**Final**	**Min %**	**Max %**
$T_{W|z=0}$	K	1214.28		1273.51	+0.0%	+5.4%
$T_{W|z=0.5L}$	K	1165.86		1261.20	+0.0%	+8.6%
$T_{W|z=L}$	K	1182.62		1277.14	+0.0%	+8.1%
$T_{cat|z=0}$	K	776.33		775.04	-0.3%	+0.0%
$T_{cat|z=0.5L}$	K	1113.59		1217.39	+0.0%	+10.0%
$T_{cat|z=L}$	K	1172.58		1272.70	-0.0%	+8.7%
T_S^{out}	K	1206.57		1284.42	+0.0%	+6.5%
ΔP_T	bar	3.99		1.22	-71.7%	+0.0%

Figure 5.16: Transition from nominal operating point to hot operating point (minimum NG throughput).

Figure 5.15 and Figure 5.16 illustrate the transitioning ability using continuous PI control. Figure 5.15 represents a transition from the nominal operating point (T_{gas} SP = 1,172 K) to the coldest feasible operating point in Figure 5.14 (T_{gas} SP = 1,047 K); this corresponds to maximum NG throughput. Likewise, Figure 5.16 shows the transition from the nominal operating point to the hottest feasible operating point in Figure 5.14 (T_{gas} SP = 1,272 K), corresponding to minimum NG throughput. In both cases, the T_{gas} set point was ramped at a rate of 5 K/min until the new desired set point was reached. The T_{gas} and

y_{CH_4} CVs were settled at their respective set points within the first hour after the ramp was initiated, with an underdamped response observed for T_{gas} with increasing set point (Figure 5.16). With regards to system dynamics, y_{CH_4} is only slightly affected and never deviates far from set point. As such, the risk of producing off-spec NG-derived syngas during these transitions is minimal.

To satisfy a large decrease in T_{gas} SP (Figure 5.15), the SMR tube throughput (F_{SMR}) was increased to 40 kmol/hr and the pressure drop was simultaneously increased to 16 bar, which is quite high and may cause unacceptably high re-compression costs downstream of the unit depending on the process in which it is used. Catalyst core and tube wall temperatures throughout the system trend in the same direction and manner as T_{gas} SP, with slightly reduced magnitude of deviation. For a 100 K increase in T_{gas} SP (Figure 5.16), the coolant flow rate F_{SMR} decreases by 48%, resulting in a 78 K increase in the coal-derived syngas temperature exiting the RSC. The maximum tube wall temperature increases to 1,277 K at the elevated T_{gas} SP, which is 50 K below the maximum tube wall temperatures seen in the counter-current base case nominal operation.

Note that the discussed scenarios explore possible transients with the proposed design, rather than optimal ones, in order to explore the operational flexibility of the system. The operating window in Figure 5.14 may be reduced further depending on several factors such as tube metallurgical considerations, catalyst core constraints, minimum required coal-derived syngas cooling duty, etc. These issues are material/vendor specific and are difficult to address at the present time, and should be investigated in future work.

Chapter 6

Conclusions and Recommendations

6.1 Conclusions

The major objective of this work was to investigate the operability and control of a hybrid gasifier/reformer device, and assess its suitability to the polygeneration plant concept.

A rigorous dynamic, two-dimensional heterogeneous model which was developed through first principles in prior work (Ghouse et al., 2014) was used to simulate the hybrid system. Several modifications were made to facilitate the implementation of a control structure on the system. A mass balance, momentum balance and water-gas shift reaction kinetics were appended to the shell gas (coal-derived syngas) model to enable the simulation of coal-derived syngas disturbances in the radiant syngas cooler. The tube and refractory wall models were upgraded from thin slab approximations to radial models, which facilitated a reduction of the previous errors in the energy balance. Discontinuities in the transfer of enthalpy due to gas diffusion previously modeled using `IF/ELSE` statements were removed by approximating the phenomena with a hyperbolic tangent function. This strategy, combined with the application of a custom numerical grid for the

catalyst to capture the sharp diffusion front at the particle surface, was shown to substantially reduce simulation time without a noticeable loss of numerical accuracy.

A base case design was developed for both co-current and counter-current configurations, which ensured tube wall and coal-derived syngas exit temperatures were sufficiently low, and adequate conversion of methane was achieved within the radiant tubes. The counter-current system was able to utilize coal-derived syngas heat more effectively than the co-current system, providing 33% greater cooling duty and 37% higher methane reformer throughput for the base case example. These advantages were severely hampered by the high maximum tube wall temperature (1,328 K) which, while lower than modern tube metallurgical limits, is well above temperatures observed in conventional SMRs and could result in comparatively shorter tube lives. The maximum tube temperatures for the co-current configuration, being 100 K lower, are more in line with typical SMR temperatures, but the coal-derived syngas enters the quench section at elevated temperatures in this case (though the quench pool is anticipated to handle this). Tube wall temperatures can be further lowered in both cases, but only at the expense of increased CH_4 slip in the SMR product gas, or increased steam feed flow rates (reducing process efficiency).

A multi-loop PI control structure was implemented for the gasifier/reformer device, whereby tube gas exit temperature (T_{gas}) was controlled by manipulating tube flow rate (F_{SMR}) and CH_4 slip (y_{CH_4}) was controlled by manipulating the steam-to-carbon ratio ($R_{S/C}$). This in itself constitutes a departure from conventional SMR control, where heat duty (via fuel gas flow) is a critical manipulated variable. For the gasifier/reformer system, heat duty, like all other coal-derived syngas variables, is a disturbance. A series of realistic set point change and disturbance scenarios were investigated, with internal model control (IMC) tuned control parameters used as an initial guess, followed by optimized tunings through minimization of integral absolute error (IAE). The control of the counter-current system was overall superior to co-current in terms of reducing integral average error and settling time, and was also able to reject a very severe disturbance in the amount of a 50% reduction in gasifier flow rate. Co-current control is inherently slower due to the

136

increased distance between the measurement location and the disturbance source; despite this, control performance after tuning was still found to be acceptable for moderate disturbance rejection and set point changes. However, in the case of severe gasifier upsets, feedback-only control is inadequate for the co-current system; feedforward control from coal-derived syngas flow to SMR flow must be implemented if such cases are to be expected. However, due to the nature of the system, such feedforward control is extremely difficult to implement.

Discrete feedback PI control performance depends on fast sample times, since the y_{CH_4} dynamic response to system perturbations is twenty times faster than the T_{gas} dynamic response. PI control performance was found to deteriorate substantially with sample times longer than ten seconds. An offset-free model predictive controller (MPC) was developed to address this issue, as well as to take process interactions into account. The linear control model was augmented with disturbance states, which were estimated using a Luenberger observer to effectively eliminate plant-model mismatch in the face of unknown disturbances. The MPC controller provided improved set point tracking and settling times versus PI control, especially in the temperature control (76% reduction in IAE relative to PI), which is important for preserving tube life-span. While the MPC easily rejected coal-derived syngas temperature fluctuations, variations in coal-syngas flow rate resulted in oscillatory response, necessitating MPC detuning. MPC control using a sampling time of ten seconds or less provides excellent control of the system; longer sample times (such as thirty seconds) result in drifting of the y_{CH_4} CV, but MPC in this case provides a stable response where PI destabilized the plant.

For the co-current system, the operation of the device within the flexible polygeneration context was demonstrated. Using the set point of T_{gas} as a handle, the operating envelope of the gasifier/reformer device was established. When greater emphasis is placed on electricity production (minimum liquid fuel production), the T_{gas} set point can be increased up to 100 K from the base case set point (1,172 K) in order to reduce SMR throughput and yield NG-derived syngas with an H_2/CO ratio of 3.7. Conversely, when maximum

liquid fuel production is required, the T_{gas} set point can be reduced by up to 125 K from the base case set point, maximizing SMR throughput and yielding NG-derived syngas with an H_2/CO ratio of 8.4. The expanse of this operating envelope may be constricted by practical considerations such as maximum allowable pressure drop, coal-derived syngas exit temperature and variations in the tube and catalyst temperatures, all of which depend on the chosen materials of construction.

6.2   Recommendations for Further Work

Improved MPC design:

The results of this work have demonstrated the benefits of implementing model-based control as opposed to multi-loop PI control for the proposed device. The MPC implementation can be improved upon in several areas. To address the severe non-linearity of the process caused by the strongly endothermic diffusion-limited reactions in the SMR catalyst, a series of locally linear models can be identified from multiple steady-state operating points for use in the MPC controller. The control model will transition from one linear model to the other based on current operating conditions, providing improved response in cases where the system is driven relatively far away from the model that has been linearized at the nominal steady-state.

Disturbance models may be identified from coal-side disturbances and incorporated into the MPC for improved disturbance rejection. This should be treated with caution, as one cannot realistically measure the coal-derived syngas conditions entering the RSC directly. To implement this in a realistic manner, a reduced gasifier model can be developed (similar to (Monaghan and Ghoniem, 2012b)) which uses measureable information such as coal slurry and oxygen flow rates, to predict gasifier exit conditions.

Within the MPC framework, the objective function can be reformulated to place less emphasis on maintaining an exact temperature and conversion set point. Additional objectives can be introduced, such as meeting the H_2 requirements of downstream processes,

while ensuring that the coal-derived syngas temperature at the RSC exit is below a minimum requirement. Market pricing for electricity and liquid fuels can also be incorporated into the MPC objective function to optimize the operation of the gasifier/reformer device and maximize profit.

Optimal Base Case Design:

This work demonstrated co-current and counter-current configurations that can operate safely in the gasifier and reject plausible disturbances. However, the base case designs, since they were determined though manually testing multiple plausible designs, are generally suboptimal; while the chosen designs satisfy safety and operability constraints, they do not consider the satisfaction of economic objectives. Optimization can be employed to determine an improved base case design that fits within the flexible polygeneration context, but may require model-order reduction techniques to be employed for the full non-linear model at the expense of some loss of accuracy. The throughput must be high enough to effectively blend with the coal-derived syngas, while the tube bundle must be able to fit within the RSC geometry without impeding the flow of slag. Tube wall temperatures must also be sufficiently low to prevent overheating and shortening of tube life span.

Start-up and Shut-down Scenarios:

Within this work, it was assumed that the gasifier/reformer device was able to achieve the desired steady-state safely and effectively. The nature of the start-up and shut-down scenario has not been explored but is critical to the commercial success of the design. While gasifiers and SMRs as individual units have their own scenarios in practice, the integration of the technologies requires careful synchronization of these operating procedures, in a manner that will not jeopardize the integrity of either system. The importance of a proper shut-down scenario is highlighted by the relatively short gasifier uptimes observed in industrial practice. The non-linear `gPROMS` model can be used to develop these scenarios.

LIST OF REFERENCES

AASBERG-PETERSEN, K., BAK HANSEN, J.-H., CHRISTENSEN, T. ., DYBKJAER, I., CHRISTENSEN, P. S., STUB NIELSEN, C., … ROSTRUP-NIELSEN, J. . (2001). Technologies for large-scale gas conversion. *Applied Catalysis A: General*, *221*(1), 379–387.

ADAMS, T. A., AND BARTON, P. I. (2009). A dynamic two-dimensional heterogeneous model for water gas shift reactors. *International Journal of Hydrogen Energy*, *34*(21), 8877–8891.

ADAMS, T. A., AND BARTON, P. I. (2011). Combining coal gasification and natural gas reforming for efficient polygeneration. *Fuel Processing Technology*, *92*(3), 639–655.

ALATIQI, I. (1990). Online quality control methods for steam-gas reformers. *International Journal of Hydrogen Energy*, *15*(3), 179–185.

ALATIQI, I., AND MEZIOU, A. (1991). Dynamic simulation and adaptive control of an industrial steam gas reformer. *Computers & Chemical Engineering*, *15*(3), 147–155.

ALATIQI, I., MEZIOU, A., AND GASMELSEED, G. (1989). Modelling, simulation and sensitivity analysis of steam-methane reformers. *International Journal of Hydrogen Energy*, *14*(4), 241–256.

BOCKELIE, M. J., DENISON, M. K., CHEN, Z., SENIOR, C. L., AND SAROFIM, A. F. (2003). Using Models To Select Operating Conditions for Gasifiers. In *Twentieth Annual Pittsburgh Coal Conference, Pittsburgh, PA (USA)*.

BOCKELIE, M. J., SWENSEN, D. A., DENISON, M. K., AND SAROFIM, A. F. (2004). A computational workbench environment for virtual power plant simulation. *Contract DE-FC26-00NT41047, Final Report*.

BOTERO, C., FIELD, R. P., BRASINGTON, R. D., HERZOG, H. J., AND GHONIEM, A. F. (2012). Performance of an IGCC plant with carbon capture and coal-CO2-slurry feed: Impact of coal rank, slurry loading, and syngas cooling technology. *Industrial & Engineering Chemistry Research*, *51*(36), 11778–11790.

BP P.L.C. (2013). *BP Statistical Review of World Energy 2013*. United Kingdom.

BP P.L.C. (2014). *BP Energy Outlook 2035*. United Kingdom.

BUSTAMANTE, F., ENICK, R. M., CUGINI, A. V., KILLMEYER, R. P., HOWARD, B. H., ROTHENBERGER, K. S., … SHI, S. (2004). High-temperature kinetics of the homogeneous reverse water-gas shift reaction. *AIChE Journal*, *50*(5), 1028–1041.

BUSTAMANTE, F., ENICK, R. M., KILLMEYER, R. P., HOWARD, B. H., ROTHENBERGER, K. S., CUGINI, A. V., … CIOCCO, M. V. (2005). Uncatalyzed and wall-catalyzed forward water-gas shift reaction kinetics. *AIChE Journal*, *51*(5), 1440–1454.

CHAU, P. C. (2002). *Process control: a first course with MATLAB*. Cambridge University Press.

CHOI, Y., AND STENGER, H. G. (2003). Water gas shift reaction kinetics and reactor modeling for fuel cell grade hydrogen. *Journal of Power Sources*, *124*(2), 432–439.

COLETTI, F., AND MACCHIETTO, S. (2011). A dynamic, distributed model of shell-and-tube heat exchangers undergoing crude oil fouling. *Industrial & Engineering Chemistry Research*, *50*(8), 4515–4533.

DE DEKEN J, C., DEVOS E, F., AND FROMENT G, F. (1982). Steam Reforming of Natural Gas: Intrinsic Kinetics, Diffusional Influences, and Reactor Design. *Chemical Reaction Engineering*, *196*, 181–197.

DE WILDE, J., AND FROMENT, G. F. (2013). Modeling of dual-zone structured reactors for natural gas steam reforming. *Industrial & Engineering Chemistry Research*, *52*(39), 14055–14065.

DRY, M. E. (2002). The Fischer–Tropsch process: 1950–2000. *Catalysis Today*, *71*(3), 227–241.

DYBKJÆR, I. (1995). Tubular reforming and autothermal reforming of natural gas—an overview of available processes. *Fuel Processing Technology*, *42*(2), 85–107.

ELNASHAIE, S. S. (1994). *Modelling, simulation and optimization of industrial fixed bed catalytic reactors.* (Vol 7.). CRC Press.

EPRI. (1990). Cool Water Coal Gasification Program: Final Report. *Report No. GS-6806*.

GHOUSE, J. H., AND ADAMS II, T. A. (2013). A multi-scale dynamic two-dimensional heterogeneous model for catalytic steam methane reforming reactors. *International Journal of Hydrogen Energy*, *38*(24), 9984–9999.

GHOUSE, J. H., SEEPERSAD, D., AND ADAMS II, T. A. (2014). Integration of steam methane reformer within the GE-Texaco radiant syngas cooler. *Unpublished Manuscript*.

GOVIND, R., AND SHAH, J. (1984). Modeling and simulation of an entrained flow coal gasifier. *AIChE Journal*, *30*(1), 79–92.

HAWKINS, G. (2013). *Steam Reforming Practical Operation*. GBH Enterprises Ltd.

JONES, W., AND LINDSTEDT, R. (1988). Global reaction schemes for hydrocarbon combustion. *Combustion and Flame*, *73*(3), 233–249.

KASULE, J. S., TURTON, R., BHATTACHARYYA, D., AND ZITNEY, S. E. (2012). Mathematical Modeling of a Single-Stage, Downward-Firing, Entrained-Flow Gasifier. *Industrial & Engineering Chemistry Research*, *51*(18), 6429–6440.

MARLIN, T. E. (2000). *Process control: designing processes and control systems for dynamic performance* (Vol. 2.). New York: McGraw-Hill.

MCDANIEL, J., AND HORNICK, M. (2002). Tampa Electric Polk Power Station Integrated Gasification Combined Cycle Project: Final Technical Report. *Prepared by Tampa Electric Company for The US Department of Energy*.

MEZIOU, A., AND ALATIQI, I. (1994). Identification and control of an industrial steam-reforming plant. *The Canadian Journal of Chemical Engineering*, *72*(2), 321–329.

MEZIOU, A., DESHPANDE, P., AND ALATIQI, I. (1995). Dynamic matrix control of an industrial steam gas reformer. *International Journal of Hydrogen Energy*, *20*(3), 187–192.

MONAGHAN, R., AND GHONIEM, A. (2012a). A dynamic reduced order model for simulating entrained flow gasifiers. Part II: Model validation and sensitivity analysis. *Fuel*, *94*, 280–297.

MONAGHAN, R., AND GHONIEM, A. (2012b). A dynamic reduced order model for simulating entrained flow gasifiers: Part I: Model development and description. *Fuel*, *91*(1), 61–80.

MONAGHAN, R., AND GHONIEM, A. (2012c). Simulation of a commercial-scale entrained flow gasifier using a dynamic reduced order model. *Energy & Fuels*, *26*(2), 1089–1106.

PANTOLEONTOS, G., KIKKINIDES, E. S., AND GEORGIADIS, M. C. (2012). A heterogeneous dynamic model for the simulation and optimisation of the steam methane reforming reactor. *International Journal of Hydrogen Energy*, *37*(21), 16346–16358.

PEDERNERA, M. N., PIÑA, J., BORIO, D. O., AND BUCALÁ, V. (2003). Use of a heterogeneous two-dimensional model to improve the primary steam reformer performance. *Chemical Engineering Journal*, *94*(1), 29–40.

PRECISIVE LLC. (2013). *Precisive 5 Hydrocarbon Composition Analyzer*. Woburn, MA: Precisive LLC.

PROCESS SYSTEMS ENTERPRISE. (2011). *gPROMS Model Developer Guide*. Process Systems Enterprise.

QIAN, F., KONG, X., CHENG, H., DU, W., AND ZHONG, W. (2013). Development of a Kinetic Model for Industrial Entrained Flow Coal Gasifiers. *Industrial & Engineering Chemistry Research*, *52*(5), 1819–1828.

QIN, S. J., AND BADGWELL, T. A. (2003). A survey of industrial model predictive control technology. *Control Engineering Practice*, *11*(7), 733–764.

RAJESH, J. K., GUPTA, S. K., RANGAIAH, G. P., AND RAY, A. K. (2000). Multiobjective optimization of steam reformer performance using genetic algorithm. *Industrial & Engineering Chemistry Research*, *39*(3), 706–717.

ROBINSON, P. J., AND LUYBEN, W. L. (2008). Simple dynamic gasifier model that runs in Aspen Dynamics. *Industrial & Engineering Chemistry Research*, *47*(20), 7784–7792.

ROFFEL, B., AND BETLEM, B. H. (2004). *Advanced Practical Process Control*. New York: Springer.

SANANDAJI, B. M., VINCENT, T. L., COLCLASURE, A. M., AND KEE, R. J. (2011). Modeling and control of tubular solid-oxide fuel cell systems: II. Nonlinear model reduction and model predictive control. *Journal of Power Sources*, *196*(1), 208–217.

SCHMIDT & CLEMENS INC. (2010). *High Alloys for the Petrochemical Industries*. Lindlar, Germany: Schmidt + Clemens GmbH.

SEBORG, D. E., MELLICHAMP, D. A., EDGAR, T. F., AND DOYLE, F. J. (2010). *Process Dynamics and Control*. John Wiley and Sons.

SINGH, C. P. P., AND SARAF, D. N. (1979). Simulation of Side Fired Steam-Hydrocarbon Reformers. *Industrial & Engineering Chemistry Process Design and Development*, *18*(1), 1–7.

STEYNBERG, A., AND DRY, M. (EDS.). (2004). *Fischer-Tropsch Technology*. Elsevier.

WALLACE, M., DAS, B., MHASKAR, P., HOUSE, J., AND SALSBURY, T. (2012). Offset-free model predictive control of a vapor compression cycle. *Journal of Process Control*, *22*(7), 1374–1386.

WATANABE, H., AND OTAKA, M. (2006). Numerical simulation of coal gasification in entrained flow coal gasifier. *Fuel*, *85*(12), 1935–1943.

WESENBERG, M., AND SVENDSEN, H. (2007). Mass and heat transfer limitations in a heterogeneous model of a gas-heated steam reformer. *Industrial & Engineering Chemistry Research*, *46*(3), 667–676.

WOODS, M. C., CAPICOTTO, P. J., HASLBECK, J. L., KUEHN, N. J., MATUSZEWSKI, M., PINKERTON, L. L., … VAYSMAN, V. (2007). Cost and performance baseline for fossil energy plants. *National Energy Technology Laboratory*.

XU, J., AND FROMENT, G. (1989). Methane steam reforming: II. Diffusional limitations and reactor simulation. *AIChE Journal*, *35*(1), 97–103.